



저작자표시-비영리-변경금지 2.0 대한민국

이용자는 아래의 조건을 따르는 경우에 한하여 자유롭게

- 이 저작물을 복제, 배포, 전송, 전시, 공연 및 방송할 수 있습니다.

다음과 같은 조건을 따라야 합니다:



저작자표시. 귀하는 원저작자를 표시하여야 합니다.



비영리. 귀하는 이 저작물을 영리 목적으로 이용할 수 없습니다.



변경금지. 귀하는 이 저작물을 개작, 변형 또는 가공할 수 없습니다.

- 귀하는, 이 저작물의 재이용이나 배포의 경우, 이 저작물에 적용된 이용허락조건을 명확하게 나타내어야 합니다.
- 저작권자로부터 별도의 허가를 받으면 이러한 조건들은 적용되지 않습니다.

저작권법에 따른 이용자의 권리는 위의 내용에 의하여 영향을 받지 않습니다.

이것은 [이용허락규약\(Legal Code\)](#)을 이해하기 쉽게 요약한 것입니다.

[Disclaimer](#)

이학박사 학위논문

**Surface Modified
Inorganic Materials for
Nano Forensic Applications**

나노 법과학적 응용을 위한
표면 개질된 무기물질에 대한 연구

2015 년 8 월

서울대학교 대학원

화학부 무기화학전공

유 승 진

Ph. D. Dissertation

**Surface Modified
Inorganic Materials for
Nano Forensic Applications**

Supervisor : Professor Dongwhan Lee

Co-Supervisor : Jin-Kyu Lee

Major : Inorganic Chemistry

June 2015

By Seung-Jin Ryu

Department of Chemistry

The Graduate School

Seoul National University

Surface Modified Inorganic Materials for Nano Forensic Applications

지도교수 이 동 환
공동지도교수 이 진 규

이 논문을 이학박사 학위논문으로 제출함
2015 년 6 월

서울대학교 대학원
화학부 무기화학전공
유 승 진

유승진의 박사 학위논문을 인준함
2015 년 6 월

위원장	손 병 혁	(인)
부위원장	이 동 환	(인)
위원	이 진 규	(인)
위원	정 택 동	(인)
위원	윤 태 중	(인)

Abstract

Surface Modified Inorganic Materials for Nano Forensic Applications

Seung-Jin Ryu

Department of Chemistry

Graduate School

Seoul National University

Surface modified Inorganic Materials have attracted considerable research interest due to their advantages of bi or multi-functionality and various applications. In this thesis, I demonstrate Metal-ion-modified silica powder for colorimetric forensic sensor, Photoluminescent europium(III) complex intercalated in natural and synthetic clay minerals for enhanced latent fingerprint detection and Semiconductor Quantum Dots as a Fluorescent Inorganic Nanomaterial for Forensic Application.

In Chapter 1, we briefly explain evidence in forensic science and summarized *On-site* Colorimetric Sensor using Metal-ion-modified silica powder, latent fingerprint detection using Nanocomposite materials and fingerprint development using Fluorescent Inorganic Nanomaterials for Forensic Application.

In Chapter 2, we demonstrated Quantitative Detection of Toxic H₂S and NH₃ Gases using Metal-Ion-Modified Silica Powders. A highly sensitive *on-site* colorimetric forensic sensor has been developed for the quantitative detection of hydrogen sulfide and ammonia gases. The sensor consists of metal-ion-modified silica-gel powders placed in a glass tube. The powder

color changes upon reaction with toxic hydrogen sulfide and ammonia gases. It is capable of easily detecting toxic gases in the concentration range between 100 ppm, which is considered as immediately dangerous to life and health, and 3000 ppm, which may cause death, by using a glass tube with an inner diameter of 3 mm. Since the sensor reported here is insensitive to environmental conditions such as temperature or humidity, and is featured by simplicity, fast response, high sensitivity, and easily understandable results based on absolute affirmative/negative response, it is expected to be effectively used for *on-site* applications such as testing the existence of toxic gases in confined working and industrial spaces.

In Chapter 3, we examined Quantitative Detection of Toxic S^{2-} Ion in Blood Plasma using Metal-Ion-Modified Silica Powders. Immensely sensitive, accurate and simple *on-site* colorimetric sensor has been developed for the quantitative detection of the sulfide ion in human blood plasma. The colorimetric sensor consists of lead-ion-modified silica-gel powders placed in a glass tube. The powder color changes upon reaction with sulfide ions in blood plasma. It is capable of easily detecting toxic sulfide ion by using a glass tube with an inner diameter of 3 mm. By employing the type of colorimetric sensor to a blood sample, it is possible to detect the sulfide ion with a concentration limit of 0.1 ppm and excellent reproducibility, thus making it superior to conventional analysis methods that need multiple preparation processes and various sophisticated instruments. Since the sensor reported here is insensitive to environmental conditions such as temperature or humidity, and is featured by simplicity, fast response, high sensitivity, and easily understandable results based on absolute affirmative/negative response, it is expected to be effectively used for *on-site* applications such as detecting poisonous ions in blood samples.

In Chapter 4, we demonstrated Photoluminescent europium(III) complex intercalated in natural and synthetic clay minerals for enhanced latent fingerprint detection. Fluorescent nanohybrid materials, europium(III) complex intercalated Na^+ -smectite clay minerals (synthetic hectorite and natural montmorillonite), have been developed to visualize latent fingerprints. The guest europium(III) complex $([\text{EuCl}_2(\text{Phen})_2(\text{H}_2\text{O})_2]\text{Cl}\cdot\text{H}_2\text{O})$ was obtained by simple complex reaction between europium chloride hexahydrate $(\text{EuCl}_3\cdot 6\text{H}_2\text{O})$ and 1,10-phenanthroline (Phen) as a 1:2 molar ratio of Eu^{3+} ion to ligand molecules. The intercalated nanohybrids $([\text{Eu}(\text{Phen})_2]^{3+}\text{-clay minerals})$ were obtained through ion exchange reaction of interlayer sodium cation with europium complex ion. Guest europium(III) complex and $([\text{Eu}(\text{Phen})_2]^{3+}\text{-clay mineral hybrids})$ were characterized by powder X-ray diffraction, Fourier transform infrared, thermal analysis (TG-DTA), elemental analysis, UV-visible and fluorescence spectroscopy. The intercalated complex maintains a characteristic red $^5\text{D}_0\text{-}^7\text{F}_2$ emission at wavelength 617 nm, which is comparable to the free complex. The $^5\text{D}_0\text{-}^7\text{F}_2$ emission intensity of $([\text{Eu}(\text{Phen})_2]^{3+}\text{-hectorite})$ was *ca.* 3.5 times higher than that of $([\text{Eu}(\text{Phen})_2]^{3+}\text{-montmorillonite})$, due to the presence of quenching impurities in natural montmorillonite itself. Fingerprint residues on glass slides were harvested by using $([\text{Eu}(\text{Phen})_2]^{3+}\text{-clay mineral powders})$, resulting in good definition for enhanced latent fingerprint detection. Particularly, $([\text{Eu}(\text{Phen})_2]^{3+}\text{-hectorite hybrid powder})$ was more clearly separated from the background compared to the montmorillonite hybrid powder.

In Chapter 5, we described Nano Forensic Application: Latent Fingerprint Detection on Diverse Surfaces by means of the Multifunctional Properties of Nanocomposite powder. We used photoluminescent $([\text{Eu}(\text{Phen})_2]^{3+}\text{-clay nanocomposite powder})$ to enhance the visualization of latent fingerprints on

diverse porous and non-porous surfaces. We obtained nanocomposites powder through the ion exchange reaction of interlayer sodium cation in two different types of clay (synthetic hectorite type and natural montmorillonite-type) with europium (III) complex ion. Moreover, in order to improve interaction between latent fingerprint residue and nanocomposites powder, we successfully modified the surface property of $[\text{Eu}(\text{Phen})_2]^{3+}$ -hectorite nanocomposite to be more hydrophobic by means of simple silylation reaction with hydroxyl group at the edge of clay and hexadecyltrimethoxysilane molecules. The nanocomposites powder showed a characteristic red emission at wavelength 617 nm. We detected and visualized latent fingerprints on the non-porous surfaces of glass, polymer film, plastic, metal, and adhesive tape. Also, we detected latent fingerprints on the porous surfaces of adhesive tape made of paper, credit card receipts, and paper money.

In Chapter 6, we explored Latent Fingerprint Detection using Semiconductor Quantum Dots as a Fluorescent Inorganic Nanomaterial for Forensic Application. We synthesized QD@SiO_2 by a modified Stober method to enhance the visualization of latent fingerprints on diverse surfaces with maintaining PL efficiency. In order to synthesize green-emitting QD (GQD) gradient alloy QDs ($\lambda_{\text{em}} = 530 \text{ nm}$) emitting green light, CdO and $\text{Zn}(\text{OAc})_2$ were put into a 100-mL two-neck-RBF, and a condenser and a thermocouple were connected to the RBF. Then OA and ODE were put into the RBF, which was heated at $180 \text{ }^\circ\text{C}$ until the color of the solution went transparent. Amphiphilic polymers such as polyvinylpyrrolidone (PVP) were directly adsorbed onto the surface of semiconductor QDs. Also, silica shells were introduced to the QDs to synthesize QD@SiO_2 which maintains PL efficiency. QD@SiO_2 synthesized by a modified Stober method was appropriate for the detection and visualization of latent fingerprint as it

maintained very strong emission efficiency as well as biocompatibility due to the silica shells on the surface. The strong fluorescence of QD could effectively visualize latent fingerprint deposited on various substrates found at the crime scenes such as aluminum foil, paper money, transparent polymer film and glass using Olympus camera. Most of the obtained fluorescent GQD@SiO₂ nano-powders based latent fingerprint developers proved successful in developing latent fingerprints on porous and nonporous substrates. Moreover, Photographs of latent fingerprints developed with GQD@SiO₂ nano-powders on porous surfaces of paper money and on non-porous surfaces of plastic materials using Video spectral comparator 6000. The results show superior fingerprint ridge images with photoluminescent property for the latent fingerprint detection in forensic application.

Keywords: Colorimetric detection, On-site forensic sensor, Toxic gas, Metal ion-modified silica, hydrogen sulfide, sulfide ion, Aluminosilicates, Intercalations, Europium, Luminescence, Organic-inorganic hybrid composites, Nanocomposites, Porous and non-porous surfaces, Luminescence, Europium complex, Fluorescent inorganic nanomaterial, Latent fingerprint detection; Forensic application

Student Number: 2008-30096

Contents

Abstract	i
Contents	vi
List of Figures	ix
List of Tables	xvii

Chapter 1. Research Background.....1

1.1 Evidence in Forensic Science	2
1.2 On-site Colorimetric Sensor for Forensic Application.....	4
1.3 Nanocomposite Materials for Forensic Application	10
1.4 Fluorescent Inorganic Nanomaterials for Forensic Application.....	16
1.5 References	20

Chapter 2. *On-site* Colorimetric Forensic Sensor (I): Quantitative Detection of Toxic H₂S and NH₃ Gases using Metal-Ion-Modified Silica Powders.....24

2.1 Abstract	25
2.2 Introduction	26
2.3 Experimental Section	28
2.4 Results and Discussion	32
2.5 Conclusions	39
2.6 References	40

Chapter 3. *On-site* Colorimetric Forensic Sensor (II):

**Quantitative Detection of Toxic S²⁻ Ion in Blood Plasma
using Metal-Ion-modified Silica Powders42**

3.1 Abstract43
3.2 Introduction44
3.3 Experimental Section46
3.4 Results and Discussion49
3.5 Conclusions57
3.6 References58

**Chapter 4. Photoluminescent europium(III) complex
intercalated in natural and synthetic clay minerals for
enhanced latent fingerprint detection60**

4.1 Abstract61
4.2 Introduction62
4.3 Experimental Section65
4.4 Results and Discussion68
4.5 Conclusions87
4.6 References88

**Chapter 5. Nano Forensic Application: Latent
Fingerprint Detection on Diverse Surfaces by means of
the Multifunctional Properties of Nanocomposite Powder
.....93**

5.1 Abstract94
5.2 Introduction95
5.3 Experimental Section98

5.4	Results and Discussion	101
5.5	Conclusions.....	114
5.6	References.....	115

Chapter 6. Latent Fingerprint Detection using Semiconductor Quantum Dots as a Fluorescent Inorganic Nanomaterial for Forensic Application 118

6.1	Abstract	119
6.2	Introduction.....	120
6.3	Experimental Section.....	123
6.4	Results and Discussion	125
6.5	Conclusions.....	131
6.6	References.....	132

APPENDIX/Chapter 1. Layered double hydroxides as novel antibacterial drug delivery system134

1.1	Abstract.....	135
1.2	Introduction.....	136
1.3	Experimental Section.....	139
1.4	Results and Discussion	142
1.5	Conclusions.....	147
1.6	References.....	148

Korean Abstract149

List of Figures

Chapter 1

Figure 1-1. Preparation of metal-cation-modified silica powders.....	6
Figure 1-2. Experimental settings for detecting (I) H ₂ S or NH ₃ gases, and (II) S ²⁻ ion by metal-cation-modified sulfonated silica powders.	6
Figure 1-3. Schematic representation of (a) molecular crystal structure of Eu(III) complex and (b) [Eu(Phen) ₂] ³⁺ -clay mineral hybrids.....	11
Figure 1-4. Schematic representation of (a) intercalation reaction for [Eu(Phen) ₂] ³⁺ -montmorillonite/hectorite nanocomposites and (b) silylation for [Eu(Phen) ₂] ³⁺ -hectorite-HDTMS nanocomposite.	12
Figure 1-5. Schematic representation of synthesized GQD@SiO ₂ nanoparticles and latent fingerprint detection.	17

Chapter 2

Scheme 2-1. Experimental settings of the colorimetric sensor for detecting H ₂ S or NH ₃ gases (I) and reaction mechanism of color change between toxic H ₂ S, NH ₃ gases and metal-cation-modified sulfonated silica powders (II) . . .	30
Scheme 2-2. Preparation of metal-cation-modified silica powders.	32
Figure 2-1. SEM images showing the morphology of original sulfonated	

silica powders (left), sulfonated silica powders modified with silver cation (middle), and sulfonated silica powders after formation of Ag₂S band (right) ...

..... 32

Figure 2-2. SEM images showing the morphology of original sulfonated silica powders (left), sulfonated silica powders modified with copper cation (middle), and sulfonated silica powders after formation of [Cu(NH₃)₄]²⁺ complex band (right)..... 33

Figure 2-3. EDX spectra showing the presence of silver (left) and copper (right) after surface modification of sulfonated silica powders with metal cations 33

Figure 2-4. Digital images of Ag₂S bands formed after exposing the tube sensors packed with silver-modified silica powder to 450 mL of the contaminated air with various amount of H₂S gas (top). Linear dependency of Ag₂S band width on the H₂S gas concentration (bottom) 35

Figure 2-5. Digital images of [Cu(NH₃)₄]²⁺ bands formed after exposing the tube sensors packed with copper-modified silica powder to 900 mL of NH₃ gas (top). Linear dependency of [Cu(NH₃)₄]²⁺ band width on the NH₃ gas concentration (bottom) 36

Chapter 3

Scheme 3-1. Experimental settings of the colorimetric sensor for detecting

H ₂ S or NH ₃ gases (I) and reaction mechanism of color change between toxic H ₂ S, NH ₃ gases and metal-cation-modified sulfonated silica powders (II)	48
Schem 3-2. Preparation of metal-cation-modified silica powders.....	49
Figure 3-1. SEM images showing the morphology of original sulfonated silica powders (left), sulfonated silica powders modified with lead cation (middle), and sulfonated silica powders after formation of PbS band (right).	49
Figure 3-2. EDX spectra showing the presence of lead after surface modification of sulfonated silica powders with metal cation.....	50
Figure 3-3. Sulfide ion determination in human blood sample by the Conway micro diffusion method and its corresponding correlation coefficient value.	52
Figure 3-4. Sulfide ion determination in human blood sample by dialysis membrane filter method and its corresponding correlation coefficient value .	53
Figure 3-5. Digital images of PbS bands formed after 5 mL of human blood plasma containing various concentration of S ²⁻ ion was passed through glass column packed with lead-modified silica powder (top). Linear dependency of PbS band width on the S ²⁻ ion concentration in human blood plasma (bottom) .	55

Chapter 4

Figure 4-1. X-ray diffraction patterns of (a) Eu(III) complex ([EuCl₂(Phen)₂(H₂O)₂]Cl·H₂O), (b) pristine Na⁺-hectorite, (c) [Eu(Phen)₂]³⁺-hectorite hybrid, (d) pristine Na⁺-montmorillonite and (e) [Eu(Phen)₂]³⁺-montmorillonite hybrid **69**

Figure 4-2. Schematic representation of (a) molecular crystal structure of Eu(III) complex and (b) [Eu(Phen)₂]³⁺-clay mineral hybrids. **73**

Figure 4-3. TG and DTA curves of (a) Eu(III) complex. **74**

Figure 4-3. TG and DTA curves of (b) [Eu(Phen)₂]³⁺-hectorite hybrid and (c) [Eu(Phen)₂]³⁺-montmorillonite hybrid **75**

Figure 4-4. Fourier transform infrared spectra of (a) Eu(III) complex, (b) pristine Na⁺-hectorite, (c) [Eu(Phen)₂]³⁺-hectorite hybrid (d) pristine Na⁺-montmorillonite and (e) [Eu(Phen)₂]³⁺-montmorillonite hybrid. **77**

Figure 4-5. Diffuse reflectance UV-vis spectra of solid (a) Eu(III) complex, (b) [Eu(Phen)₂]³⁺-hectorite hybrid and (c) [Eu(Phen)₂]³⁺-montmorillonite hybrid. The inset represents the intra-configurational 4*f*-4*f* transitions of Eu(III) complex. **79**

Figure 4-6. The room-temperature solid-state excitation and emission spectra of (a) Eu(III) complex, (b) [Eu(Phen)₂]³⁺-hectorite hybrid and (c) [Eu(Phen)₂]³⁺-montmorillonite hybrid. **83**

Figure 4-7. Photographs of latent fingerprints on glass slides developed with

[(a) and (c)] the $[\text{Eu}(\text{Phen})_2]^{3+}$ -hectorite hybrid and [(b) and (d)] $[\text{Eu}(\text{Phen})_2]^{3+}$ -montmorillonite hybrid powders before [(a) and (b)] and after [(c) and (d)] UV irradiation at 312 nm, respectively..... **86**

Chapter 5

Figure 5-1. Schematic representation of (a) intercalation reaction for $[\text{Eu}(\text{Phen})_2]^{3+}$ -montmorillonite/hectorite nanocomposites and (b) silylation for $[\text{Eu}(\text{Phen})_2]^{3+}$ -hectorite-HDTMS nanocomposite. **102**

Figure 5-2(a). X-ray diffraction patterns of (a) Eu(III) complex, (b) $[\text{Eu}(\text{Phen})_2]^{3+}$ -montmorillonite nanocomposite (*: quartz), (c) $[\text{Eu}(\text{Phen})_2]^{3+}$ -hectorite nanocomposite and (d) $[\text{Eu}(\text{Phen})_2]^{3+}$ -hectorite-HDTMS nanocomposite..... **103**

Figure 5-2(b). The solid-state emission spectra of $[\text{Eu}(\text{Phen})_2]^{3+}$ -montmorillonite nanocomposite (dotted line), $[\text{Eu}(\text{Phen})_2]^{3+}$ -hectorite nanocomposite (solid line) and $[\text{Eu}(\text{Phen})_2]^{3+}$ -hectorite-HDTMS nanocomposite (dashed line)..... **104**

Figure 5-3. Latent fingerprint images developed by $[\text{Eu}(\text{Phen})_2]^{3+}$ -montmorillonite nanocomposite deposited on different non-porous surfaces illuminated with 312 nm light. Fingerprints on (a) glass, (b) polymer film, (c) plastic, (d) metal and (e) adhesive tape are shown..... **106**

Figure 5-4. Latent fingerprint images developed by $[\text{Eu}(\text{Phen})_2]^{3+}$ -hectorite

nanocomposite deposited on different non-porous surfaces illuminated with 312 nm light. Fingerprints on (a) glass, (b) polymer film, (c) plastic, (d) metal and (e) adhesive tape are shown..... **107**

Figure 5-5. Latent fingerprint images developed by $[\text{Eu}(\text{Phen})_2]^{3+}$ -hectorite-HDTMS nanocomposite deposited on different non-porous surfaces illuminated with 312 nm light. Fingerprints on (a) Glass, (b) polymer film, (c) plastic, (d) metal and (e) adhesive tape are shown..... **108**

Figure 5-6. Photographs of latent fingerprints developed with $[\text{Eu}(\text{Phen})_2]^{3+}$ -montmorillonite nanocomposite on porous surfaces of (a) tape made of paper, (b) traditional credit card receipt and (c) credit card receipt made of electronic paper under UV illumination at 312 nm..... **110**

Figure 5-7. Photographs of latent fingerprints developed with $[\text{Eu}(\text{Phen})_2]^{3+}$ -hectorite nanocomposite on porous surfaces of (a) tape made of paper, (b) traditional credit card receipt and (c) credit card receipt made of electronic paper under UV illumination at 312 nm..... **111**

Figure 5-8. Photographs of latent fingerprints developed with $[\text{Eu}(\text{Phen})_2]^{3+}$ -hectorite-HDTMS nanocomposite on porous surfaces of (a) tape made of paper, (b) traditional credit card receipt and (c) credit card receipt made of electronic paper under UV illumination at 312 nm..... **111**

Figure 5-9. Comparison of the latent fingerprints developed using different nanocomposites on paper money surfaces. (a) $[\text{Eu}(\text{Phen})_2]^{3+}$ -montmorillonite, (b) $[\text{Eu}(\text{Phen})_2]^{3+}$ -hectorite and (c) $[\text{Eu}(\text{Phen})_2]^{3+}$ -hectorite-HDTMS. Upper

and lower column are shown under white illumination and UV illumination (312 nm), respectively..... **112**

Chapter 6

Figure 6-1. Schematic representation of synthesized GQD@SiO₂ nanoparticles..... **125**

Figure 6-2. TEM images of GQDs..... **126**

Figure 6-3. UV-visible absorbance and PL spectra **126**

Figure 6-4. PL spectra of GQD@SiO₂ depending on reaction time..... **127**

Figure 6-5. TEM images of GQD depending on reaction time; initial time (a), after 1 hour (b), 2 hours (c), 3 hours (d), 6 hours (e), 9 hours (f) 12 hours (g) and 24 hours (h). From the reaction, QD@SiO₂ of about 2.5 g could be acquired..... **128**

Figure 6-6. Detection of latent fingerprint using GQD@SiO₂ on aluminum foil (a), paper money (b), transparent polymer film (c) and glass (d)..... **129**

Figure 6-7. Detection of latent fingerprint on paper money as a porous surface using GQD@SiO₂ monitoring visible region (a, c) and 354-nm (b, d) **130**

Figure 6-8. Detection of latent fingerprint on plastic surface as a non-porous surface using GQD@SiO₂ monitoring visible region (a) and 354-nm (b). ... **130**

APPENDIX/Chapter 1

APPENDIX/Figure 1-1. Molecular structure of the cefazolin sodium salt	138
APPENDIX/Figure 1-2. Powder X-ray diffraction patterns of cefazolin-LDH (a), ZnAl-LDH (b) and cefazolin sodium (c)	142
APPENDIX/Figure 1-3. Schematic structure of cefazolin molecules in the LDH interlayer space	143
APPENDIX/Figure 1-4. Zones of bacterial inhibition of (a) LDH, (b) cefazolin sodium, and (c) cefazolin-LDH nanohybrid in (A) water and (B) a 0.8 % NaCl solution	146

List of Tables

Chapter 2

Table 2-1. Linear Response Range	38
Table 2-2. Detection Limits and Colorimetric Change.....	38

Chapter 3

Table 3-1. Linear Response Range	56
Table 3-2. Detection Limits and Colorimetric Change.....	56

Chapter 4

Table 4-1. XRD analysis results and chemical formulas for Eu(III) complex and $[\text{Eu}(\text{Phen})_2]^{3+}$ -clay mineral hybrids	73
Table 4-2. Photoluminescence data for Eu(III) complex and $[\text{Eu}(\text{Phen})_2]^{3+}$ -clay mineral hybrids.....	84

Chapter 5

Table 5-1. Comparison of definition for the latent fingerprint developed by nanocomposites. (* * *) represents clear fingerprint ridge, (* *) most of the fingerprint ridge and (*) faint fingerprint image, respectively.....	113
---	------------

APPENDIX/Chapter 1

APPENDIX/table 1-1. Chemical compositions of the pristine LDH and cefazolin-LDH hybrid by ICP and CHNS measurements.....	144
---	------------

Chapter 1

Research Background

1.1. Evidence in Forensic Science.

Forensic science is “a mixed science” (Oxford English Dictionary, 2005). The areas of forensic science consist of criminalistics, chemistry, physics, biology, engineering, anthropology, odontology, pathology and toxicology etc. The purpose of forensic science is the application of science to law. Forensic science applies the knowledge and technology of science to the definition and enforcement of such laws. These knowledge and technology could be useful for determining the evidential value of crime scene and related evidence.^{1,2}

Various forms of forensic evidences at the crime scenes have been reported including toxic chemicals, fibers, paints, ink, toner, metals, inorganic materials, and unidentified materials (of solid forms), which have been used for preliminary investigations, cause of death and tracking suspects. When suspects or related individuals are narrowed down, chemical composition analysis is utilized for a composition identity test to compare the evidences from the crime scene with those which acquired from the suspects. Also, In order to perceive whether there are toxic chemicals in the environment of industrial field or the scene of accident, we need an analysis method that can rapidly quantify and qualify the toxic chemicals for the cause of the death. Though the analysis techniques for forensic evidence are used, the crimes increase along with their behaviors and concealments becoming highly intelligent. Moreover, the crimes become faster, wider and more violent, and scientific investigation becomes indispensable to acquire clear evidences because it becomes more limited to acquire evidences through witnesses and legworks due to individualism and anonymity of the developed societies. In addition, the type of forensic evidence from the crime scenes gets more divergent, and much attention has been given to the analysis techniques that can determine the identities of suspects and primary cause of death. It is

important to select evidences that can specify criminals, clarify the case and determine the authenticity among numerous evidences found at the crime scenes, which is essential for forensic evidences.

1.2. On-site Colorimetric Sensor for Forensic Application.

1.2.1 Summary

Highly toxic gas such as hydrogen sulfide and ammonia gas is generated as a product or by-product in the industrial site, manufacturing process, and space where human artificial technology is mobilized.³ This generation of toxic gas may cause a fatal accident to human beings and takes the life of person in a moment. Many studies of effectively detecting and monitoring the toxic gas as soon as possible have attracted attention for a long time from the biological or industrial viewpoint due to the toxicity of toxic gas.⁴ Hydrogen sulfide gas is known as a deadly gas due to poisoning, environmental poisoning, etc. in the course of industrial process and operation in the confined space at work. In case a person inhales the hydrogen sulfide gas, blood is poisoned. And a phenomenon of alveolus rupture, blister, etc. occurs. And cognitive and olfactory abilities are lost. And in case of inhaling the gas in the concentration of 1000 ppm or more in air, human beings die immediately.^{5,6} And in case hydrogen sulfide concentration in blood is 5 ppm or more, this is fatal, and human beings will die in the end. Similarly to this, in case of being exposed to the ammonia gas concentration of 5000 ppm in air, human beings are put to death immediately due to the skin damage, cornea damage, organ damage, and difficulty in breathing. The actual condition is that we need a detection method that is rapid, and has high sensitivity, and has high mobility, and is simple and reliable due to the fatal toxicity of these toxic gases. Besides, we need a method which can make an analysis in gaseous state, solution state, and blood so as to make it possible to be applied to medical, forensic science, and industrial field. Until now, several analysis methods have used titration method, spectroscopic analysis method, electrochemical analysis method, and chromatography technology.^{7, 8, 9, 10, 11, 12}

However, these conventional analysis methods can make an analysis, being limited to a sample in air or a sample in liquid and blood state. In case of the conventional analysis method using Membrane filter and Micro diffusion Method traditionally used for the analysis of hydrogen sulfide concentration in blood, it is possible to analyze concentration up to 0.1 ppm.^{13, 14} However, there is a disadvantage of inferior reproducibility. Titration method requires simple equipment, but has low detection sensitivity.^{15, 16} Other methods consist of complex equipment, expensive equipment, and complex chemical compound to react with and detect a toxic gas. In order to detect ammonia gas, ion chromatography and sensor to measure electric resistance by using metal oxide semiconductor is used, and an organic compound etc. are used. However, this method also has a disadvantage of being operated at high temperature. And economically, it should be provided with expensive equipment. Therefore, this study developed a sensor necessary for the detection of toxic gas by using the colorimetric method, which could simultaneously analyze a sample of gas in air and blood sample, and would be simple device, and would be economical and highly sensitive. The analysis method of this sensor is what uses surface-modified silica particle with metal cation by using sulfonate silica gel, and can rapidly and accurately detect toxic gas by using the chemical reaction that cause the color to change if the particle reacts with toxic gas (hydrogen sulfide, ammonia) inside the tube. Besides, it is possible to detect toxic gas at low concentration as well as toxic gas at a concentration in air, which may cause death. And in a blood sample, it is possible to obtain the same results as that of detection limit concentration (0.1 ppm) in comparison with the conventional analysis method. And reproducibility is developed. As a result, it is possible to make an analysis regardless of type of sample. And this doesn't require sample preparation,

analysis duration, and special chemical reaction condition, and expensive and complex equipment, and this can be used as rapid and accurate detection method. Besides, this chemical reaction of color change isn't affected by the environmental factors such as temperature and humidity. And it is possible to be detected by the reaction with a specific toxic gas within short reaction time. In addition, colorimetric sensor can be directly utilized as real-time detection method at the scene of an accident etc. which happen in the workplace, by using the advantage of mobility.

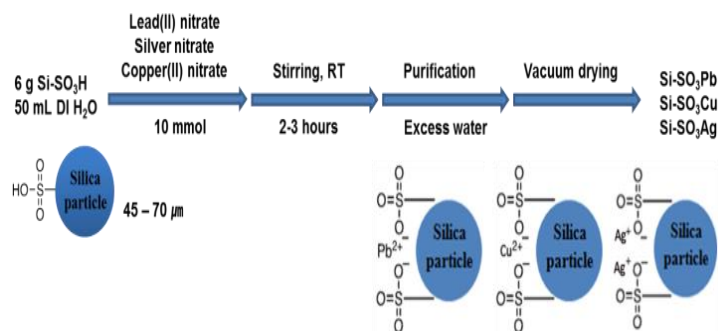


Figure 1-1. Preparation of metal-cation-modified silica powders.

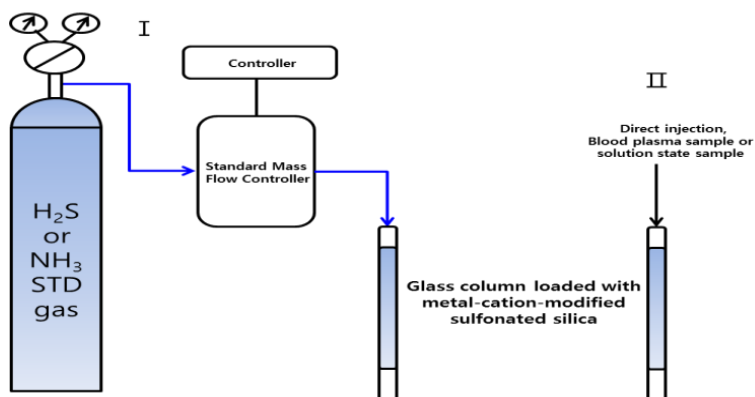


Figure 1-2. Experimental settings for detecting (I) H₂S or NH₃ gases, and (II) S²⁻ ion by metal-cation-modified sulfonated silica powders.

1.2.2 Scope of Dissertation

Hydrogen sulfide is a colorless and fatally poisonous gas, and has an unpleasant odor, but is known as a gas indispensably emitted in the process of industry, manufacturing industry, and waste disposal. If S^{2-} , sulfide ion, is exposed to strong acid or acidic environment, hydrogen sulfide gas is emitted. And because this is emitted in gaseous state, it is difficult for people to perceive this. And this can be recognized through odor, but this has high toxicity even at very low concentration. Therefore, we need a method which makes it possible to accurately and rapidly detect even a very small amount of gas in blood in case artificial detection system and human beings suck the gas.

In order to perceive whether there is toxic gas in air in the environment of industrial field or the scene of accident, we need an analysis method that can rapidly quantify and qualify the gas. At the scene, a direct analysis method is indispensable because it is difficult to preserve the scene even though the space is confined. Partly, a sensor, etc. to detect a toxic gas in air are known. However, the actual condition is that we lack a method which can directly bond a substance to real toxic gas ingredients by using direct chemical bond and can make a qualitative and quantitative analysis through the colorimetric method.

Besides, in order to detect various toxic gases emitted in the underground space, industrial space, and so on, a simple and mobile analysis method is necessary. After a certain amount of sample in air is made to flow, in case of being bonded to a specific toxic gas ingredient, it must be possible to qualitatively identify the toxic gas which displays a certain color, and we need a method which can quantitatively and rapidly make an analysis according the changed length. A color is immediately shown to change when a specific toxic gas ingredient is chemically bonded to the substance on the surface of silica

by using a surface-modified silica particle with metal cation as the support in order to satisfy these conditions of method. And besides, it is possible to make a quantitative analysis by using a difference in the length of color change of silica particle according to the toxic gas concentration in case of being bonded to a specific toxic gas ingredient. Therefore, it is possible to grasp whether there is a fatal amount of toxic gas to human beings as well as toxic gas ingredient in air.

In case of being poisoned by hydrogen sulfide, there is sulfide ion in blood. And diffusion method has been used as a method of detecting the sulfide ion concentration. Diffusion method uses a device divided into two sections inside the closed circular cell. And blood and strong acid of 10 % is added to the circular outer section, and hydrogen sulfide gas is generated, and it uses a method where NaOH, strong base, captures the generated gas in the inner section, and the gas is detected by using UV and so on through ion chromatography and preparation process. This is a method of generating the hydrogen sulfide gas by adding a strong acid to blood. And the method goes through a process where its phase changes from liquid state of blood to the gaseous state of hydrogen sulfide by the method of adding an excess strong acid to the solution state which contains sulfide ion in blood, and hydrogen sulfide in gaseous state is captured by the strong base in liquid state again. That is to say, because strong acid and strong base is used as excess in the process of phase change of liquid \rightarrow gas \rightarrow liquid, the process of capture may lead to a loss of hydrogen sulfide gas and sulfide ion that they intend to detect. As a result, this method has difficulties of degrading the reproducibility in the final results of sulfide ion concentration, and losing the reliability of results especially in case of a very small amount. Besides, an analysis is made by using ion chromatography of the sample obtained by the separation of blood

plasma in the supernatant state from blood with a membrane filter. This method makes it possible to give a qualitative and quantitative analysis of chromatography. However, there is difficulty in experimentally giving an accurate quantitative analysis because sulfide ion may easily volatilize in the form of hydrogen sulfide within a short period of time from the blood sample.

We introduced a support of surface-modified silica with metal cation by using the colorimetric method in order to develop a detection method which can rapidly and accurately check whether there is toxic gas in air sample, and can identify the type of toxic gas and can give a quantitative analysis, and can supplement experimental error limit in the process of using strong acid and strong base and changing phase in many steps and in the process of capture so as to analyze blood and water solution sample, and can rapidly and accurately detect toxic gases and toxic chemicals from sample of gas in air, sample in water solution state, and blood sample.

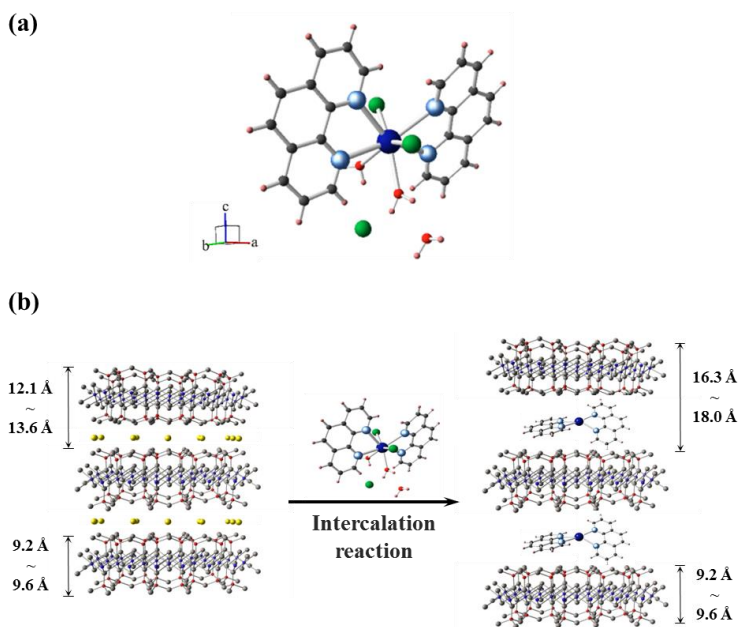
1.3. Nanocomposite materials for Forensic Application.

1.3.1 Summary

Earlier, the database for fingerprints and DNA was introduced as a new method to identify criminals, which has changed investigations to be based on evidences rather than on confession. The evidences acquired by the scientific methods have been adopted more frequently as forensic evidences, and scientific investigation and forensic analysis techniques have been changed to make acquired scientific investigation data more searchable. One of the requirements of forensic evidences are whether one is directly applicable to identify and trace suspects or not, and microscopic traces found from evidences such as fingerprints and contact marks can be regarded as the most important forensic evidences. Microscopic traces, such as fingerprint and contact marks, can be found from evidences at the crime scene, which can be used for individual identification. In particular, fingerprints of humans are different from one another where the probability of identical fingerprints found from different individuals is one in a billion. Furthermore, one's fingerprints do not change over time, and it has gained credibility as much as DNA identifications. As such, fingerprints have been one of the most widely used methods for the forensic identification of individuals since the 19th century.

Until now, there have been many literatures that introduced various methods that employed physical and chemical analysis to develop fingerprints.¹⁷ This study suggested two-dimensional nano-composites that exhibited stable fluorescence to visualize microscopic traces and latent fingerprints. Firstly, europium complexes were synthesized to express fluorescence, which was intercalated between two-dimensional inorganic clay compounds by the ion exchange method. The two-dimensional nano

structures synthesized as such showed better chemical stability than the organic europium complex as it was, and exhibited the same fluorescence characteristics. The synthesized materials were examined by x-ray diffraction and infrared analysis, which showed the europium complexes were intercalated between the two-dimensional nano-structure and chemically stable. The two-dimensional hybrid materials of the stabilized europium complexes showed the same fluorescence characteristics, which was applicable for individual identification from the development test on latent



fingerprints.

Figure 1-3. Schematic representation of (a) molecular crystal structure of Eu(III) complex and (b) $[\text{Eu}(\text{Phen})_2]^{3+}$ -clay mineral hybrids.

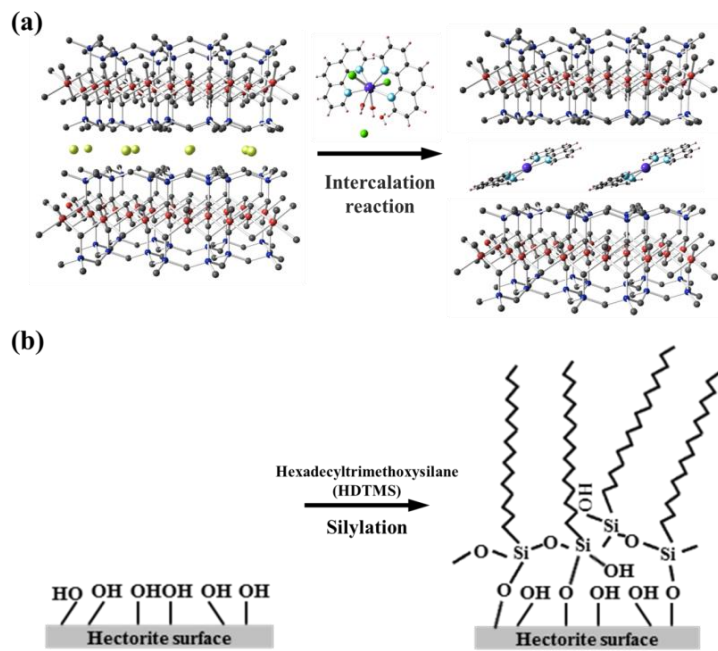


Figure 1-4. Schematic representation of (a) intercalation reaction for [Eu(Phen)₂]³⁺-montmorillonite/hectorite nanocomposites and (b) silylation for [Eu(Phen)₂]³⁺-hectorite-HDTMS nanocomposite.

1.3.2 Scope of Dissertation

Along with crimes increase in the highly industrialized society, their behaviors and concealments become more intelligent. Moreover, crimes in the modern society become faster, wider and more violent, and scientific investigation is indispensable to acquire clear evidences as it becomes more limited to acquire them through witnesses and legworks due to individualism and anonymity of the developed society. Scientific investigation also becomes a general method for investigations as crimes become divergent, intelligent, wide and international, which calls for scientific methods for investigation. Especially, scientific investigation can be used to acquire critical information such as the identification of criminals and the collection and analysis of

evidences. New methodologies have been introduced to scientific investigations, and the utilization of database for fingerprints and DNA makes the investigation based on evidences rather than on confessions. These scientific evidences are more likely accepted as proofs by the court, and it becomes important to make investigation data informatized.

Microscopic traces such as fingerprints and contact marks used for individual identifications can be found at the crime scenes. In particular, fingerprints of humans are different from one another where the probability of identical fingerprints found from different individuals is one in a billion. Furthermore, one's fingerprints do not change over time, and it has gained credibility as much as DNA identification. As such, fingerprints have been one of the most widely used methods for the forensic identification of individuals since the 19th century.

Most of fingerprints can be visualized by illuminating alternate light sources after applying detection chemicals or spraying powders.^{18, 19} Chemicals for the detection can be selected depending on the type of contact matrixes, such as porous materials, nonporous materials and adhesive materials.

For porous materials like paper, iodine fuming, DFO (1,8-Diazafluoren-9-one), ninhydrin, silver nitrate and physical developer can be used. For nonporous materials, superglue and vacuum metal deposition can be used, while gentian violet used for adhesive materials. In addition to those, recent studies have reported possible applications of mercury, cadmium, titanium, lead and manganese.

It has been reported, however, that conventional detection chemicals could not visualize microscopic traces and makes it impossible to acquire individual identification from microscopic traces or circumstantial evidences from

contact marks. Also the toxicity of inorganic salts to the investigator has been reported when titanium, mercury and lead were used. Therefore, this study suggested introducing a new forensic individual identification method, which used a new functional nano-particle that could visualize microscopic traces of various chemical characteristics of contact matrixes.²⁰ In particular; the new material was designed to differentiate itself from the contact matrix as it contained fluorescent materials that emitted light of specific wavelength, especially in the UV region. Various combinations of lanthanides and ligands were tried to improve fluorescence characteristics.^{21, 22, 23} Surface modification of fluorescent materials was examined to increase adhesion with the traces, while magnetic nano-particles were applied to prevent damage to the traces.

Recently, nanohybridization and nanocomposites made from various nano materials have attracted much interest.^{24, 25} The combination can make the shape and dimension of materials in the nanometer scale so that the physical and chemical characteristics of nano-particles can be fine-tuned. Furthermore, the combinations of two or more kinds of materials with different chemical structures and functionalities enable expressions of new characteristics due to their combinations in the nanometer scale in addition to their original characteristics. This new features of nano-composites have been studied widely according to their applications.^{26, 27}

Lanthanide compounds, which shows photonic activity, such as europium, show strong fluorescence due to their strong stokes shift, long fluorescence lifetime, and distinct emission band, and have been studied for various fields such as laser, phosphor and electronic optical devices. The color of emitted light from lanthanide compounds depends on the lanthanide core metal. For example, the Eu^{3+} and Tb^{3+} ions emit red and green lights, respectively, and most of them are trivalent. A lanthanide ion itself, however, generally shows

weak fluorescence, and it is combined with ligands that strongly absorb light to overcome the shortage. The ligands transfer the absorbed light to the lanthanide ion so that it exhibits stronger fluorescence, which is called as an 'antenna effect.'

Though lanthanide compounds can acquire strong fluorescence due to an 'antenna effect,' the compounds are not suitable for practical applications as they are not thermally and mechanically stable which limits processing. Especially the fluorescence is quenched by absorbing humidity in the air. In order to prevent fluorescence quenching due to the vibration of absorbed water molecules and to increase processing capability of the compounds, recent studies have been done on nano-hybrid materials that combine lanthanide compounds with various matrixes such as polymer, aluminosilicate and micro- and mesoscopic porous materials.

In particular, the study on two-dimensional nano-particles was very important as they could make a complex when combined with other nano-materials and be used as precursors for various applications such as multi-layer films, hetero-catalysts and porous nano-hybrid materials. Among the two-dimensional materials, clay minerals have been mostly studied as they were inorganic materials which exhibited negative charges and had cation exchange capability. Cation complexes could be intercalated between the layers of clay minerals through cation exchange capability, which made the intercalated materials stable from thermal, chemical and mechanical stress due to the electrostatic attractive force in the inorganic layers. This study focused on montmorillonite as a natural clay mineral and hectorite as artificial one to be combined with lanthanide compounds to make them stable and protect from water molecules so that the quenching was prevented.

In order to make the material useful for fingerprint development, the

surface of the nano-hybrid materials for the intercalation, or the clay minerals, was modified with various materials. The polarity of fingerprints was classified by the characteristics of the contact matrix surface and the deposited time, for which suitable detection chemicals were produced, respectively.

1.4 Fluorescent Inorganic Nanomaterials for Forensic Application.

1.4.1 Summary

QDs of good emission characteristics were coated with polyvinylpyrrolidone (PVP), to which silica shells were introduced by a modified Stober method. The emission characteristics of QD@SiO₂ did not change during the process, which exhibited strong emission after the process. It could be employed for fluorescence labeling markers to visualize latent fingerprints for individual identification for scientific investigation since the synthesis of the QD@SiO₂ was simple while showing strong emission.

Many studies have been reported that introduced various materials and methods to visualize microscopic traces.^{27, 28, 29} However, the success rate of such methods has remained less than 50% in practical applications. Though there have been many suggestions for new materials and methods, it could not be employed for practical applications because either the materials were not mass-producible or their applicability in the crime scene was limited. Hence, the detect ability on microscopic traces is expected to be improved if the material is made from nano materials that exhibit good emission and have functionality that can interact with microscopic traces, which will lead to better sensitivity and selectivity on microscopic trace detection.^{30, 31}

A detection method is to be established that uses nano-particles whose fluorescence characteristics are maximized compared with conventional fluorescence materials for microscopic trace visualization.

The detection limitation is to be overcome by the improved resolution and sensitivity of the microscopic trace visualization that employs fluorescent nano-particles with an increased interaction with the traces by surface treatments.

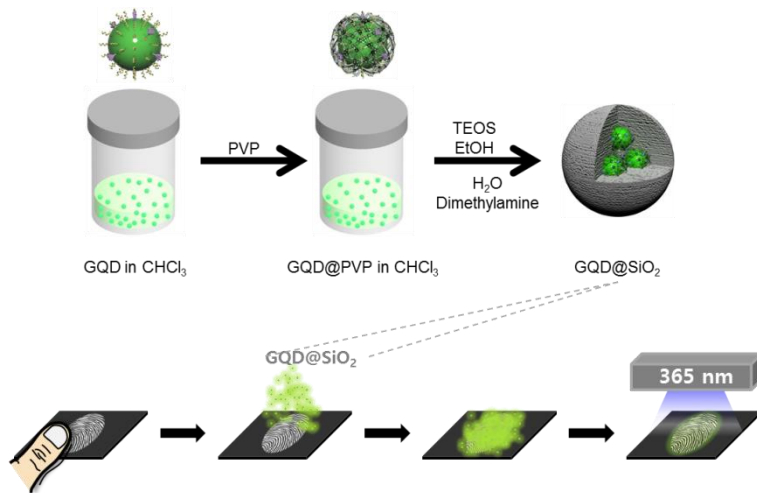


Figure 1-5. Schematic representation of synthesized GQD@SiO₂ nanoparticles and latent fingerprint detection.

1.4.2 Scope of Dissertation

The limitations on the detection of microscopic traces found in the crime scenes can be overcome by the excellent emission of the nano-particles. Moreover, its sensitivity can be improved by introducing new materials to the nano-particles that can interact with the surface of the traces. This method is expected to improve the arrest rate of criminals as forensic individual identification becomes more effective. This will lead to a lower criminal rate that enables more effective social security as criminals or likely will be alerted.

Semiconductor quantum dots (QDs) show strong fluorescence as they have 100 to 1000 times absorption coefficients, compared with typical dyes, along with high quantum efficiency. They also can be adjusted to emit fluorescence in the visible region as the wavelength depends on the size of the particles. The photoluminescence (PL) spectra can be controlled due to its narrow PL spectra and one excitation wavelength, and various studies have been done to apply this to energy conversion, optical device, and especially to biological imaging. Generally QDs are synthesized in non-polar organic solvents of high boiling points to acquire single crystals of high quantum efficiency and narrow size distribution, which has been widely used as it can achieve high quantum efficiency that minimizes surface bonding compared with other methods can.^{32, 33} However, the QDs produced by the method have many hydrophobic ligands on their surface and are only dispersed with organic solvents, and it requires the surface treated with appropriate materials to make them dispersed with solvents like water or alcohols to improve their applicability as optical materials for biological imaging. Hence, it is important to modify the surface while maintaining the fluorescence characteristics as the QDs are prone to surface damages which reduces the efficiency significantly. It has been attracted interests of many researchers to use QDs as fluorescence labeling marks for latent fingerprint visualization. Menzel et al. reported an example that used QDs for latent fingerprint visualization for the first time. Afterwards, most of the researches have focused on the applications of synthesized QDs, in the form of semiconductor powder or that dispersed in water, and II-VI semiconductor QDs, such as CdS, CdSe and CdTe, for fluorescence labeling marks for latent fingerprint visualization.^{34, 35, 36} Various studies have been reported that modified the surface of QDs to adapt to diverse applications^{37, 38, 39}, among which ligand exchange methods and QDs

coated with amphiphilic polymer were the most representative ones. As a method to make the surface of QDs hydrophilic, introductions of silica shells to the QD surface has been studied by many researchers as well. Silica shells can be formed easily through a hydrolysis-condensation reaction of tetraethyl orthosilicate (TEOS) as a precursor with either acid or basic catalysts. Furthermore, the surface of silica shells can be treated by various organosilicon compounds, and it is easy to make the surface treated with ligands that can interact with microscopic traces. It also has biocompatibility without toxicity, and hence is one of the most widely used materials for nano-material formations.^{40, 41}

A typical method to form QD@SiO₂ nano-particles is a reverse micelle method of water-in-oil, which easily controls the aggregation of QDs in the core. However, it requires multiple steps such as a ligand exchange reaction, and cannot avoid probable surface damages nor make it scalable as it is inevitable to use a specific process that makes the hydrolysis and condensation of TEOS on the surface of QDs.

In this study, amphiphilic polymers such as polyvinylpyrrolidone (PVP) were directly adsorbed onto the surface of semiconductor QDs to overcome the limitations described above. Also, silica shells were introduced to the QDs to synthesize QD@SiO₂ which maintains PL efficiency. QD@SiO₂ synthesized by a modified Stober method was appropriate for latent fingerprint visualization as it maintained very strong emission efficiency as well as biocompatibility due to the silica shells on the surface.

1.5. References

1. R. Saferstein, Forensic science from the crime scene to the crime lab, second edition, **2013**, Pearson education, Inc.
2. M. M. Houck, J. A. Siegel, Fundamentals of forensic science, second edition, **2010**, Elsevier Ltd.
3. T. Zhou, N. Wang, C. H. Li, H. Y. Yuan, D. Xiao, *Anal. Chem.* **2010**, *82*, 1705.
4. A. Christia-Lotter, C. Bartoli, M. D. Piercecchi-Marti, D. Demory, A. L. Pelissier-Alicot, A. Sanvoisin, G. Leonetti, *Forensic. Sci. Int.* **2007**, *169*, 206.
5. A. K. Chaturvedi, D. R. Smith, D. V. Canfield, *Forensic. Sci. Int.* **2001**, *123*, 211.
6. Z. Pawlak, A. S. Pawlak, *Talanta* **1999**, *48*, 347.
7. J. M. Davidson, Z. Pikramenou, A. Ponce, R. E. Winpenny, *Anal. Chem.* **2009**, *81*, 3669.
8. X. F. Yang, L. Wang, H. Xu, M. Zhao, *Anal. Chem.* **2009**, *631*, 91.
9. K. Han, W. F. Koch, *Anal. Chem.* **2009**, *59*, 1016.
10. K. Maebashi, K. Iwadate, K. Sakai, A. Takatsu, K. Fukui, M. Aoyagi, E. Ochiai, T. Nagai, *Forensic. Sci. Int.* **2011**, *207*, 91.
11. J. Xu, Q. Pan, Y. Shun, Z. Tian, *Sensor. Actuat. B-Chem.* **2000**, *66*, 277.
12. C. N. Xu, N. Miura, Y. Ishida, K. Matsuda, N. Yamazoe, *Sensor. Actuat. B-Chem.* **2000**, *65*, 163.
13. W. Puacz, W. Szahum, K. Linke, *Analyst* **1995**, *120*, 939.
14. K. Maebashi, K. Iwadate, K. Sakai, A. Takatsu, K. Fukui, M. Aoyagi, E. Ochiai, T. Nagai, *Forensic. Sci. Int.* **2011**, *207*, 91.
15. A. K. Chaturvedi, D. R. Smith, D. V. Canfield, *Forensic. Sci. Int.* **2001**, *123*, 211.
16. E. O'malley, E. J. Conway, O. Fitzgerald, *Biochem. J.* **1943**, *37*, 278.

17. Cui, Y., Yue, Y., Qian, G., Chen, B., **2012**. Luminescent functional metal-organic frameworks. *Chem. Rev.* 112, 1126-1162.
18. Eliseeva, S.V., Bünzli, J.-C.G., **2010**. Lanthanide luminescence for functional materials and bio-sciences. *Chem. Soc. Rev.* 39, 189-227.
19. Gao, F., Lv, C., Han, J., Li, X., Wang, Q., Zhang, J., Chen, C., Li, Q., Sun, X., Zheng, J., Bao, L., Li, X., **2011**. CdTe-montmorillonite nanocomposite: control synthesis, UV radiation-dependent photoluminescence, and enhanced latent fingerprint detection. *J. Phys. Chem. C* 115, 21574-21583.
20. Guo, X., Fu, L., Zhang, H., Carlos, L.D., Peng, C., Guo, J., Yu, J., Deng, R., Sun, L., **2005**. Incorporation of luminescent lanthanide complex inside the channels of organically modified mesoporous silica via template-ion exchange method. *New J. Chem.* 29, 1351-1358.
21. Hagerman, M.E., Salamone, S.J., Herbst, R.W., Payeur, A.L., **2003**. Tris(2,2'-bipyridine)ruthenium(II) cations as photoprobes of clay tactoid architecture within hectorite and laponite films. *Chem. Mater.* 15, 443-450.
22. Jenkins, A.L., Murray, G.M., **1998**. Enhanced luminescence of lanthanides: determination of europium by enhanced luminescence. *J. Chem. Ed.* 75, 227-230.
23. Jin, T., Tsutsumi, S., Deguchi, Y., Machida, K., Adachi, G., **1997**. Preparation and luminescence characteristics of the europium and terbium complexes incorporated into a silica matrix using a sol-gel method. *J. Alloys Comp.* 252, 59-66.
24. Jung, H., Kim, H.M., Choy, Y.B., Hwang, S.J., Choy, J.H., **2008a**. Laponite-based nanohybrid for enhanced solubility and controlled release of itraconazole. *Int. J. Pharm.* 349, 283-290.
25. Jung, H., Kim, H.M., Choy, Y.B., Hwang, S.J., Choy, J.H., **2008b**. Intraconazole-laponite: kinetics and mechanism of drug release. *Appl. Clay*

Sci. 40, 99-107.

26. Jüstel, T., **2008**. Phosphors for plasma display panels, in : Ronda, C.R., (Eds.), *Luminescence: From theory to applications*, Willey-VCH Verlag GmbH & Co. KGaA, Weinheim, Germany, pp. 61-73.
27. Khan, A.I., O'Hare, D., **2002**. Intercalation chemistry of layered double hydroxides: recent developments and applications. *J. Mater. Chem.* 12, 3191-3198.
28. N. Jaber, A. Lesniewski, H. Gabizon, S. Shenawi, D. Mandler, J. Almog, *Angew. Chem. Int. Ed.* **2012**, 51, 12224.
29. M. Wood, P. Maynard, X. Spindler, C. Lennard, C. Roux, *Angew. Chem. Int. Ed.* **2012**, 51, 12272.
30. J. Yu-Juan, L. Yun-Jun, L. Guo-Ping, L. Jie, W. Yuan-Feng, Y. Rui-Qin, L. Wen-Ting, *Forensic Sci. Int.* **2008**, 179, 34.
31. Y. F. Wang, R. Q. Yang, Y. J. Wang, Z. X. Shi, J. J. Liu, *Forensic Sci. Int.* **2009**, 185, 96.
32. J. Dilag, H. Kobus, A. V. Ellis, *Forensic Sci. Int.* **2008**, 187, 97.
33. A. Becue, S. Moret, C. Champod, P. Margot, *Forensic Sci. Int.* **2009**, 191, 36.
34. J. Liu, Z. Shi, Y. Yu, R. Yang, S. Zuo, *J. Colloid Interf. Sci.* **2010**, 342, 278.
35. E. R. Menzel, S. M. Savoy, S. J. Ulvick, K. H. Cheng, R. H. Murdock, M. R. Sudduth, *J. Forensic Sci.* **2000**, 45, 545.
36. E. R. Menzel, M. Takatsu, R. H. Murdock, K. Bouldin, K. H. Cheng, *J. Forensic Sci.* **2000**, 45, 770.
37. K. K. Bouldin, E. R. Menzel, M. Takatsu, R. H. Murdock, *J. Forensic Sci.* **2000**, 45, 1239.
38. F. Gao, J. Han, C. Lv, Q. Wang, J. Zhang, Q. Li, L. Bao, X. Li, *J. Nanopart. Res.* **2012**, 14, 1191.

39. B. E. Dalrymple, J. M. Duff, E. R. Menzel, *J. Forensic Sci.* **1977**, 22, 106.
40. F. Gao, C. Lv, J. Han, X. Li, Q. Wang, J. Zhang, C. Chen, Q. Li, X. Sun, J. Zheng, L. Bao, X. Li, *J. Phys. Chem. C* **2011**, 115, 21574.
41. F. Gao, J. Han, J. Zhang, Q. Li, X. Sun, J. Zheng, L. Bao, X. Li, Z. Liu, *Nanotechnology* **2011**, 22, 075705.

Chapter 2

***On-site* Colorimetric Forensic Sensor (I):**

Quantitative Detection of Toxic H₂S and NH₃

Gases using Metal-Ion-Modified Silica Powders

2.1. Abstract

A highly sensitive *on-site* colorimetric forensic sensor has been developed for the quantitative detection of hydrogen sulfide and ammonia gases. The sensor consists of metal-ion-modified silica-gel powders placed in a glass tube. The powder color changes upon reaction with toxic hydrogen sulfide and ammonia gases. It is capable of easily detecting toxic gases in the concentration range between 100 ppm, which is considered as immediately dangerous to life and health, and 3000 ppm, which may cause death, by using a glass tube with an inner diameter of 3 mm. Since the sensor reported here is insensitive to environmental conditions such as temperature or humidity, and is featured by simplicity, fast response, high sensitivity, and easily understandable results based on absolute affirmative/negative response, it is expected to be effectively used for *on-site* applications such as testing the existence of toxic gases in confined working and industrial spaces.

2.2. Introduction

Highly toxic gases such as hydrogen sulfide (H_2S) and ammonia (NH_3) are generated both by nature and by human activities, and in particular, as products or by-products in the chemical industry.¹ H_2S is a colorless and fatally poisonous gas with an unpleasant odor, and it is unavoidably emitted in processes in the manufacturing industry and in relation to waste disposal.^{2,3} H_2S gas is known as an extremely harmful gas due to its toxicity to human beings and to the environment; The U. S. Occupational Safety & Health Administration (OSHA) acceptable ceiling concentration for H_2S is 20 ppm. The National Institute for Occupational Safety and Health (NIOSH) sets the recommended exposure limit (REL) for H_2S to 10 ppm for 10 min, and the concentration of H_2S considered as immediately dangerous to life and health (IDLH) is 100 ppm.⁴ The IDLH is the level to which a healthy worker can be exposed for 30 min without suffering irreversible health effects. The U. S. OSHA has set a 15 min REL of 35 ppm by volume and an 8 h REL of 25 ppm by volume for gaseous NH_3 in air.⁵ In 1994, NIOSH reduced the IDLH for NH_3 from 500 ppm to 300 ppm based on recent more conservative interpretations of an original study done in 1943.⁶

Several techniques have been developed to determine H_2S concentrations, such as titrimetric,⁷ spectroscopic,⁸ electro-chemical,⁹ and chromatographic¹⁰ techniques. The titrimetric method utilizes a simple apparatus but is less sensitive. Spectroscopic and electrochemical techniques require complex chemical compounds for sulfur to react with while chromatographic techniques require expensive equipment and complicated sample pretreatment and preparation processes.^{11,12} Various types of sensors for gaseous NH_3 have also been proposed such as those based on a change in the electrical resistance using metal oxide semiconductors^{13,14} as well as those based on a quartz

micro balance¹⁵ and organic compounds.¹⁶ However, these methods are associated with disadvantages such as the requirement of a high operating temperature and expensive experimental set-up processes.^{17, 18, 19}

To detect the existence of toxic gases in the environments in industrial fields, underground spaces, and the scene of accidents, it is desirable to have access to an analysis method that can rapidly quantify and qualify these gases. Specially, in consideration of the suicidal wave related with H₂S gas which can easily be produced by mixing certain household materials^{20, 21} it is necessary to protect first responders, such as emergency service workers or family members, from the risk of death by inhaling lethal quantities of the gas or by fire.²² Under such circumstances, a direct analysis method is indispensable because it is difficult to preserve evidence at the scene, even if the space is confined. Although various gas sensors able to detect toxic gases in air are known, there is a lack of a detection method that is rapid, simple, and reliable and has high sensitivity as well as portability. Ideally, such a sensor should be able to bond to directly toxic gases by strong and selective chemical interactions,^{23, 24, 25} and make qualitative and quantitative analyses possible through simple and straightforward color changes.

We have developed a highly sensitive colorimetric sensor based on metal-ion-modified silica powders, which change color upon exposure to toxic species. This sensor consists of metal-cation-bound silica powders placed in a glass tube. The color of the powders changes if either a precipitation reaction or a complex ion formation reaction occurs in the presence of H₂S or NH₃ gas. The simple preparation method of the sensor eliminates time-consuming sample preparation and pretreatment processes, the need for special reaction conditions, and expensive complicated laboratory apparatuses. Because the sensor is not affected by environmental conditions such as the temperature or

humidity, and given that it offers simplicity, a fast response, high sensitivity and portability, it can be directly used in many on-site or in-situ applications.

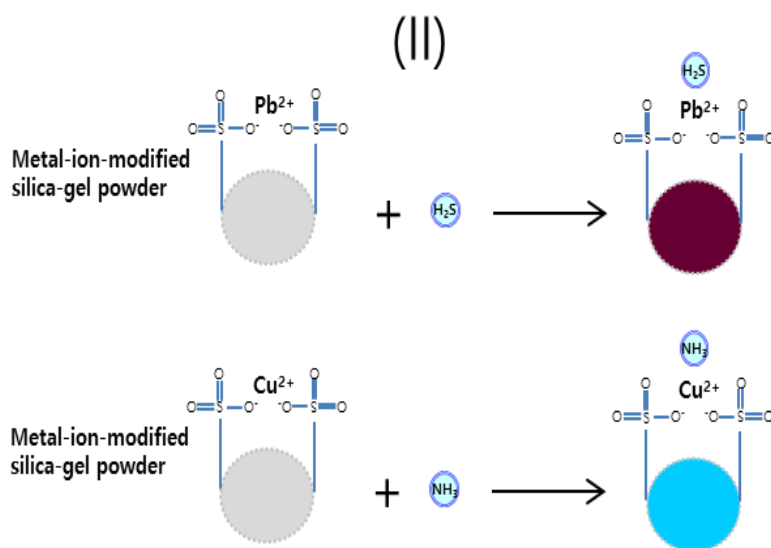
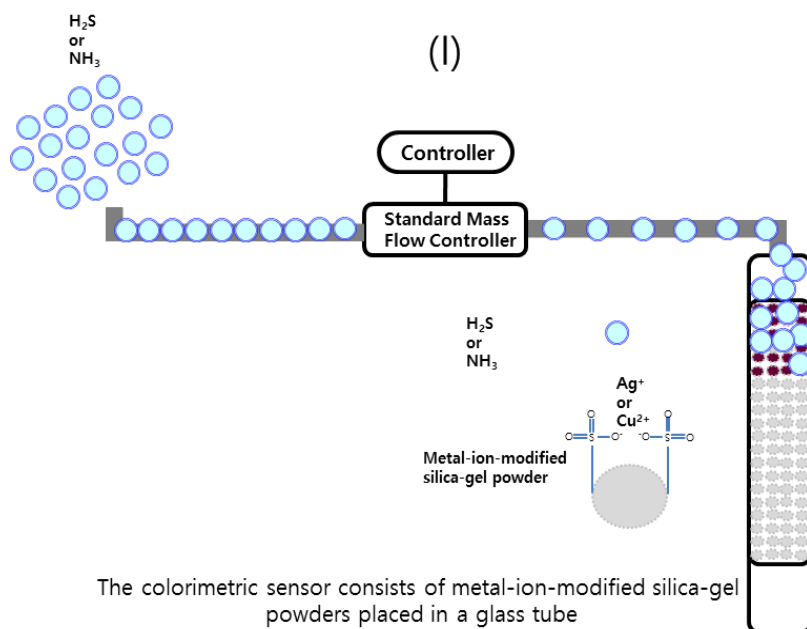
2.3. Experimental Section

Reagents and chemicals. Silver nitrate (AgNO_3 , 99%) and cupric nitrate hydrate ($\text{Cu}(\text{NO}_3)_2 \cdot 2.5\text{H}_2\text{O}$, 98%) were purchased from Sigma Aldrich. Silica gel 60 for column chromatography (SiO_2 , 0.063-0.2 mm) and sulfonated silica gel for column chromatography ($\text{SiO}_2\text{-SO}_3\text{H}$, 45-70 μm) were obtained from Merck Chemicals and Fuji Silysia Chemical Ltd., respectively. $\text{H}_2\text{S}/\text{N}_2$ and NH_3/N_2 standard gases of 100, 300, 500, 1000, 2000 and 3000 ppm ($\pm 2\%$) were purchased from Daedeok Gas Co. Standard Mass Flow Controllers such as MODEL 3660 series were purchased from KOFLOC Co. The standard gases were manufactured by according to ISO9001 and ISO14001 requirements. All reagents and chemicals were used as-received without further purification.

Preparation of silver- and copper-modified silica powders. Appropriate metal nitrate (10 mmol) was dissolved in 50 mL of deionized water in a 100 mL one-neck round bottle flask. After the metal nitrate was completely dissolved, 6.0 g of sulfonated silica gel was added and the mixture was stirred at room temperature for 3 h. The solid was then washed and purified with deionized water three times by using centrifugation at low rpm (2,000 rpm, 10 min) to remove excess free metal cations. Dried silver-, and copper-modified sulfonated silica powders were obtained by vacuum drying at 60 °C for 3 h, and the solids were then stored in a glass vial for further use. To prepare the sensors for appropriate gases, the bottom side of each glass column with an inner diameter of 3 mm and a length of ~100 mm was clogged with cotton wool, and loaded sequentially with silica gel 60, metal-ion-modified silica powder, and silica gel 60 again to make the sandwich type

packing. The top side was clogged with cotton wool to complete the set-up of the sensor columns.

Detection of H₂S and NH₃ gases. H₂S/N₂ standard gases of 100, 300, 500, 1000, 2000, and 3000 ppm ($\pm 2\%$) were connected to the Standard Mass Flow Controller, and then the mixed gases were allowed to pass through the packed column of Ag-modified silica powders to form a black precipitate of silver sulfide. The flow rate of the mixed gases containing H₂S was 30 mL/min and flow time was set to 15 min. The band widths of the area of silver sulfide precipitate were measured. Similarly, NH₃/N₂ standard gases of 100, 300, 500, 1000, 2000, and 3000 ppm ($\pm 2\%$) were connected to a Standard Mass Flow Controller, and then the mixed gases were allowed to pass through the packed column of Cu-modified silica powders to form a copper-ammonia complex having royal blue color (Scheme 2-1). The flow rate of the mixed gases containing NH₃ was 30 mL/min and flow time was set to 30 min. The band widths of the area of the royal blue copper-ammonia complex were measured. All experiments were performed three times and the average values were reported with the standard deviation.



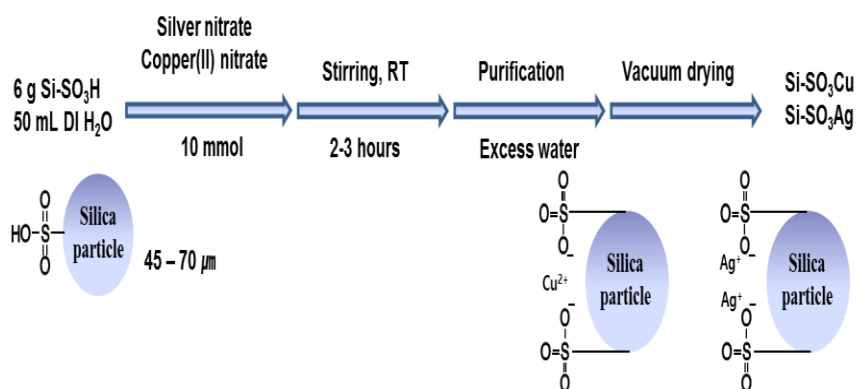
The powder color changes upon reaction with toxic H₂S or NH₃

Scheme 2-1. Experimental settings of the colorimetric sensor for detecting H₂S or NH₃ gases (I) and reaction mechanism of color change between toxic H₂S, NH₃ gases and metal-cation-modified sulfonated silica powders (II).

Characterization. The size and morphology of the metal-cation-modified silica powders were measured using a scanning electron microscope (SEM, Hitachi S-4300). The presence of silver, and copper after surface modification of the sulfonated silica powders was confirmed by energy dispersive X-ray spectrometry (EDX, Carl Zeiss Supra 55VP).

2.4. Results and Discussion

Sensing materials for H₂S or NH₃ gas were prepared by surface modification of sulfonated silica powders with various metal cations according to Scheme 2-2. The size and nearly spherical shape of the sulfonated silica powders were maintained after surface modification and after reaction with the analytes, which was confirmed by SEM as shown in Figs. 2-1 and 2-2.



Scheme 2-2. Preparation of metal-cation-modified silica powders.

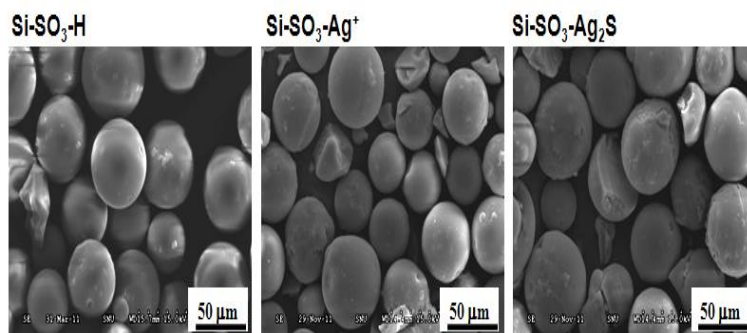


Figure 2-1. SEM images showing the morphology of original sulfonated silica powders (left), sulfonated silica powders modified with silvercation (middle), and sulfonated silica powders after formation of Ag₂S band (right).

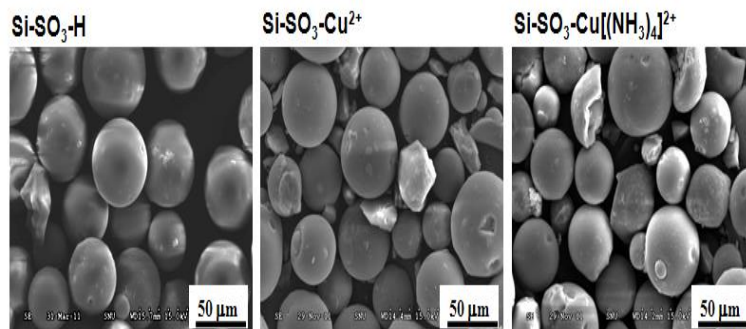


Figure 2-2. SEM images showing the morphology of original sulfonated silica powders (left), sulfonated silica powders modified with copper cation (middle), and sulfonated silica powders after formation of $[\text{Cu}(\text{NH}_3)_4]^{2+}$ complex band (right).

The color of silver-, and copper-modified silica powders was white, and sky blue, respectively, and turned into black, and royal blue after reacting with H_2S gas and NH_3 gas respectively. The presence of silver, and copper was confirmed by EDX as shown in Fig. 2-3.

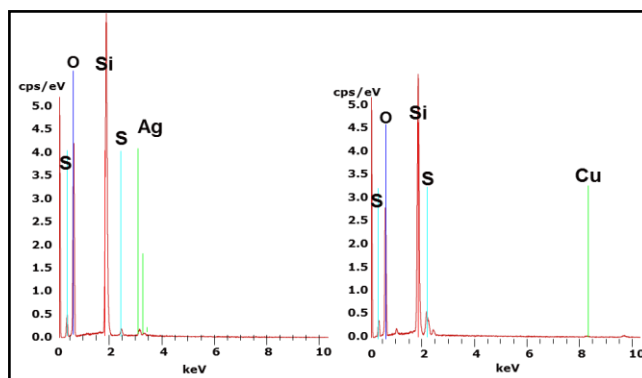


Figure 2-3. EDX spectra showing the presence of silver (left) and copper (right) after surface modification of sulfonated silica powders with metal

cations.

The platinum peak arises from the sputtering process during sample pretreatment before the EDX spectra were taken.

The prepared sensor tube was exposed to the standard samples of toxic gases by connecting to a Standard Mass Flow Controller, and the flow rate was set to 30 mL/min and flow time to 15 or 30 min for H₂S or NH₃, respectively. For the case of H₂S detection with silver-modified silica powders, it was clearly observed that the powder color changed from white to black whenever the contaminated gases contacted the sensing powder and the band width of the colored area was linearly proportional to the concentration of H₂S (Fig.2- 4).

The concentration of H₂S recommended as IDLH (100 ppm) was easily detected by our tube sensor having an inner diameter of 3 mm. It is expected that the detection limit of this tube sensor can be improved by optimizing the size and shape of the tube. This simple and convenient detection of toxic gases clearly demonstrates the usefulness of our strategy to develop *on-site* colorimetric gas sensors based on metal-ion-modified silica powders.

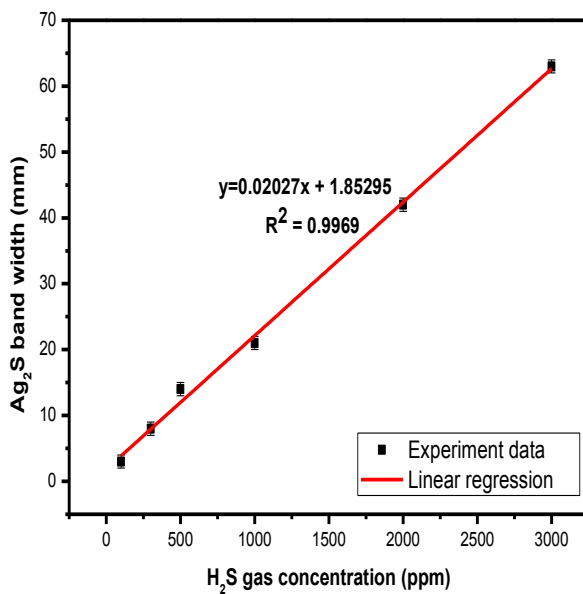
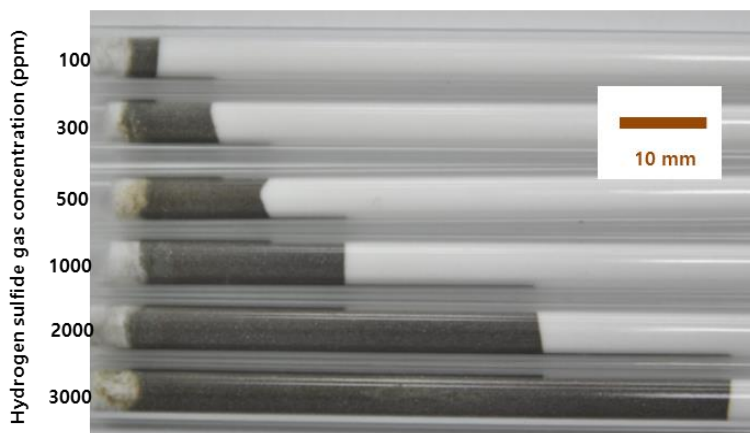


Figure 2-4. Digital images of Ag₂S bands formed after exposing the tube sensors packed with silver-modified silica powder to 450 mL of the contaminated air with various amount of H₂S gas (top). Linear dependency of Ag₂S band width on the H₂S gas concentration (bottom).

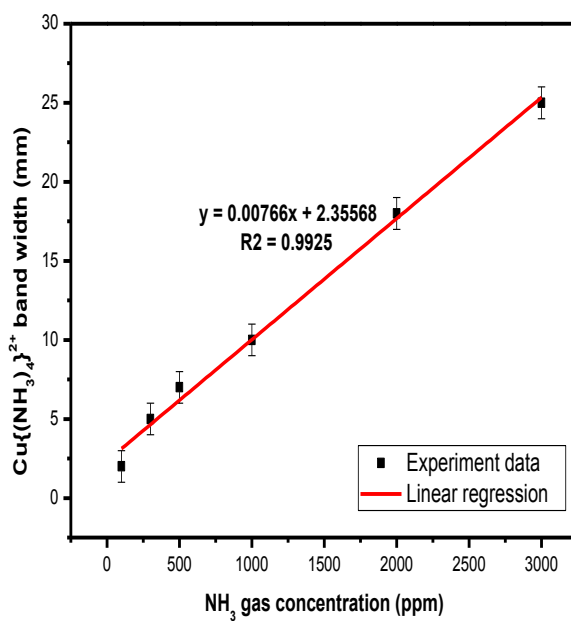
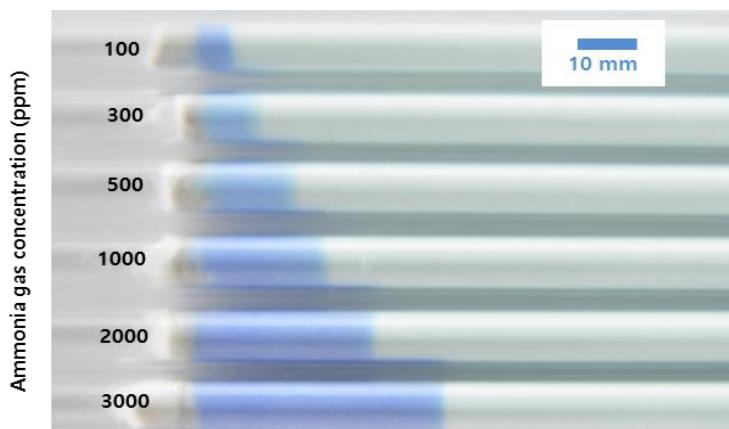


Figure 2-5. Digital images of $[\text{Cu}(\text{NH}_3)_4]^{2+}$ bands formed after exposing the tube sensors packed with copper-modified silica powder to 900 mL of NH_3 gas (top). Linear dependency of $[\text{Cu}(\text{NH}_3)_4]^{2+}$ band width on the NH_3 gas concentration (bottom).

For the case of NH_3 detection with copper-modified silica powders, the color was clearly changed from sky-blue to royal blue whenever the contaminated gases contacted the sensing powder and the band width of the colored area were linearly proportional to the concentration of NH_3 (Fig. 2-5). The concentration of NH_3 recommended as IDLH (300 ppm) was also easily detected by our tube sensor having an inner diameter of 3 mm. It is also expected that the detection limit of this tube sensor can be improved by optimizing the size and shape of the tube. The results for H_2S and NH_3 gases were summarized in Tables 2-1 and 2-2, emphasizing the excellent linear response and simplicity of detection method. The black color of silver sulfide precipitate and royal blue color of copper-ammonia complex remained stable over prolonged time (for several months) without showing any change of color or color intensity, which is advantageous for preserving evidence in official documentation. Therefore, it is expected that workers in chemical industries or forensic science field can determine the concentrations of H_2S or NH_3 gases by naked eyes by observing the color change of the metal-ion-modified silica powders, which would help protecting them from toxic environment.

Our strategy to develop *on-site* gas sensors based on metal-ion-modified silica powders can be extended to various other analytes simply by selecting appropriate metal cations, and related investigations are currently under way.

Table 2-1. Linear Response Range

Analyte	R ²	Linear range, ppm	Flow, (injection)
H ₂ S	0.9969	100 - 3000	30 mL / 15 min
NH ₃	0.9925	100 - 3000	30 mL / 30 min

Table 2-2. Detection Limits and Colorimetric Change

Analyte	Detection limit, ppm	Color	Color
	(sample phase, discriminance)	(before)	(after)
H ₂ S	less than 100 (gas sample, eye)	white	black
NH ₃	less than 100 (gas sample, eye)	sky-blue	royal blue

2.5. Conclusion

We have successfully developed the highly sensitive colorimetric sensor based on metal-ion-modified silica powders, which can display color changes by exposing to toxic species. H₂S and NH₃ gases in air can be easily detected in the range from 100 to 3000 ppm with the new sensor made with glass tubes having an inner diameter of 3 mm. The sensor can display qualitative on/off sensing for the presence of both gases at the HDLH levels (100 ppm for H₂S and 300 ppm for NH₃). This detection range is among the most important in practical applications in diverse industrial and forensic fields. Our strategy to develop *on-site* gas sensors based on metal-ion-modified silica powders can be extended to various other analytes simply by deliberately selecting appropriate metal cations. Our method offers simplicity, reproducible and easily understandable result, high sensitivity (short response time), and selectivity. Most importantly, it is portable and can be directly used for *on-site* and *in-situ* monitoring in various practical applications.

2.6. References

1. T. Zhou, N. Wang, C. H. Li, H. Y. Yuan, D. Xiao, *Anal. Chem.* **2010**, *82*, 1705.
2. A. Christia-Lotter, C. Bartoli, M. D. Piercecchi-Marti, D. Demory, A. L. Pelissier-Alicot, A. Sanvoisin, G. Leonetti, *Forensic. Sci. Int.* **2007**, *169*, 206.
3. A. K. Chaturvedi, D. R. Smith, D. V. Canfield, *Forensic. Sci. Int.* **2001**, *123*, 211.
4. C.-H. Chou, J. Selene, Agency for Toxic Substances and Disease Registry, Syracuse Research Cor. Toxicological Profile For Hydrogen Sulfide, U. S. Department of Health and Human Services, Atlanta, **2006**, p. 21.
5. N. Roney, F. Llados, Agency for Toxic Substances and Disease Registry, Syracuse Research Cor, Toxicological Profile For Ammonia, U. S. Department of Health and Human Services, Atlanta, **2004**, p. 23.
6. Centers for Disease Control and Prevention Home Page. Documentation for Immediately Dangerous To Life or Health Concentrations (IDLHs) for Ammonia. <http://www.cdc.gov/niosh/idlh/7664417.html>. (accessed Jul 1, 2014).
7. Z. Pawlak, A. S. Pawlak, *Talanta* **1999**, *48*, 347.
8. J. M. Davidson, Z. Pikramenou, A. Ponce, R. E. Winpenney, *Anal. Chem.* **2009**, *81*, 3669.
9. X. F. Yang, L. Wang, H. Xu, M. Zhao, *Anal. Chem.* **2009**, *631*, 91.
10. K. Han, W. F. Koch, *Anal. Chem.* **2009**, *59*, 1016.
11. K. Maebashi, K. Iwadate, K. Sakai, A. Takatsu, K. Fukui, M. Aoyagi, E. Ochiai, T. Nagai, *Forensic. Sci. Int.* **2011**, *207*, 91.
12. J. Xu, Q. Pan, Y. Shun, Z. Tian, *Sensor. Actuat. B-Chem.* **2000**, *66*, 277.
13. C. N. Xu, N. Miura, Y. Ishida, K. Matsuda, N. Yamazoe, *Sensor. Actuat. B-Chem.* **2000**, *65*, 163.

14. C. L. Xiang, D. D. Jiang, Y. J. Zou, H. L. Chu, S. J. Qiu, H. Z. Zhang, F. Xu, L. X. Sun, L. J. Zheng, *Ceram. Int.* **2015**, *41*, 6432.
15. L. C. Brousseau, T. E. Mallouk, *Anal. Chem.* **1997**, *69*, 679.
16. H. Bai, Q. Chen, C. Li, C. Lu, G. Shi, *Polymer* **2007**, *48*, 4015.
17. U. V. patil, N. S. Ramgir, N. Karmakar, A. Bhogale, A. K. Debnath, D. K. Aswal, S. K. Gupta, D. C. Kothari, *Appl. Surf. Sci.* **2015**. 339. 69.
18. Y. X. Li, X. B. Zou, X. W. Huang, J. Y. Shi, J. W. Zhao, M. Holmes, L. M. Hao, *Biosens. Bioelectron.* **2015**. 67. 35.
19. S. Park, S. Kim, S. Lee, C. Lee, *B. Korean. Chem. Soc.* **2015**, *36*. 468.
20. Wired Magazine Home Page. In “Dangerous Japanese ‘Detergent Suicide’ Technique Creeps Into U.S”.
http://www.colofirechiefs.org/ffsafety/wired_031309.pdf.
(accessed Jul 1, 2014).
21. Joint Regional Intelligence Home Page. Hazards Posed to First Responders by Hydrogen Sulfide Suicides.
<http://infor.publicintelligence.net/LARTTACHydrogensulfide.pdf>. (accessed Jul 1, 2014).
22. Police Magazine Home Page. Chemical Suicides.
<http://www.policemag.com/channel/patrol/articles/2011/04/duty-dangers-chemical-s-suicides.aspx>. (accessed Jul 1, 2014).
23. S. Chopra, K. Mcguire, N. Gothard, A. M. Rao, A. Pham, *Appl. Phys. Lett.* **2003**, *83*, 2280.
24. S. K. Park, T. Y. Han, J. S. Lee, *B. Korean. Chem. Soc.* **2015**, *36*. 1384.
25. K. H. Kim, H. J. Kim, *B. Korean. Chem. Soc.* **2015**, *36*. 183.

Chapter 3

***On-site* Colorimetric Forensic Sensor (II):**

Quantitative Detection of Toxic S²⁻ Ion in Blood

Plasma using Metal-Ion-Modified Silica Powders

3.1. Abstract

Immensely sensitive, accurate and simple *on-site* colorimetric sensor has been developed for the quantitative detection of the sulfide ion in human blood plasma. The colorimetric sensor consists of lead-ion-modified silica-gel powders placed in a glass tube. The powder color changes upon reaction with sulfide ions in blood plasma. It is capable of easily detecting toxic sulfide ion by using a glass tube with an inner diameter of 3 mm. By employing the type of colorimetric sensor to a blood sample, it is possible to detect the sulfide ion with a concentration limit of 0.1 ppm and excellent reproducibility, thus making it superior to conventional analysis methods that need multiple preparation processes and various sophisticated instruments. Since the sensor reported here is insensitive to environmental conditions such as temperature or humidity, and is featured by simplicity, fast response, high sensitivity, and easily understandable results based on absolute affirmative/negative response, it is expected to be effectively used for *on-site* applications such as detecting poisonous ions in blood samples.

3.2. Introduction

Fatally toxic gas such as hydrogen sulfide (H_2S) is generated by human activities, and in particular, as products or by-products in the chemical industry.¹ H_2S is a colorless and fatally poisonous gas with an unpleasant odor, and it is unavoidably emitted in processes in the manufacturing industry and in relation to waste disposal. H_2S gas is well known as an extremely harmful gas due to its toxicity to human beings and to the environment; in cases of being poisoned by H_2S , S^{2-} ion is present in victim's blood. A S^{2-} concentration higher than 5 ppm in human blood can be lethal and a cause of death.

Several techniques have been developed to determine H_2S concentrations, such as titrimetric,² spectroscopic,³ electro-chemical,⁴ and chromatographic⁵ techniques. The titrimetric method utilizes a simple apparatus but is less sensitive. Spectroscopic and electrochemical techniques require complex chemical compounds for sulfur to react with while chromatographic techniques require expensive equipment and complicated sample pretreatment and preparation processes.

To detect the existence of toxic species in human blood, it is desirable to have access to an analysis method that can rapidly quantify and qualify chemical species. Specially, in consideration of the suicidal wave related with H_2S gas which can easily be produced by mixing certain household materials⁶,⁷ it is necessary to protect first responders, such as emergency service workers or family members, from the risk of death by inhaling lethal quantities of the gas or by fire.⁸ Under such circumstances, a direct analysis method is indispensable because it is difficult to preserve evidence at the scene, even if the space is confined.

Ideally, such a sensor should be able to bond to directly toxic species by strong and selective chemical interactions, and make qualitative and

quantitative analyses possible through simple and straightforward color changes.

We have developed to emphasize the simplicity and convenience of the newly developed colorimetric method based on lead-ion-modified silica powders, which change color upon exposure to toxic species. This sensor consists of lead-cation-bound silica powders placed in a glass tube. The color of the powders changes if a precipitation reaction occurs in the presence of S^{2-} ions in blood plasma. Also, silver-cation-bound silica powders could react to sulfide ion; the same as lead-cation-bound silica powders, but in case of blood sample or aqueous sample instead gas or air, lead-cation-bound silica show the exact linear response range in our system. The simple preparation method of the sensor eliminates time-consuming sample preparation and pretreatment processes, the need for special reaction conditions, and expensive complicated laboratory apparatuses. Because the sensor is not affected by environmental conditions such as the temperature or humidity, and given that it offers simplicity, a fast response, high sensitivity and portability, it can be directly used in many on-site or in-situ applications.

3.3. Experimental Section

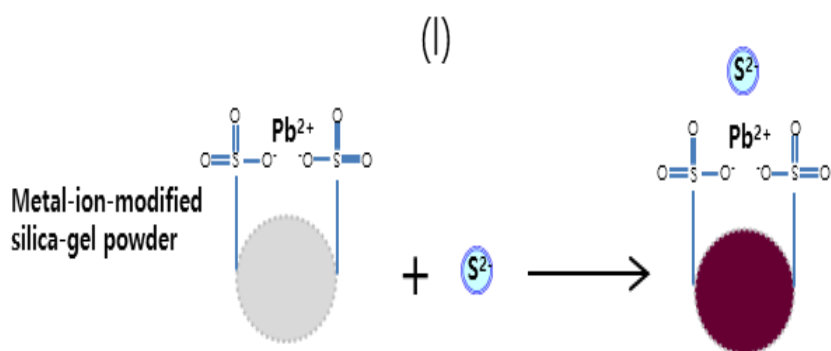
Reagents and chemicals. Lead nitrate ($\text{Pb}(\text{NO}_3)_2$, 99%) was purchased from Sigma Aldrich. Silica gel 60 for column chromatography (SiO_2 , 0.063-0.2 mm) and sulfonated silica gel for column chromatography ($\text{SiO}_2\text{-SO}_3\text{H}$, 45-70 μm) were obtained from Merck Chemicals and Fuji Silysia Chemical Ltd., respectively. All reagents and chemicals were used as-received without further purification.

Preparation of lead-modified silica powders. Appropriate lead nitrate (10 mmol) was dissolved in 50 mL of deionized water in a 100 mL one-neck round bottle flask. After the lead nitrate was completely dissolved, 6.0 g of sulfonated silica gel was added and the mixture was stirred at room temperature for 3 h. The solid was then washed and purified with deionized water three times by using centrifugation at low rpm (2,000 rpm, 10 min) to remove excess free lead cations. Dried lead-modified sulfonated silica powders were obtained by vacuum drying at 60 °C for 3 h, and the solids were then stored in a glass vial for further use. To prepare the sensor for appropriate blood plasma as analyte the bottom side of each glass column with an inner diameter of 3 mm and a length of ~100 mm was clogged with cotton wool, and loaded sequentially with silica gel 60, lead-ion-modified silica powder, and silica gel 60 again to make the sandwich type packing. The top side was clogged with cotton wool to complete the set-up of the sensor columns.

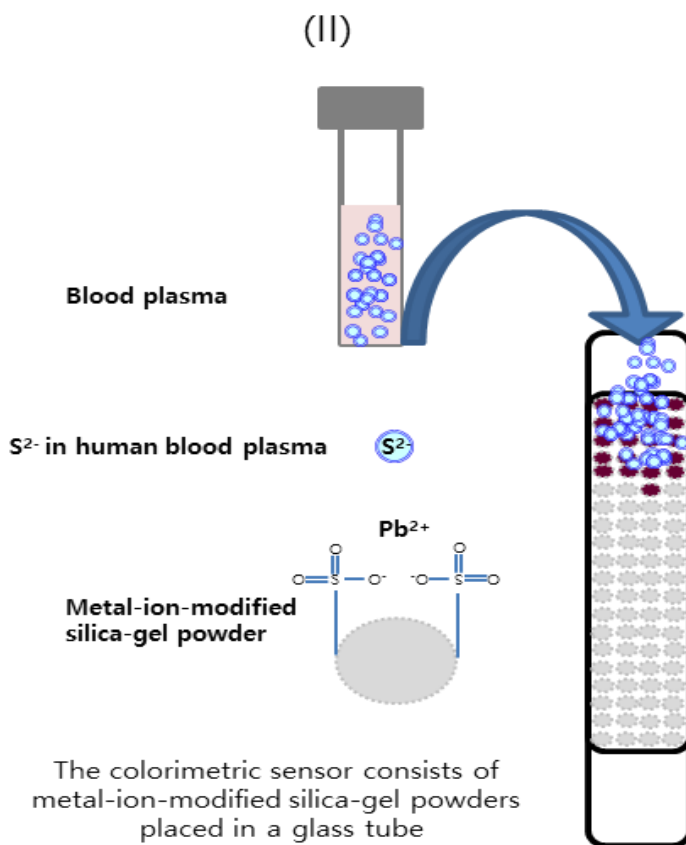
Detection of S^{2-} ion in human blood plasma. A matrix solution was prepared by diluting blood plasma with de-ionized water (volume ratio of blood plasma to deionized water was 1:16). A stock solution containing 100 ppm S^{2-} ion was prepared by dissolving 30 mg $\text{Na}_2\text{S}\cdot 9\text{H}_2\text{O}$ in 40 mL of the matrix solution. Test solutions containing various concentrations of the sulfide ion were prepared by diluting the 100 ppm S^{2-} stock solution with an

appropriate amount of the matrix solution. Each test solution (5 mL) was allowed to flow down through the glass tube (an inner diameter of 3 mm) of Pb-modified silica powders with assistance of nitrogen gas blowing from the top of the column (Scheme 3-1). The flow rate of the nitrogen gas was 30 mL/min. The band widths of the area of black PbS precipitate were measured by experimental scale meter (millimeter unit). All experiments were performed no longer than 30 min after preparation of the test solution in order to minimize the effect of sulfide ion oxidation due to exposure to ambient atmosphere. Also, all experiments were performed three times and the average values were reported with the standard deviation.

Characterization. The size and morphology of the lead-cation-modified silica powders were measured using a scanning electron microscope (SEM, Hitachi S-4300). The presence of lead after surface modification of the sulfonated silica powders was confirmed by energy dispersive X-ray spectrometry (EDX, Carl Zeiss Supra 55VP).



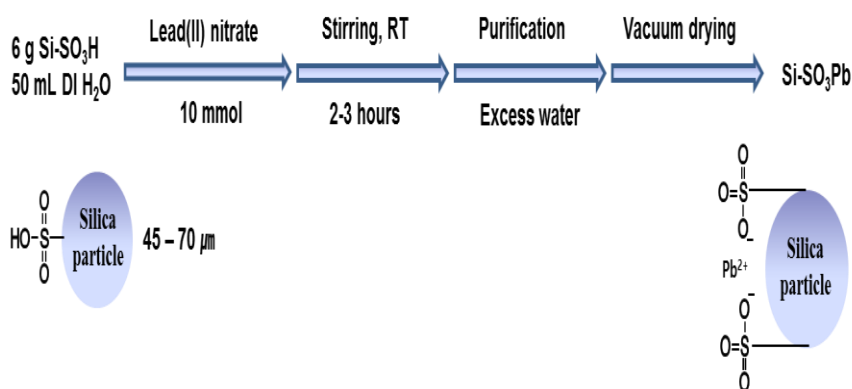
The powder color changes upon reaction with toxic sulfide ion in blood plasma



Scheme 3-1. Experimental settings of the colorimetric sensor for detecting H_2S or NH_3 gases (I) and reaction mechanism of color change between toxic H_2S , NH_3 gases and metal-cation-modified sulfonated silica powders (II).

3.4. Results and Discussion

Sensing material for S^{2-} ion in blood plasma was prepared by surface modification of sulfonated silica powders with lead cations according to Scheme 3-2. Silver-cation-bound silica powders also could react to sulfide ion the same mechanism of lead-cation-bound silica powders, but in case of aqueous sample instead gas, lead-cation-bound silica showed the exact linear response range in our system. The size and nearly spherical shape of the sulfonated silica powder were maintained after surface modification and after reaction with the analyte, which was confirmed by SEM as shown in Fig. 3-1.



Scheme 3-2. Preparation of metal-cation-modified silica powders.

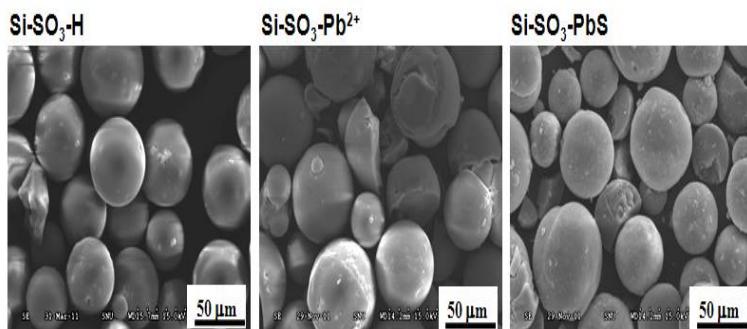


Figure 3-1. SEM images showing the morphology of original sulfonated silica powders (left), sulfonated silica powders modified with lead cation (middle), and sulfonated silica powders after formation of PbS band (right).

The color of lead-modified silica powders was white and turned into black after reacting with S^{2-} ion in blood plasma. The presence of lead was confirmed by EDX as shown in Fig. 3-2. The platinum peak arises from the sputtering process during sample pretreatment before the EDX spectra were taken.

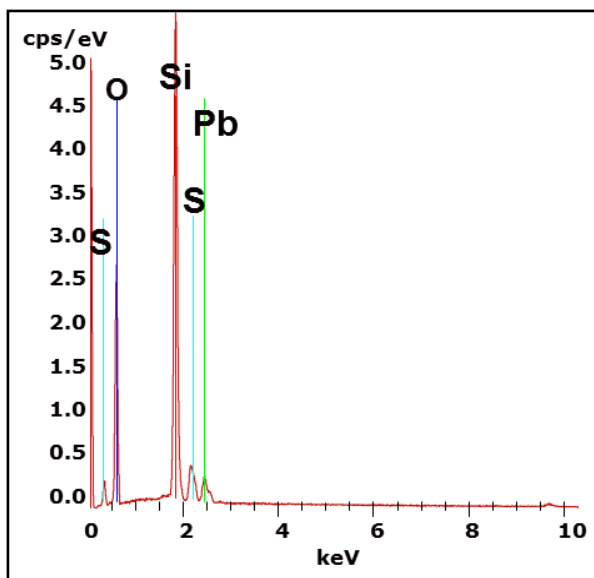
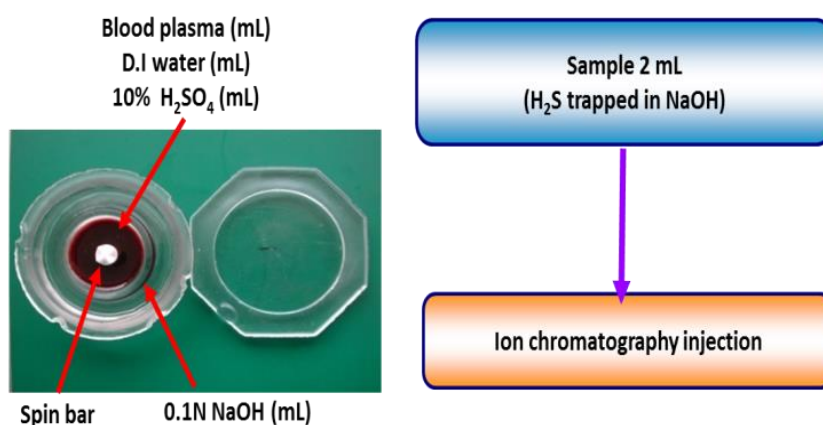


Figure 3-2. EDX spectra showing the presence of lead after surface modification of sulfonated silica powders with metal cation.

National Forensic Service (NFS) agency and forensic analyst has dealt with lots of cases of death due to H_2S poisoning either by accident or by suicide.⁹⁻¹¹ In cases of being poisoned by H_2S , S^{2-} ion is present in victim's blood. A S^{2-} ion concentration higher than 5 ppm in human blood can be lethal and a cause of death.¹²⁻¹³ There are several methods commonly used for detection and determination of S^{2-} ion concentration in human blood, including the Conway micro diffusion method,¹⁴ dialysis membrane filter

method coupled with UV-Vis spectroscopy (methylene blue method), ion chromatography (IC), or gas chromatography/mass spectroscopy (GC/MS), among which the ion chromatography method yields better results. The Conway micro diffusion method coupled with IC has been most widely used in determining sulfide ion concentrations, which employs a special micro diffusion dish, variously termed as the Conway cell, Conway dish, or Conway vessel.¹⁵ This unit consists of a shallow circular glass vessel, 40–70 mm in diameter, containing a central well and with a closely fitting lid sealed with grease; the lid closes the outer annular space but does not touch the wall of the central well. The blood plasma was placed in the inner annulus, and a gas-absorbing reagent (NaOH) was placed in the outer well. Sulfuric acid was added to the blood plasma with the lid closed, and diffusion of the evolved gas (H_2S) to the NaOH solution was allowed to proceed for 3 h. NaOH solution (2 mL) containing trapped H_2S gas was then analyzed using ion chromatography for determination of sulfide ion in the blood plasma sample (Fig. 3-3).



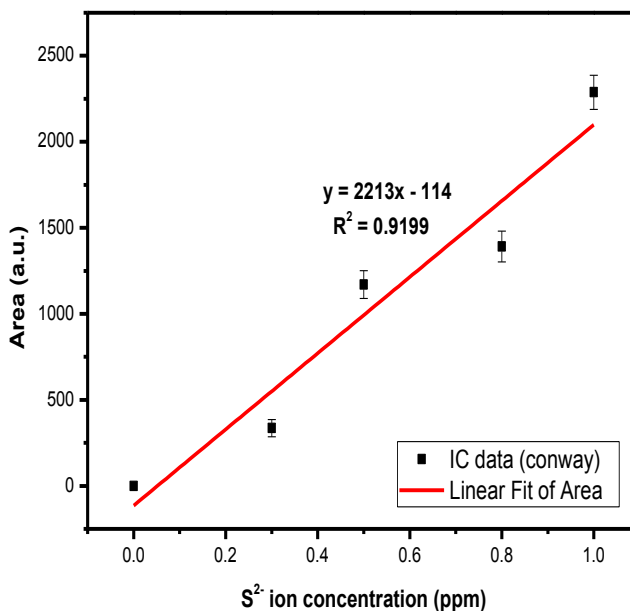


Figure 3-3. Sulfide ion determination in human blood sample by the Conway micro diffusion method and its corresponding correlation coefficient value.

Although sample pre-treatment is easy in this method, the relatively low reproducibility and reliability usually cause problems because the generated H₂S gas undergoes phase changes from liquid (aqueous S²⁻ solution) to gas (H₂S), and finally to liquid (aqueous S²⁻ solution) again by employing the strong acid and base before collection. Another method of S²⁻ ion detection in human blood plasma was conducted through the direct IC method as shown in Fig. 3-4. S²⁻ ion concentration in human blood could be easily determined by this method, but S²⁻ ion may easily volatilize in the form of H₂S within a short period of time from the blood sample during the pretreatment process, which can cause poorly reproducible results. The requirement of complex equipment and time-consuming process add some drawbacks to this method.

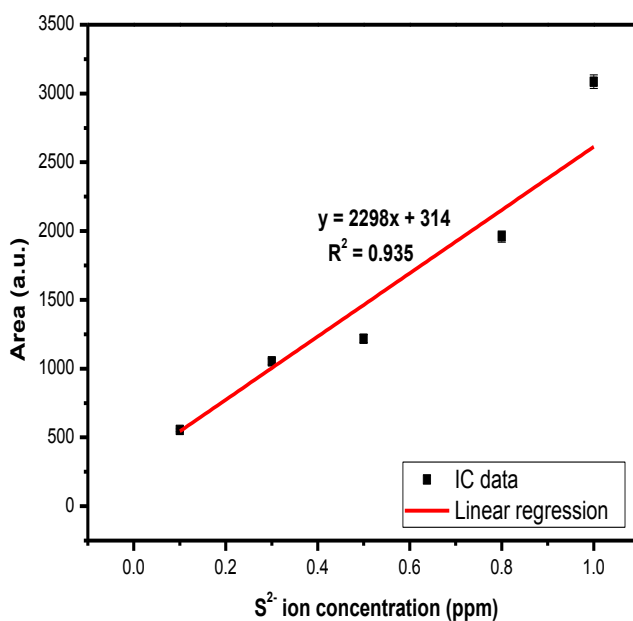
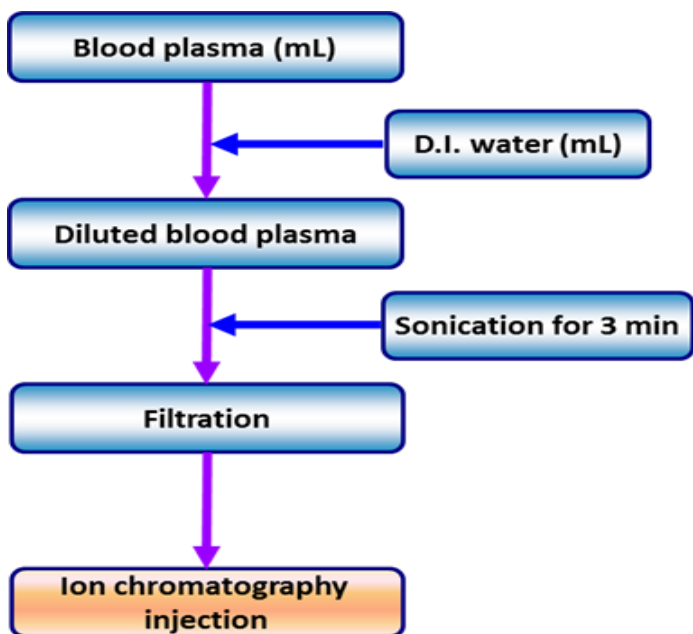


Figure 3-4. Sulfide ion determination in human blood sample by dialysis membrane filter method and its corresponding correlation coefficient value.

To emphasize the simplicity and convenience of the newly developed colorimetric method, the Conway micro diffusion method coupled with IC and the direct IC method after dialysis membrane filtration were also employed and the results were compared (Figs. 3–4). The white lead-modified silica powder turned black upon reaction with sulfide ion indicating the formation of lead sulfide precipitate, which was easily visualized with naked eye (Fig. 3-5).

The new method eliminates the necessity of multiple and tedious sample preparation and pretreatment, special reaction conditions, and expensive complicated laboratory apparatus, and produces comparable (even better) correlation coefficient values to conventional methods. The R^2 values of a linear regression were equal to or above 0.99, indicating an acceptable linear response. A very low detection limit (0.1 ppm) comparable to that of the conventional methods was also obtained (Tables 3-1 and 3-2). The sensor material is insensitive to environmental conditions such as temperature or humidity and offers simplicity, fast response, high sensitivity, and easily understandable results based on absolute affirmative/negative response.

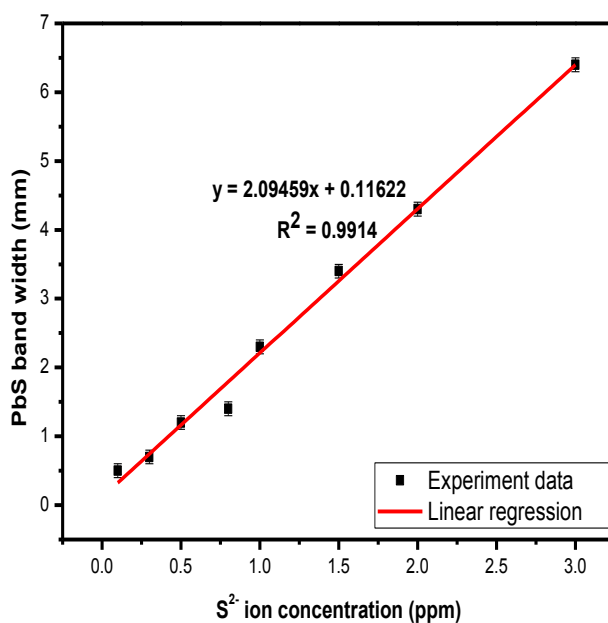
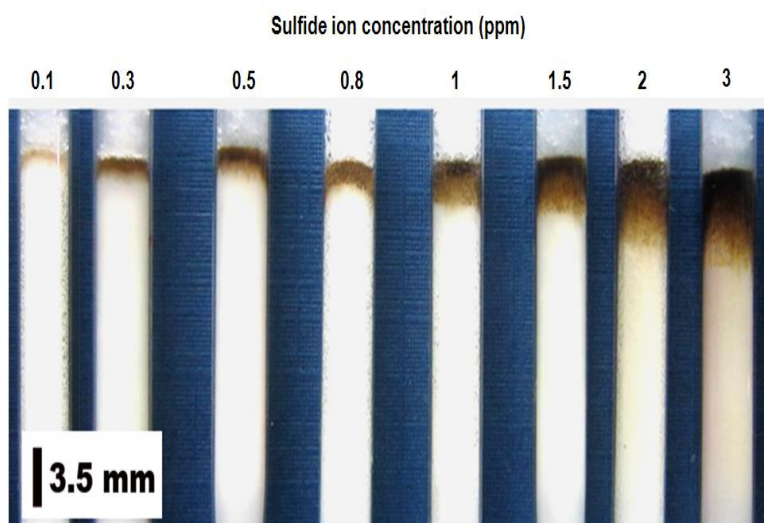


Figure 3-5. Digital images of PbS bands formed after 5 mL of human blood plasma containing various concentration of S^{2-} ion was passed through glass column packed with lead-modified silica powder (top). Linear dependency of PbS band width on the S^{2-} ion concentration in human blood plasma (bottom).

Table 3-1. Linear Response Range

Analyte	R ²	Linear range, ppm	Flow, (injection)
S ²⁻	0.9914	0.1 - 10	5 mL

Table 3-2. Detection Limits and Colorimetric Change

Analyte	Detection limit, ppm (sample phase, discriminance)	Color (before)	Color (after)
S ²⁻	0.1 (blood plasma sample, eye)	white	black

3.5. Conclusion

We have successfully developed the highly sensitive colorimetric method based on lead-ion-modified silica powders, which can display color changes by exposing to toxic sulfide ion in human blood plasma. Also, silver-cation-bound silica powders could react to sulfide ion the same as lead-cation-bound silica powders, but in case of blood sample or aqueous sample instead gas or air, lead-cation-bound silica show the exact linear response range in our system. Moreover, the newly developed sensor is also very effective to detect S^{2-} ions in blood samples in the range of 0.1 ppm (detection limit) to 3 ppm (fatal dose). Our strategy to develop *on-site* colorimetric sensor based on lead-ion-modified silica powders can be extended to various other analytes simply by deliberately selecting appropriate metal cations. Our method offers simplicity, reproducible and easily understandable result, high sensitivity (short response time), and selectivity, while eliminates the requirement of complex and expensive equipment and complicated sample preparations (e.g., micro diffusion, extraction). Most importantly, it is portable and can be directly used for *on-site* and *in-situ* monitoring in various practical applications.

3.6. References

1. T. Zhou, N. Wang, C. H. Li, H. Y. Yuan, D. Xiao, *Anal. Chem.* **2010**, *82*, 1705.
2. Z. Pawlak, A. Pawlak, A. S. *Talanta.* **1999**, *48*, 347.
3. J. M. Davidson, Z. Pikramenou, A. Ponce, R. E. Winpenny, *Anal. Chem.* **2009**, *81*, 3669.
4. X. F. Yang, L. Wang, H. Xu, M. Zhao, *Anal. Chem.* **2009**, *631*, 91.
5. K. Han, W. F. Koch, *Anal. Chem.* **2009**, *59*, 1016.
6. Wired Magazine Home Page. In “Dangerous Japanese ‘Detergent Suicide’ Technique Creeps Into U.S?”. http://www.colofirechiefs.org/ffsafety/wired_031309.pdf. (accessed Jul 1, 2014).
7. Joint Regional Intelligence Home Page. Hazards Posed to First Responders by Hydrogen Sulfide Suicides. <http://infor.publicintelligence.net/LARTTACHydrogensulfide.pdf>. (accessed Jul 1, 2014).
8. Police Magazine Home Page. Chemical Suicides. <http://www.policemag.com/channel/patrol/articles/2011/04/duty-dangers-chemical-suicides.aspx>. (accessed Jul 1, 2014).
9. K. Kimura, M. Hasegawa, K. Matsubara, C. Maseda, M. Kagawa, S. Takahashi, K. I. Tanabe, *Forensic. Sci. Int.* **1994**, *66*, 111.

10. A. Christia-Lotter, C. Bartoli, M. D. Piercecchi-Marti, D. Demory, A. L. Pelissier-Alicot, A. Sanvoisin, G. Leonetti, *Forensic. Sci. Int.* **2007**, *169*, 206.
11. W. Steiling, M. Bascompta, P. Carthew, G. Catalano, N. Corea, A. D'Haese, P. Jackson, L. Kromidas, P. Meurice, H. Rothe, M. Singal, *Toxicol. Lett.* **2014**, *227*, 41.
12. W. Puacz, W. Szahum, K. Linke, *Analyst* **1995**, *120*, 939.
13. K. Maebashi, K. Iwadate, K. Sakai, A. Takatsu, K. Fukui, M. Aoyagi, E. Ochiai, T. Nagai, *Forensic. Sci. Int.* **2011**, *207*, 91.
14. A. K. Chaturvedi, D. R. Smith, D. V. Canfield, *Forensic. Sci. Int.* **2001**, *123*, 211.
15. E. O'malley, E. J. Conway, O. Fitzgerald, *Biochem. J.* **1943**, *37*, 278.

Chapter 4

**Photoluminescent europium(III) complex
intercalated in natural and synthetic clay minerals
for enhanced latent fingerprint detection**

4.1. Abstract

Fluorescent nanohybrid materials, europium(III) complex intercalated Na⁺-smectite clay minerals (synthetic hectorite and natural montmorillonite), have been developed to visualize latent fingerprints. The guest europium(III) complex ([EuCl₂(Phen)₂(H₂O)₂]Cl·H₂O) was obtained by simple complex reaction between europium chloride hexahydrate (EuCl₃·6H₂O) and 1,10-phenanthroline (Phen) as a 1:2 molar ratio of Eu³⁺ ion to ligand molecules. The intercalated nanohybrids ([Eu(Phen)₂]³⁺-clay minerals) were obtained through ion exchange reaction of interlayer sodium cation with europium complex ion. Guest europium(III) complex and [Eu(Phen)₂]³⁺-clay mineral hybrids were characterized by powder X-ray diffraction, Fourier transform infrared, thermal analysis (TG-DTA), elemental analysis, UV-visible and fluorescence spectroscopy. The intercalated complex maintains a characteristic red ⁵D₀-⁷F₂ emission at wavelength 617 nm, which is comparable to the free complex. The ⁵D₀-⁷F₂ emission intensity of [Eu(Phen)₂]³⁺-hectorite was *ca.* 3.5 times higher than that of [Eu(Phen)₂]³⁺-montmorillonite, due to the presence of quenching impurities in natural montmorillonite itself. Fingerprint residues on glass slides were harvested by using [Eu(Phen)₂]³⁺-clay mineral powders, resulting in good definition for enhanced latent fingerprint detection. Particularly, [Eu(Phen)₂]³⁺-hectorite hybrid powder was more clearly separated from the background compared to the montmorillonite hybrid powder.

4.2. Introduction

Recently, various nanohybrid materials have attracted considerable research interest due to their unusual and synergetic physicochemical properties, which cannot be achieved by any single component (Cerveau *et al.*, 2001; Choy *et al.*, 2002a; Zhang *et al.*, 2009). Various physico-chemical processes have been applied for the production of such materials. Among them, the intercalation reaction - which is the reversible insertion of guest species into two-dimensional host materials - is expected to be one of the most effective ways of preparing noble materials with the desired functionality (Khan and O'Hare, 2002; Letaief and Detellier 2007; Jung *et al.*, 2008a). In this regard, clay minerals, in particular, have attracted a great deal of attention, because they can keep various cationic species within their interlayer space, regardless of whether they are inorganic or organic ions or even polymeric ions (Choy *et al.*, 2002b; Jung *et al.*, 2008b; Zhu *et al.*, 2009). Therefore, numerous studies have been directed towards the intercalation chemistry of clay minerals.

Compounds containing lanthanide ions, such as Eu(III), have attracted significant interest in the fields of optical display devices and medical applications (Kido and Okamoto, 2002; Bünzli and Piguet, 2005; Eliseeva and Bünzli, 2010), due to their excellent photoluminescence property based on the $4f-4f$ electron transition of Eu(III). Trivalent europium ion shows five narrow emission lines, corresponding to a series of ${}^5D_0-{}^7F_J$ transitions ($J = 0, 1, 2, 3$ and 4), and the strongest emission can be assigned to the transition ${}^5D_0-{}^7F_2$ appearing around 615 nm (emits red light) (Jin *et al.*, 1997). Generally, europium ion itself exhibits rather weak photoluminescence either in solution or in a solid state, because of its weak light absorption. However, the problem of weak light absorption can be overcome by the so-called 'antenna effect' (or

sensitization) (Binnemans, 2009; Cui *et al.*, 2012). When complexed with heterocyclic ligands, such as 1,10-phenanthroline or 2,2'-bipyridine, these chelated complexes exhibit strong fluorescence emission with a long intensity decay lifetime, due to the intramolecular energy transfer from the ligand to the metal ion (Jin *et al.*, 1997). Although they exhibit enhanced photoluminescence, pure europium complexes show poor thermal and mechanical stabilities and poor processing ability. Moreover, these complexes suffer from luminescence quenching in humid conditions. To prevent emission quenching by vibration of coordinated H₂O molecules, and to improve the processing ability of the complexes, the europium complexes are introduced in various matrixes, such as polymer, aluminosilicate, and micro- or mesoporous materials, to form nanohybrids (Kráčalík *et al.*, 2007; Sánchez *et al.*, 2006; Peng *et al.*, 2005).

Among a variety of matrix materials, smectite clay minerals are regarded as having great potential in this respect (Hagerman *et al.*, 2003; Okada *et al.*, 2007). The interlayer space of smectite clay minerals could be an effective stabilizer for the lanthanide species, due to their high retention capacity. The complex molecules, introduced by electrostatic forces between the inorganic layers, can be protected thermally, chemically and mechanically from the external environment. Most of all, the luminescence property of europium complexes, when intercalated into the clay minerals, can be maintained, while simultaneously providing stability of the complex against reaction with moisture. Therefore, such a hybrid system is a promising approach to develop improved luminescent materials. In this regard, luminescent hybrid materials based on natural clay minerals have been extensively studied (Gao *et al.*, 2011; Khaorapapong *et al.*, 2010). Specially, Celedon *et al.* (2009) reported that lanthanide complexes were intercalated into Na⁺-montmorillonite for

protection against hydrolysis. However, lattice of natural clay minerals contains significant amounts of iron ion, a factor which interrupt the luminescence. The present paper deals with not only natural montmorillonite but also synthetic hectorite, which is structurally related to montmorillonite but contains few or no iron ion content. In addition, their use in latent fingerprint detection by comparison between natural and synthetic clay mineral nanohybrids has rarely been attempted.

In the present study, we describe the synthesis, characterization, and luminescence properties of europium(III)-clay mineral nanohybrids, along with the results of a preliminary test of their latent fingerprint detection. Two types of clay minerals (Laponite-XLG, synthetic hectorite-type and Kunipia-F, natural montmorillonite-type) were used as the host clay minerals. The guest europium complex, $[\text{EuCl}_2(\text{Phen})_2(\text{H}_2\text{O})_2]\text{Cl}\cdot\text{H}_2\text{O}$, was obtained by simple complex reaction between europium chloride hexahydrate ($\text{EuCl}_3\cdot 6\text{H}_2\text{O}$) and 1, 10-phenanthroline (Phen).

4.3. Experimental Section

4.3.1 Materials.

$\text{EuCl}_3 \cdot 6\text{H}_2\text{O}$ (99.99%) and 1, 10-phenanthroline ($\geq 99\%$) were purchased from Sigma Aldrich. Two clay minerals, Na^+ -montmorillonite and Na^+ -hectorite, were used as host materials. Na^+ -montmorillonite (Kunipia F, Kunimine Corp.) was used with the chemical formula of $\text{Na}_{0.35}\text{K}_{0.01}\text{Ca}_{0.02}(\text{Si}_{3.88}\text{Al}_{0.12})(\text{Al}_{1.53}\text{Mg}_{0.32}\text{Fe}_{0.10})\text{O}_{10}(\text{OH})_2 \cdot n\text{H}_2\text{O}$ and a cation exchange capacity (CEC) is 100 mequiv/100 g. The specific surface area was $6 \text{ m}^2/\text{g}$. The dimensions of montmorillonite are *ca.* $1 \text{ nm} \times 1.5 \text{ }\mu\text{m}$, with a negative charge density is $0.022 \text{ e}^-/\text{\AA}^2$. Na^+ -hectorite (Laponite XLG, Rockwood Ltd.), synthetic clay mineral, has the chemical formula of $\text{Na}_{0.3}(\text{Si}_4)(\text{Mg}_{2.7}\text{Li}_{0.3})\text{O}_{10}(\text{OH})_2 \cdot n\text{H}_2\text{O}$ and a CEC is 63 mequiv/100g. The specific surface area was $370 \text{ m}^2/\text{g}$. The dimensions of hectorite are *ca.* $1 \text{ nm} \times 25 \text{ nm}$, with a negative charge density is $0.014 \text{ e}^-/\text{\AA}^2$. All other reagents were of analytical grade.

4.3.2 Synthesis of Europium(III) Complex.

The precursor Eu(III) complex were prepared by modification of previously reported procedures (Jin *et al.*, 1997; Bansal *et al.*, 1969). $\text{EuCl}_3 \cdot 6\text{H}_2\text{O}$ (2.7224 g, 7.43 mmol) and 1, 10-phenanthroline (2.6779 g, 14.86 mmol) were dissolved in each absolute ethanol (20 mL) solution. The two ethanoic solutions were mixed, and then stirred for 3 h until a white compound was precipitated. The precipitate was filtered using a PTFE filter (pore size $1.0 \text{ }\mu\text{m}$) and was dried at room temperature. Finally, the obtained product was dissolved in water and recrystallized by evaporation.

$[\text{EuCl}_2(\text{Phen})_2(\text{H}_2\text{O})_2]\text{Cl} \cdot \text{H}_2\text{O}$ (672.77): *calcd.* Eu 22.59, C 42.85, H 3.30, N 8.32; *found* Eu 22.67, C 42.83, H 3.08, N 8.39.

4.3.3 Preparation of [Eu(Phen)₂]³⁺-clay mineral hybrids.

1 g of host clay mineral (Na⁺-montmorillonite or Na⁺-hectorite) was pre-swelled in water (75 mL) for one day. The resultant clay mineral dispersion was mixed with Eu(III) complex aqueous solution (corresponding to 1.2-fold the CEC of each clay mineral) under vigorous stirring for 24 h at room temperature. After the ion exchange reaction, the product was separated by centrifugation, and then washed with deionized water several times to remove the excess Eu(III) complex. The intercalation compound was dried in a vacuum oven at 80 °C for 12 h.

4.3.4 Latent fingerprint detection test.

To test [Eu(Phen)₂]³⁺-clay mineral hybrids as a detection agent, fingerprints were deposited onto clean non-porous glass microscope slides. Index finger prints were applied to the glass surface by a middle age male donor. [Eu(Phen)₂]³⁺-clay mineral powders brushed on the latent fingerprints using a commercial make-up brush. The resulting fingerprints were observed by monitoring with UV light at 312 nm, using a Video spectral comparator 6000 (Foster + Freeman Ltd, UK).

4.3.5 Sample characterizations.

X-ray diffraction (XRD) patterns were obtained using a diffractometer (Bruker D8 advance) with graphite-monochromatized and Ni-filtered Cu K α radiation ($\lambda = 1.5418 \text{ \AA}$). The XRD patterns were recorded at an operating voltage of 40 kV and a current of 30 mA. The chemical compositions were determined by performing elemental analysis (CHN : Thermo Electron-FLASH EA1112 and ICP : ICP-OES, Perkin Elmer Optima 8300). Thermogravimetry-differential thermal analysis (TG-DTA) was carried out to

check the thermal behavior of the guest Eu(III)-complex and intercalated clay mineral nanohybrids under air, where the heating rate was fixed at 10 °C/min in the temperature range of 30 °C to 800 °C. Fourier transform infrared spectra (FT-IR) were obtained in the range of 4000 ~ 400 cm⁻¹ with a Varian FTS 800 FT-IR spectrometer by the standard KBr disk method. Diffuse reflectance UV-vis spectra for solid samples were collected using a V-550 Solid UV/Vis Spectrometer (JASCO) equipped with an integrating sphere using BaSO₄ as a standard. The UV-vis spectra obtained in diffuse reflectance mode [R_{∞}] were transformed to a magnitude proportional to the extinction coefficient (κ) through the Kubelka-Munk function [$F(R_{\infty})$] (Kortüm *et al.*, 1963).

$$F(R_{\infty}) = (1 - R_{\infty})^2/2R_{\infty}$$

The excitation and emission spectra were recorded with a Cary Eclipse fluorescence spectrophotometer (Varian) using a xenon lamp as the light source, and the signal was detected using a photomultiplier. All emission spectra were recorded on the corresponding maximum peak positions with a slit width of 10 nm for both the excitation and emission at room temperature. Absolute quantum efficiency for all powder samples was measured at room temperature using absolute quantum efficiency measurement system (Otsuka Electronics, QE-1000) equipped with integrating hemisphere using BaSO₄ as a reference material. A 150 W Xe lamp was used as the source light. Here the quantum efficiency (QE) was used to describe the internal quantum efficiency (IQE), which is defined as the ratio between the number of emitted photon and the number of absorbed photon.

4.4. Results and Discussion

4.4.1. Powder X-ray diffraction analysis

Figure 4-1 shows the powder XRD patterns of the Na⁺-host clay minerals, [Eu(Phen)₂]³⁺-clay mineral hybrids, and Eu(III) complex itself. All diffraction patterns of the obtained Eu(III) complex (Figure 4-1a) were matched with patterns of [EuCl₂(Phen)₂(H₂O)₂]Cl·H₂O which has been previously detailed in literature (space group *Pca*2₁ / *a* = 36.1931 Å, *b* = 7.6074 Å, *c* = 18.0844 Å / *V* = 4979.28 Å³ / *Z* = 8) (Puntus *et al.*, 2008). From the analysis of diffraction patterns, we can estimate molecular dimensions of Eu(III) complex as *a* = 9.0483 Å, *b* = 7.6074 Å and *c* = 9.0422 Å. The Na⁺-hectorite exhibited a broad *001* diffraction pattern (Figure 1b) indicating low crystallinity and small particle size. The Na⁺-montmorillonite indicates well developed *00l* diffraction patterns (Figure 4-1d) due to the relatively larger particle size and higher crystallinity than hectorite. Upon intercalation, the basal spacing significantly expanded from approximately 13.6 to 16.3 Å (Figure 4-1c) and 12.1 to 18.0 Å (Figure 4-1e), suggesting the replacement of interlayer sodium cation by [Eu(Phen)₂]³⁺. Subtracting the silicate layer thickness (hectorite: 9.2 Å, and montmorillonite: 9.6 Å) (Jung *et al.*, 2008a; Bouwe *et al.*, 2011) from the basal spacing of the [Eu(Phen)₂]³⁺-clay mineral hybrids, the interlayer space were estimated to be 7.1 Å and 8.4 Å, respectively. Interestingly, the interlayer space of each hybrid were similar to the lateral molecular length of Eu(III) complex (7.6074 Å), and much smaller than its longitudinal length (9.0483 Å). These results suggested that intercalated Eu(III) complex forms a monolayer, with its longitudinal axis parallel to the layer of clay minerals.

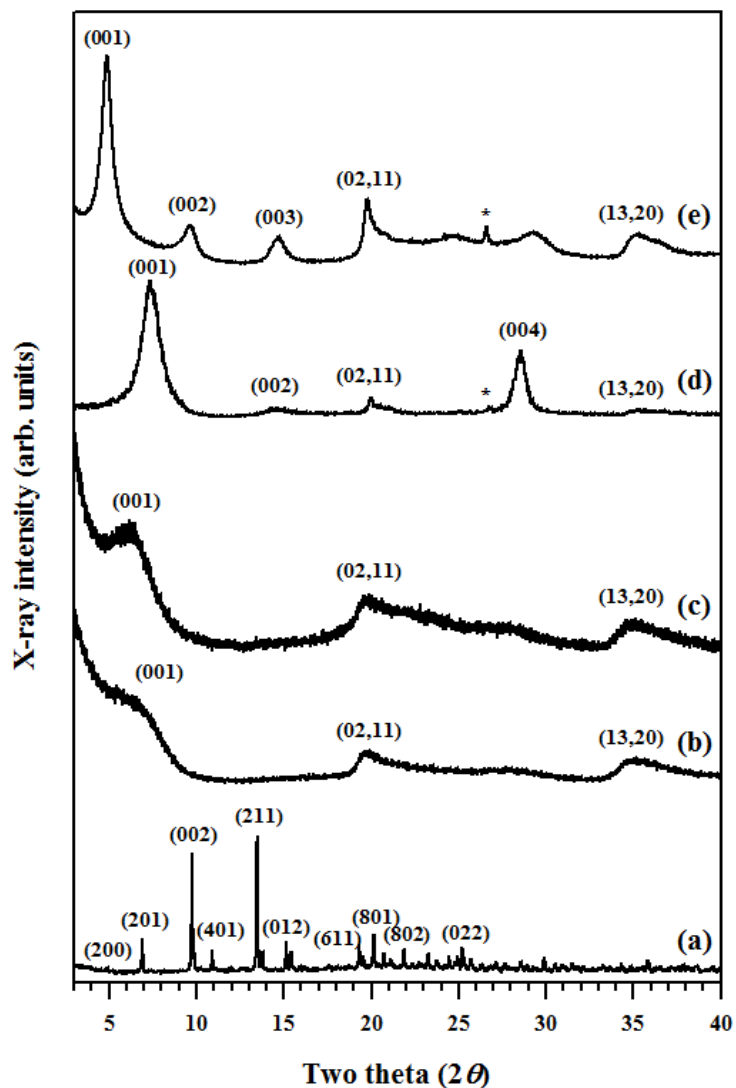


Figure 4-1. X-ray diffraction patterns of (a) Eu(III) complex $[\text{EuCl}_2(\text{Phen})_2(\text{H}_2\text{O})_2]\text{Cl}\cdot\text{H}_2\text{O}$, (b) pristine Na^+ -hectorite, (c) $[\text{Eu}(\text{Phen})_2]^{3+}$ -hectorite hybrid, (d) pristine Na^+ -montmorillonite and (e) $[\text{Eu}(\text{Phen})_2]^{3+}$ -montmorillonite hybrid (* : quartz).

To propose a more reasonable interlayer structure, we considered the distribution of guest ions in the interlayer space of the clay minerals by the location of the negative charge in the layers. Steric limitation is usually generated by the equivalent area (A_e) of clay mineral lattices and the area demand (A_c) of the intercalated molecules. The equivalent area (A_e) available for a monolayer monovalent cation in the interlayer space can be estimated from the equation $A_e = ab/2\xi$, where a and b are lattice parameters of clay mineral and ξ is the layer charge (Jung *et al.*, 2008a). The hectorite and montmorillonite exhibited the equivalent areas of about 60.24 \AA^2 and 38.33 \AA^2 per unit charge, while the area demand of Eu(III) complex (A_c) was 81.817 \AA^2 because the estimated molecular dimensions of Eu(III) complex from XRD analysis were $9.0483 \text{ \AA} \times 7.6074 \text{ \AA} \times 9.0422 \text{ \AA}$. To optimize electrostatic interaction between clay mineral host and Europium complex, three times larger areas of A_e are needed for each Eu(III) complex. A good agreement of these calculations with both the observed stoichiometry of the Eu(III) complex intercalated species and the basal spacing of the obtained nanohybrids (Table 4-1) is observed in the schematic representation (Figure 4-2b) of this geometrical consideration. This agreement goes along with the molecular crystal structure of $[\text{EuCl}_2(\text{Phen})_2(\text{H}_2\text{O})_2]\text{Cl}\cdot\text{H}_2\text{O}$, as shown in Figure 4-2a.

From such an analysis it should be noted that the monolayer structure was highly probable for $[\text{Eu}(\text{Phen})_2]^{3+}$ complex ions in the interlayer space, which could explain a similar interlayer space of the lateral dimension of Eu(III) complex. In addition, Eu(III) complex, when intercalated, was homogeneously distributed at the molecular level in the interlayer space of clay minerals, without forming large particles with a crystalline structure. As

shown in Figure 4-1a, the characteristic orthorhombic ($Pca2_1$) crystalline peaks of $[EuCl_2(Phen)_2(H_2O)_2]Cl \cdot H_2O$ disappeared in the nanohybrids.

4.4.2. Thermal analysis

The TG–DTA curves of guest Eu(III) complex, hectorite and montmorillonite hybrids are shown in Figure 4-3. For Eu(III) complex, the first weight loss (7.3%), which is accompanied with a endothermic response up to 134 °C, can be assigned to the dehydration of inner and outer coordinated water. The second weak endothermic weight loss (27.7%) occurred between 290 °C and 407 °C, and was attributed to the elimination of coordinated phenanthroline molecules. Above 400 °C, the following intense exothermic peak with the large weight loss (33.3%) corresponds to the oxidative decomposition of the phenanthroline ligand. At temperature above 540 °C, the Eu(III) complex was completely decomposed to $EuClO$ (Jin *et al.*, 1997; Bansal *et al.*, 1969). On the other hand, the TG–DTA curves of $[Eu(Phen)_2]^{3+}$ -clay mineral hybrids show the thermal evolution with three consecutive stages due to the dehydration, decomposition, and dehydroxylation. The first weight losses (*ca.* 2.5% and 2.6%) by dehydration were smaller than that of the pure Na^+ -hectorite (*ca.* 15.8%) and Na^+ -montmorillonite (*ca.* 11.4%) (Jung *et al.*, 2008a), because of the presence of an intercalated hydrophobic Eu(III) complex. The second ones were associated with an exothermic reaction in the range of 240 to 650 °C and 230 to 700 °C, which resulted from the oxidative decomposition of intercalated $[Eu(Phen)_2]^{3+}$ complex ions (*ca.* 13.5% and 23.1%). The contents of Eu(III) complex in the hectorite and montmorillonite hybrids, as measured by elemental analysis, were 11.32 ± 0.01 and 18.80 ± 0.01 wt.%, which is in agreement with the estimation by thermal analysis within the error range. The

decomposition of $[\text{Eu}(\text{Phen})_2]^{3+}$ complex ions when confined in the interlayer space of hectorite clay mineral takes place at a higher temperature (at 528 °C) than that of the free complex, which shows maximum exothermic peak at 488 °C. A similar observation was made in the case of the montmorillonite hybrid system (at 528 °C). In general, the intercalated compound exhibits increasing thermal stability compare with its origin organic compounds. In this research, our hybrid compounds are also in agreement with general intercalated compound advantages. That is, the confinement of the organic molecules intercalated between the inorganic layers can contribute to enhanced thermal stability of the Eu(III) complex.

Table 4-1. XRD analysis results and chemical formulas for Eu(III) complex and $[\text{Eu}(\text{Phen})_2]^{3+}$ -clay mineral hybrids.

	Interlayer spacing (\AA) ^a	Chemical formula ^b
Eu(III) complex	-	$[\text{EuCl}_2(\text{Phen})_2(\text{H}_2\text{O})_2]\text{Cl}\cdot\text{H}_2\text{O}$
$[\text{Eu}(\text{Phen})_2]^{3+}$ -hectorite hybrid	16.3	$[\text{Eu}(\text{Phen})_2]_{0.14}(\text{Si}_4)(\text{Mg}_{2.7}\text{Li}_{0.3})\text{O}_{10}(\text{OH})_2\cdot 3\text{H}_2\text{O}$
$[\text{Eu}(\text{Phen})_2]^{3+}$ -montmorillonite hybrid	18.0	$[\text{Eu}(\text{Phen})_2]_{0.134}(\text{Si}_{3.88}\text{Al}_{0.12})(\text{Al}_{1.53}\text{Mg}_{0.32}\text{Fe}_{0.10})\text{O}_{10}(\text{OH})_2\cdot 2\text{H}_2\text{O}$

^a Interlayer spacing were calculated from 001 diffraction patterns.

^b Chemical formula were estimated from the ICP and CHN results.

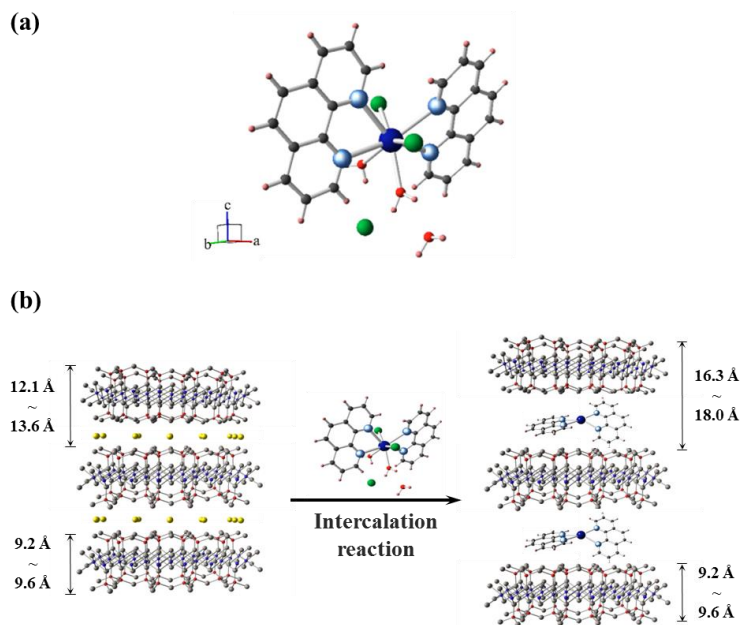


Figure 4-2. Schematic representation of (a) molecular crystal structure of Eu(III) complex and (b) $[\text{Eu}(\text{Phen})_2]^{3+}$ -clay mineral hybrids.

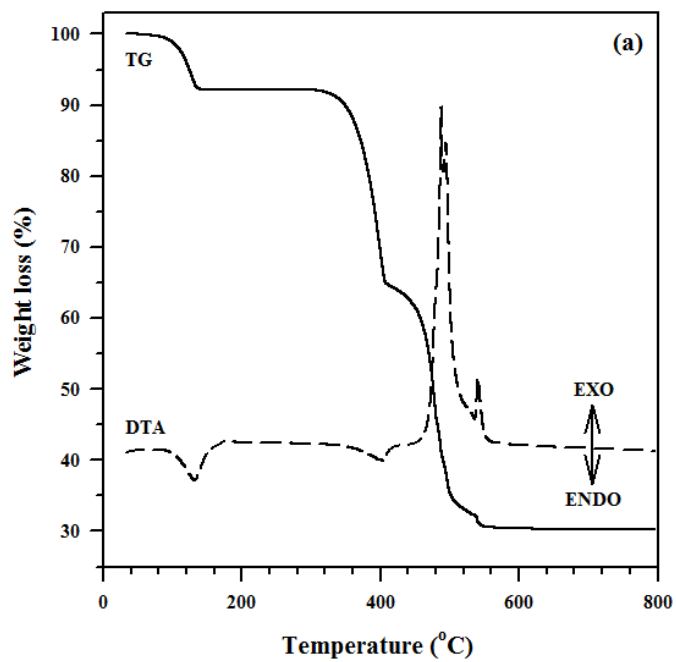


Figure 4-3. TG and DTA curves of (a) Eu(III) complex.

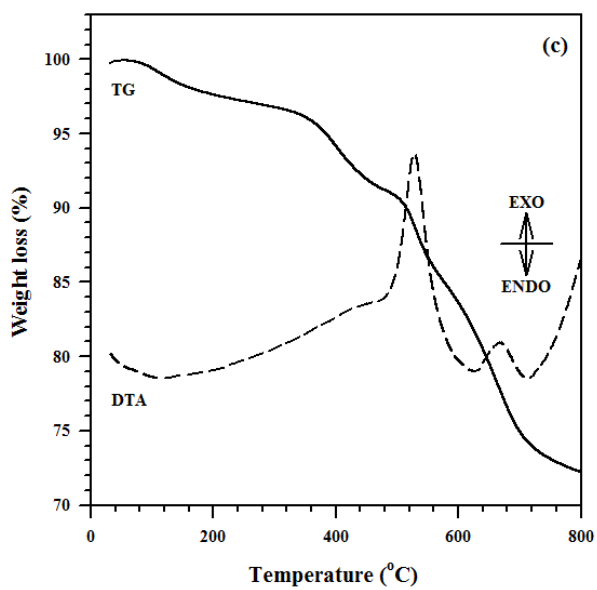
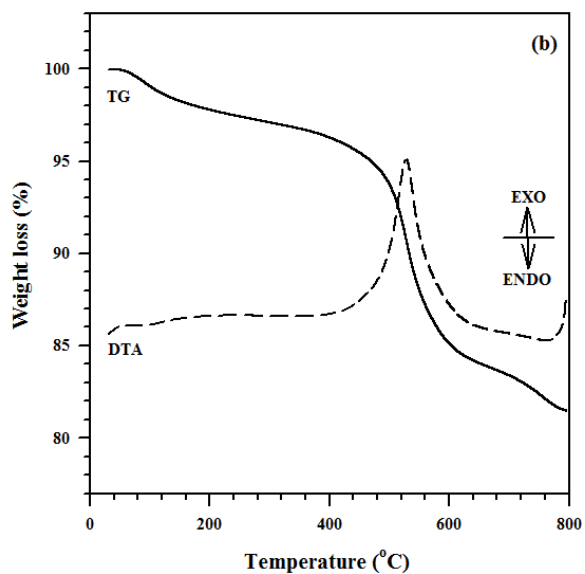


Figure 4-3. TG and DTA curves of (b) $[\text{Eu}(\text{Phen})_2]^{3+}$ -hectorite hybrid and (c) $[\text{Eu}(\text{Phen})_2]^{3+}$ -montmorillonite hybrid.

4.4.3. Fourier transform infrared spectroscopy

FT-IR spectra were examined to provide further evidence for the intercalation of $[\text{Eu}(\text{Phen})_2]^{3+}$ complex ion. Figure 4-4 shows the FT-IR spectra of Eu(III) complex, Na^+ -hectorite, $[\text{Eu}(\text{Phen})_2]^{3+}$ -hectorite hybrid, Na^+ -montmorillonite and $[\text{Eu}(\text{Phen})_2]^{3+}$ -montmorillonite hybrid. The FT-IR spectrum of Eu(III) complex, which are observed in free ligands (Bouwe *et al.*, 2011), is shown in Figure 4a. The bands between 1593 and 1516 cm^{-1} might be assigned to the aromatic skeleton vibration of C=C bonds. Also, a characteristic band at 1423 cm^{-1} was attributed to the stretching vibrations of C=N bonds. Two peaks at 849 and 729 cm^{-1} indicate that the C-H bonds of the aromatic cycle are bended the out of the plane of Phen molecules. For Na^+ -hectorite, the absorption bands at 1013 and 467 cm^{-1} resulted from stretching vibrations of Si-O bonds and Si-O-Si bending vibrations in the clay mineral lattice, respectively. The band at 656 cm^{-1} is ascribed to Mg_3OH bending vibration (Jung *et al.*, 2008a). In case of Na^+ -montmorillonite, the absorption bands at 1043 and 469 cm^{-1} are assigned to a Si-O bond similar to that of hectorite. The typically bands at 914 cm^{-1} and 523 cm^{-1} were due to Al-Al-OH bending vibration in the octahedral layer, and Al-O-Si bending mode, respectively. The absorption near 3626 cm^{-1} is related to hydroxyl stretching vibration of OH units bound to aluminum ions in the clay minerals (Madejová, 2003). Compared with pure Eu(III) complex and hybrids, it should be noted that all the characteristic bands of Eu(III) complex were also detected in the spectra of all the hybrids, which suggests that $[\text{Eu}(\text{Phen})_2]^{3+}$ complex ion is intercalated into the interlayer of the clay mineral, maintaining its functionalities.

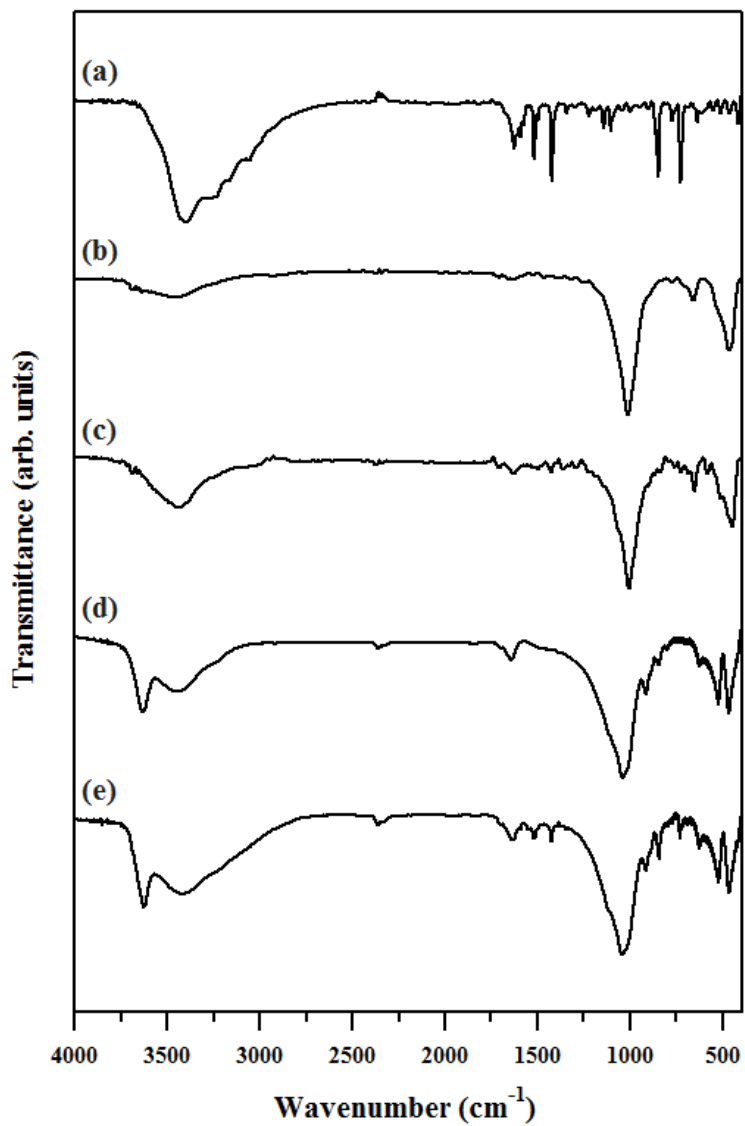


Figure 4-4. Fourier transform infrared spectra of (a) Eu(III) complex, (b) pristine Na⁺-hectorite, (c) [Eu(Phen)₂]³⁺-hectorite hybrid (d) pristine Na⁺-montmorillonite and (e) [Eu(Phen)₂]³⁺-montmorillonite hybrid.

4.4.4. Diffuse reflectance UV-vis spectra

Figure 4-5 shows the diffuse reflectance UV-vis spectra of the guest Eu(III) complex and $[\text{Eu}(\text{Phen})_2]^{3+}$ -clay mineral hybrids in solid state. Eu(III) complex showed a strong and broad band in a wavelength range of 200-390 nm, which is associated with $\pi - \pi^*$ electronic transition caused by phenanthroline ligand. In addition, weaker peaks were observed at 395, 416, 465, 536 and 592 nm, which are due to the intra-configurational forbidden $4f - 4f$ transitions of Eu(III) ions. The $[\text{Eu}(\text{Phen})_2]^{3+}$ -clay mineral hybrids also had a strong and broad band in the UV-vis region, which should be the absorption by ligands of the complex. One of the most notable features is a small but significant *ca.* 14.5 (in case hectorite) or 16 nm (in case montmorillonite) red-shift in the edge of the spectra compared with the free Eu(III) complex. These phenomena suggest a reduction in the energy involving $\pi - \pi^*$ transitions in the ligands, the result of the intercalation of the complex between interlayers of the clay mineral. This feature is probably due to the polar change of surrounding environment after intercalation. In hybrids, the complex is sandwiched by the negatively charged clay mineral layers; the charge distribution should become more symmetric than that of the free complex (Xin *et al.*, 2006). This result is well in agreement with the intensity ratio $I(^5\text{D}_0 \rightarrow ^7\text{F}_2) / I(^5\text{D}_0 \rightarrow ^7\text{F}_1)$ of photoluminescence data, and will be discussed later. Moreover, the other broad band around 510 nm is only clearly observable for the $[\text{Eu}(\text{Phen})_2]^{3+}$ -clay mineral hybrids. It may also be regarded as change for the electronic structures of the Eu(III) complex due to the electrostatic interaction between the intercalated Eu(III) complex and clay minerals after intercalation reaction.

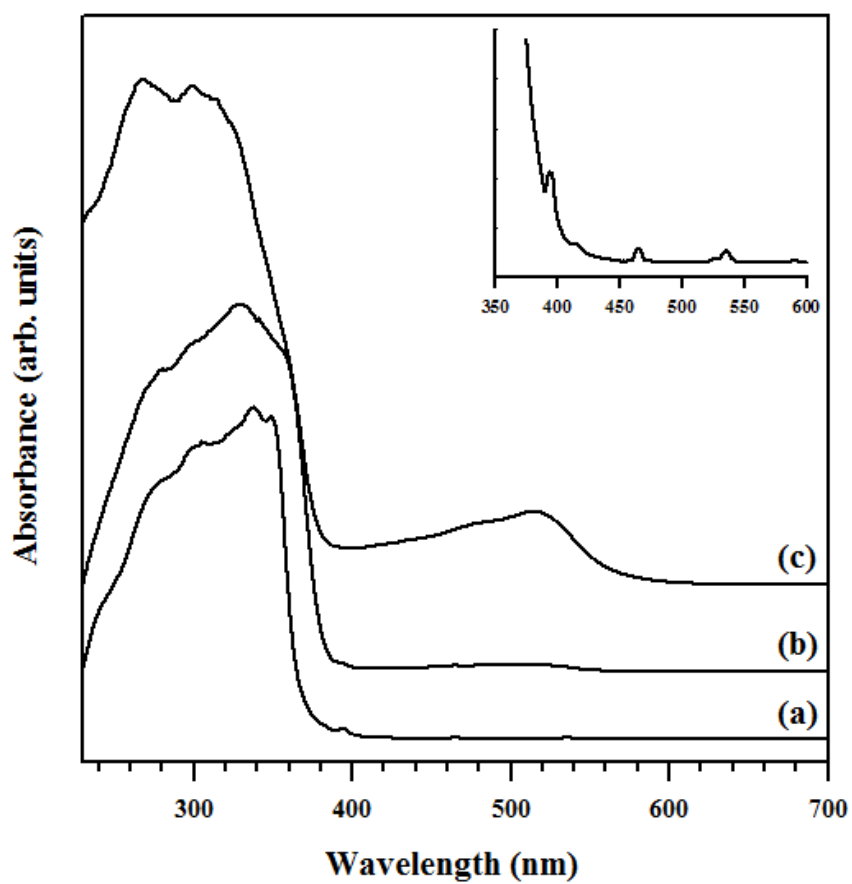


Figure 4-5. Diffuse reflectance UV-vis spectra of solid (a) Eu(III) complex, (b) $[\text{Eu}(\text{Phen})_2]^{3+}$ -hectorite hybrid and (c) $[\text{Eu}(\text{Phen})_2]^{3+}$ -montmorillonite hybrid. The inset represents the intra-configurational $4f$ - $4f$ transitions of Eu(III) complex.

4.4.5. Photoluminescence study

The room-temperature solid-state excitation and emission spectra of the Eu(III) complex are shown in Figure 4-6a. The previous research of the Eu(III) complex has reported a strong red photoluminescence upon radiation with ultraviolet light. The excitation spectrum was observed by monitoring the emission wavelength at 617 nm. The intense and broad excitation band around 330 nm was attributed to electronic transitions from the ground state level (π)S₀ to the excited level (π^*)S₁ of the organic phenanthroline ligand (Guo *et al.*, 2005). In addition, weaker peaks were observed at 395 and 465 nm (${}^7F_0 \rightarrow {}^5L_6$ and ${}^7F_0 \rightarrow {}^5D_2$, respectively), which are due to the intra-configurational $4f - 4f$ transitions of Eu(III) ions. The luminescence spectrum was measured with 328 nm as the excitation wavelength. The narrow peaks observed in the luminescence spectrum are transitions between the 5D_0 excited state and the different J levels of the ground term 7F (7F_J , J = 1 ~ 4) (Binnemans, 2009; Jenkins and Murray, 1998). They all exhibit the characteristic emission band at *ca.* 592, 617, 653 and 701 nm corresponding to ${}^5D_0 \rightarrow {}^7F_J$ (J = 1 ~ 4), respectively, with the ${}^5D_0 \rightarrow {}^7F_2$ transition as the dominant red emission. Two weak peaks at 538 and 557 nm are assigned to the transitions ${}^5D_1 \rightarrow {}^7F_1$ and ${}^5D_1 \rightarrow {}^7F_2$, respectively. The intensity ratio of I (${}^5D_0 \rightarrow {}^7F_2$) / I (${}^5D_0 \rightarrow {}^7F_1$) is 3.35 as shown in Table 4-2. This emission intensity ratio is very sensitive to the coordination symmetry of the Eu³⁺ ions, because the ${}^5D_0 \rightarrow {}^7F_1$ emission is due to the magnetic dipole and is independent of the surrounding environment, while the ${}^5D_0 \rightarrow {}^7F_2$ emission is due to the electric dipole and is sensitive to the crystal field symmetry (Jenkins and Murray, 1998; Jüstel, 2008). Such a high ratio is only possible when the europium ion does not occupy a site with inversion symmetry. So,

we can conclude that the pure Eu(III) complex has a low symmetry without an inversion center.

[Eu(Phen)₂]³⁺-clay mineral hybrids photo-luminescence spectra are shown in Figures 4-6b and 4-6c. All hybrid powder samples were observed to have a similar luminescence feature as the Eu(III) complex, except relatively lower intensities due to the dilution effect by the clay mineral host matrix. The amount of intercalated Eu(III) complex in each clay mineral was about 14.0 (in case of hectorite) and 13.4 (in case of montmorillonite) wt.%, as obtained from the elemental analysis results (table 1). The relative intensity of ⁵D₀ → ⁷F₂ transition of [Eu(Phen)₂]³⁺-hectorite and [Eu(Phen)₂]³⁺-montmorillonite is *ca.* 0.277 and 0.081, respectively, for the comparison of the Eu(III) complex itself. In the case of the [Eu(Phen)₂]³⁺-hectorite hybrid, the luminescence intensity per Eu(III) complex molecule in the hybrid was enhanced after it was intercalated into the hectorite host clay mineral. It can be noticed that intercalation of Eu(III) complex into the hectorite greatly make the reduction of the concentration quenching because intercalated complex molecules are homogeneously dispersed in the matrices (Wu *et al.*, 2000). The [Eu(Phen)₂]³⁺-montmorillonite also contains a similar amount of Eu(III) complex in the hybrid, but its luminescence intensity was lower than that of the hectorite hybrid. It is noteworthy here that the highest emission intensity (⁵D₀ → ⁷F₂) of [Eu(Phen)₂]³⁺-hectorite was *ca.* 3.4 times higher than that of [Eu(Phen)₂]³⁺-montmorillonite, due to the suppression of emission by quenching impurities in montmorillonite. Generally, natural clay mineral contains significant amounts of iron (Na⁺-montmorillonite contains about 1.37% of Fe), which undergoes a strong ligand to metal charge transfer transition, and this may interrupt the emission of intercalated Eu(III) complex in montmorillonite (Lezhnina *et al.*, 2007; Pimchan *et al.*, 2011). In order to

further quantitatively discuss this phenomenon, the IQE of all powder samples was measured and reported in Table 4-2. These results are also accordance with the conclusions obtained from intensity ratio values, such as quenching effect between natural and synthetic clay minerals.

Both of the emission spectra were measured with 295 nm as the excitation wavelength. As mentioned above, the intensity ratio ($I(^5D_0 \rightarrow ^7F_2) / I(^5D_0 \rightarrow ^7F_1)$) is sensitive to the symmetry around Eu^{3+} ions and provides valuable information about environmental change. The intensity ratio is significantly reduced from 3.35 for pure Eu(III) complex to 2.99 and 2.48 for $[\text{Eu(Phen)}_2]^{3+}$ -hectorite and $[\text{Eu(Phen)}_2]^{3+}$ -montmorillonite, respectively (Table 2). This result suggests that the intercalated $[\text{Eu(Phen)}_2]^{3+}$ complex ions are stabilized between the interlayer space of clay minerals, with a centrosymmetric coordination environment (Guo *et al.*, 2005; Xin *et al.*, 2006). In addition, the fact that the intensity ratio of $[\text{Eu(Phen)}_2]^{3+}$ -hectorite was higher than that of montmorillonite one could suggest that the intercalated complex ion was relatively asymmetric structure in hectorite. These mean we could expect that the intercalated molecules were more distorted coordination structure in hectorite. As a result, it is leading to smaller basal spacing of $[\text{Eu(Phen)}_2]^{3+}$ -hectorite compared with $[\text{Eu(Phen)}_2]^{3+}$ -montmorillonite accordance with XRD data.

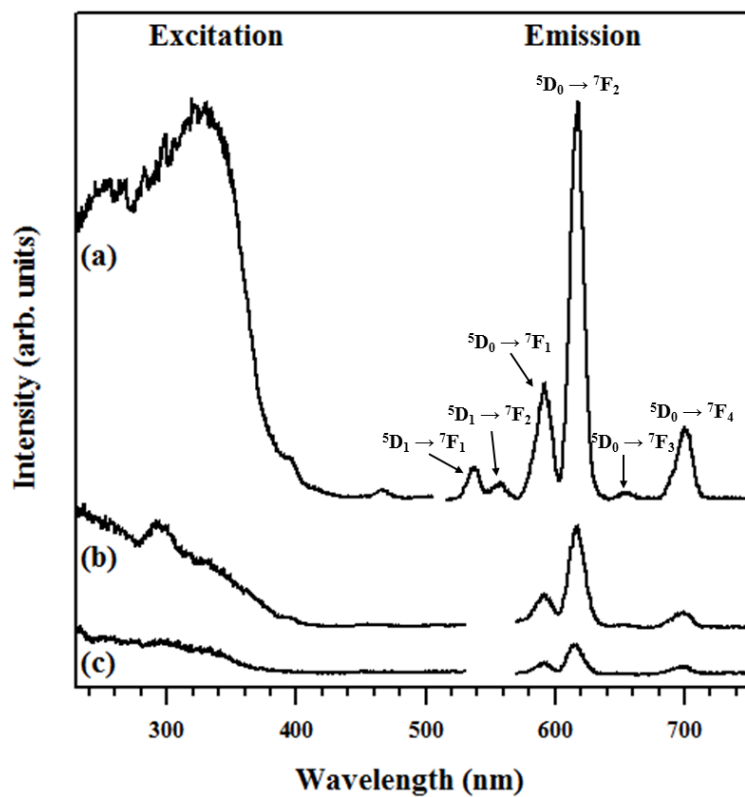


Figure 4-6. The room-temperature solid-state excitation and emission spectra of (a) Eu(III) complex, (b) $[\text{Eu}(\text{Phen})_2]^{3+}$ -hectorite hybrid and (c) $[\text{Eu}(\text{Phen})_2]^{3+}$ -montmorillonite hybrid.

Table 4-2. Photoluminescence data for Eu(III) complex and [Eu(Phen)₂]³⁺-clay mineral hybrids.

	Excitation wavelength (nm)	Intensity ratio ^a	QE (%)
Eu(III) complex	328	3.35	19.2 ^b
[Eu(Phen) ₂] ³⁺ -hectorite hybrid	295	2.99	9.9 ^b (2.7 ^c)
[Eu(Phen) ₂] ³⁺ - montmorillonite hybrid	295	2.48	2.1 ^b (2.6 ^d)

^a The intensity ratio of I (⁵D₀→⁷F₂) / I (⁵D₀→⁷F₁). ‘I’ means peak intensity of transition.

^b IQE.

^c The expected QE calculated from IQE of pure Eu(III) complex when normalized by 14.0 wt.% of [Eu(Phen)₂]³⁺ content in hectorite hybrid (19.2% × 0.14).

^d The expected QE calculated from IQE of pure Eu(III) complex when normalized by 13.4 wt.% of [Eu(Phen)₂]³⁺ content in montmorillonite hybrid (19.2% × 0.134).

4.4.6. Fingerprint developing test

The obtained $[\text{Eu}(\text{Phen})_2]^{3+}$ -clay mineral hybrids show characteristic photoluminescence. After the intercalation of Eu(III) complex into the clay matrix, the intercalated complex showed high thermal stability and enhanced adhesive properties. Pure Eu(III) complex alone did not exhibit high stability against environmental parameters, such as humidity, heat, light, etc. Thus it would be one of the critical factors to enhance the thermal stability of the Eu(III) complex as a fingerprint identification agent. In this regard, it is possible that the $[\text{Eu}(\text{Phen})_2]^{3+}$ -clay mineral hybrids may be used as a series of alternative photoluminescent labeling markers for enhanced latent fingerprint detection in forensic science. Figure 4-7 shows the preliminary test results from latent fingerprint detection on glass slides before and after UV irradiation (at 312 nm) by developing with the $[\text{Eu}(\text{Phen})_2]^{3+}$ -hectorite hybrid (Figure 4-7a and 4-7c) and $[\text{Eu}(\text{Phen})_2]^{3+}$ -montmorillonite hybrid (Figure 4-7b and 4-7d) powders. $[\text{Eu}(\text{Phen})_2]^{3+}$ -clay mineral hybrid particles can be clearly seen on residues of the fingerprint ridges, and their visibility can be further optimized for fingerprint identification purposes. Particularly, $[\text{Eu}(\text{Phen})_2]^{3+}$ -hectorite hybrid powder was much brighter than that of the montmorillonite hybrid, which is in agreement with fluorescence results. It is also noted that the powder size of $[\text{Eu}(\text{Phen})_2]^{3+}$ -hectorite hybrid may be further optimized for fingerprint identification purpose because fine particles adhere better than larger ones (Chen *et al.*, 2009). Thus, the $[\text{Eu}(\text{Phen})_2]^{3+}$ -hectorite hybrid particles can be clearly seen on the fingerprint residues details, without the use of background staining, as compared with the $[\text{Eu}(\text{Phen})_2]^{3+}$ -montmorillonite hybrid, resulting in good contrast for enhanced detection.

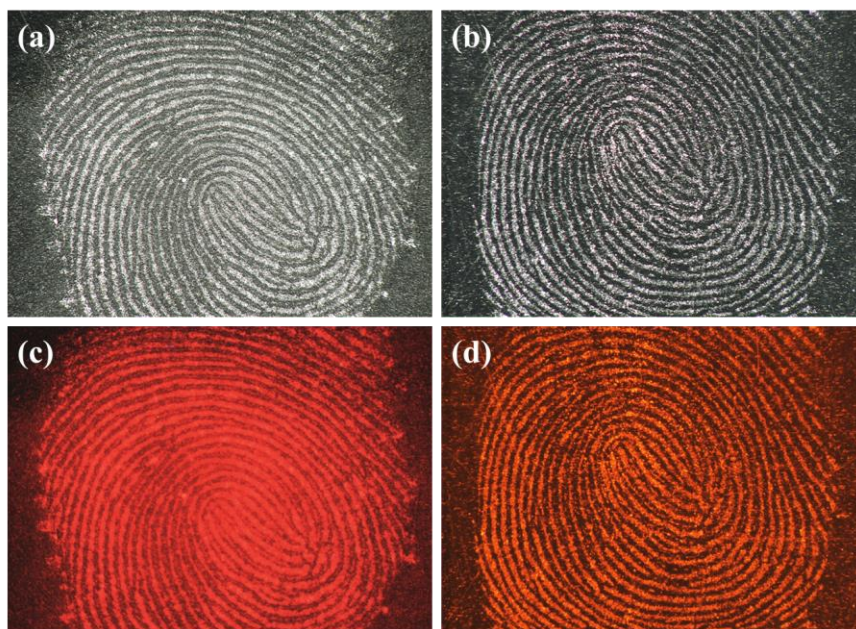


Figure 4-7. Photographs of latent fingerprints on glass slides developed with [(a) and (c)] the $[\text{Eu}(\text{Phen})_2]^{3+}$ -hectorite hybrid and [(b) and (d)] $[\text{Eu}(\text{Phen})_2]^{3+}$ -montmorillonite hybrid powders before [(a) and (b)] and after [(c) and (d)] UV irradiation at 312 nm, respectively.

4.5. Conclusion

In conclusion, we report the hybridization of Eu(III) complex with synthetic hectorite and natural montmorillonite clay mineral, which leads to a remarkably sensitive fingerprint development agent. The intercalated Eu(III) complex species in clay mineral nanohybrids showed much higher thermal, chemical and mechanical stabilities than pure Eu(III) complex. In addition, characteristic photoluminescence phenomena are maintained even after intercalation. Accordingly, the $[\text{Eu}(\text{Phen})_2]^{3+}$ -clay mineral nanohybrids may be effectively used as a photoluminescent labeling marker for fingerprint detection and identification. The luminescence intensities of $[\text{Eu}(\text{Phen})_2]^{3+}$ -hectorite was much higher than that of $[\text{Eu}(\text{Phen})_2]^{3+}$ -montmorillonite, due to the absence of quenching impurity ion such as iron in the hectorite host clay mineral along with greatly reduced concentration quenching. Our results indicate that the specific selection of clay mineral as a host material is a factor which critically affects functionalizing Eu(III) complexes in nanohybrids.

4.6. References

1. Bansal, B.M., Damien, D., Koehly, G., 1969. Complexes of rare-earth element chlorides with 1,10-phenanthroline. *Inorg. Nucl. Chem. Letters* 5, 509-514.
2. Binnemans, K., 2009. Lanthanide-based luminescent hybrid materials. *Chem. Rev.* 109, 4283-4374.
3. Bouwe, R.G.B., Tonle, I.K., Letaief, S., Ngameni, E., Detellier, C., 2011. Structural characterization of 1,10-phenanthroline-montmorillonite intercalation compounds and their application as low-cost electrochemical sensors for Pb(II) detection at the sub-nanomolar level. *Appl. Clay Sci.* 52, 258-265.
4. Bünzli, J.-C.G., Piguet, C., 2005. Taking advantage of luminescent lanthanide ions. *Chem. Soc. Rev.* 34, 1048-1077.
5. Celedon, S., Quiroz, C., Gonzalez, G., Sotomayor Torres, C.M., Benavente, E., 2009. Lanthanides-clay nanocomposites: synthesis, characterization and optical properties. *Mater. Res. Bull.* 44, 1191-1194.
6. Cerveau, G., Corriu, R.J.P., Framery, E., 2001. Nanostructured organic-inorganic hybrid materials: kinetic control of the texture. *Chem. Mater.* 13, 3373-3388.
7. Chen, Q., Kerk, W.T., Soutar, A.M., Zeng, X.T., 2009. Application of dye intercalated bentonite for developing latent fingerprints. *Appl. Clay Sci.* 44, 156-160.
8. Choy, J.H., Lee, H.C., Jung, H., Kim, H., Boo, H., 2002a. Exfoliation and restacking route to anatase-layered titanate nanohybrid with enhanced

- photocatalytic activity. *Chem. Mater.* 14, 2486-2491.
9. Choy, J.H., Jung, H., Han, Y.S., Yoon, J.B., Shul, Y.G., Kim, H.J., 2002b. New CoO-SiO₂-sol pillared clays as catalysts for NO_x conversion. *Chem. Mater.* 14, 3823-3828.
10. Cui, Y., Yue, Y., Qian, G., Chen, B., 2012. Luminescent functional metal-organic frameworks. *Chem. Rev.* 112, 1126-1162.
11. Eliseeva, S.V., Bünzli, J.-C.G., 2010. Lanthanide luminescence for functional materials and bio-sciences. *Chem. Soc. Rev.* 39, 189-227.
12. Gao, F., Lv, C., Han, J., Li, X., Wang, Q., Zhang, J., Chen, C., Li, Q., Sun, X., Zheng, J., Bao, L., Li, X., 2011. CdTe-montmorillonite nanocomposite: control synthesis, UV radiation-dependent photoluminescence, and enhanced latent fingerprint detection. *J. Phys. Chem. C* 115, 21574-21583.
13. Guo, X., Fu, L., Zhang, H., Carlos, L.D., Peng, C., Guo, J., Yu, J., Deng, R., Sun, L., 2005. Incorporation of luminescent lanthanide complex inside the channels of organically modified mesoporous silica via template-ion exchange method. *New J. Chem.* 29, 1351-1358.
14. Hagerman, M.E., Salamone, S.J., Herbst, R.W., Payeur, A.L., 2003. Tris(2,2'-bipyridine)ruthenium(II) cations as photoprobes of clay tactoid architecture within hectorite and laponite films. *Chem. Mater.* 15, 443-450.
15. Jenkins, A.L., Murray, G.M., 1998. Enhanced luminescence of lanthanides: determination of europium by enhanced luminescence. *J. Chem. Ed.* 75, 227-230.
16. Jin, T., Tsutsumi, S., Deguchi, Y., Machida, K., Adachi, G., 1997. Preparation and luminescence characteristics of the europium and terbium

complexes incorporated into a silica matrix using a sol-gel method. *J. Alloys Comp.* 252, 59-66.

17. Jung, H., Kim, H.M., Choy, Y.B., Hwang, S.J., Choy, J.H., 2008a. Laponite-based nanohybrid for enhanced solubility and controlled release of itraconazole. *Int. J. Pharm.* 349, 283-290.

18. Jung, H., Kim, H.M., Choy, Y.B., Hwang, S.J., Choy, J.H., 2008b. Itraconazole-laponite: kinetics and mechanism of drug release. *Appl. Clay Sci.* 40, 99-107.

19. Jüstel, T., 2008. Phosphors for plasma display panels, in : Ronda, C.R., (Eds.), *Luminescence: From theory to applications*, Willey-VCH Verlag GmbH & Co. KGaA, Weinheim, Germany, pp. 61-73.

20. Khan, A.I., O'Hare, D., 2002. Intercalation chemistry of layered double hydroxides: recent developments and applications. *J. Mater. Chem.* 12, 3191-3198.

21. Khaorapong, N., Ontam, A., Ogawa, M., 2010. Formation of ZnS and CdS in the interlayer spaces of montmorillonite. *Appl. Clay Sci.* 50, 19-24.

22. Kido, J., Okamoto, Y., 2002. Organo lanthanide metal complexes for electroluminescent materials. *Chem. Rev.* 102, 2357-2368.

23. Kortüm, G., Braun, W., Herzog, G., 1963. Principles and techniques of diffuse-reflectance spectroscopy. *Angew. Chem., Int. Ed. Engl.* 2, 333-404.

24. Kráčalík, M., Studenovský, M., Mikešová, J., Sikora, A., Thomann, R., Friedrich, C., Fortelný, I., Simoník, J., 2007. Recycled PET nanocomposites improved by silanization of organoclays. *J. Appl. Polym. Sci.* 106, 926-937.

25. Letaief, S., Detellier, C., 2007. Nanohybrid materials from the

- intercalation of imidazolium ionic liquids in kaolinite. *J. Mater. Chem.* 17, 1476-1484.
26. Lezhnina, M., Benavente, E., Bentlage, M., Echevarria, Y., Klumpp, E., Kynast, U., 2007. Luminescent hybrid material based on a clay mineral. *Chem. Mater.* 19, 1098-1102.
27. Madejová, J., 2003. FTIR techniques in clay mineral studies. *Vib. Spectrosc.* 31, 1-10.
28. Okada, T., Ehara, Y., Ogawa, M., 2007. Adsorption of Eu^{3+} to smectites and fluoro-tetrasilicic mica. *Clays Clay Miner.* 55, 348-353.
29. Peng, C., Zhang, H., Yu, J., Meng, Q., Fu, L., Li, H., Sun, L., Guo, X., 2005. Synthesis, characterization, and luminescence properties of the ternary europium complex covalently bonded to mesoporous SBA-15. *J. Phys. Chem. B* 109, 15278-15287.
30. Pimchan, P., Khaorapong, N., Ogawa, M., 2011. Preparation of a series of group XIII metal-quinolate complexes in natural and synthetic smectites. *Appl. Clay Sci.* 54, 287-291.
31. Puntus, L.N., Lyssenko, K.A., Antipin, M.Y., Bünzli, J.-C.G., 2008. Role of inner- and outer-sphere bonding in the sensitization of Eu^{III} -luminescence deciphered by combined analysis of experimental electron density distribution function and photophysical data. *Inorg. Chem.* 47, 11095-11107.
32. Sánchez, A., Echeverría, Y., Torres, C.M.S., González, G., Benavente, E., 2006. Intercalation of europium (III) species into bentonite. *Mater. Res. Bull.* 41, 1185-1191.
33. Wu, R., Zhao, H., Su, Q., 2000. Photoacoustic and fluorescence studies of

silica gels doped with rare earth salicylic acid complexes. *J. Non-Cryst. Solids* 278, 223-227.

34. Xin, H., Ebina, Y., Ma, R., Takada, K., Sasaki, T., 2006. Thermally stable luminescent composites fabricated by confining rare earth complexes in the two-dimensional gallery of titania nanosheets and their photophysical properties. *J. Phys. Chem. B* 110, 9863-9868.

35. Zhang, H., Pan, D., Duan, X., 2009. Synthesis, characterization, and magnetically controlled release behavior of novel core-shell structural magnetic ibuprofen-intercalated LDH nanohybrids. *J. Phys. Chem. C* 113, 12140-12148.

36. Zhu, M.-Z., Ding, K.-Y., Xu, S.-H., Jiang, X., 2009. Adsorption of phosphate on hydroxyaluminum- and hydroxyiron-montmorillonite complexes. *J. Hazard. Mater.* 165, 645-651.

Chapter 5

**Nano Forensic Application:
Latent Fingerprint Detection on Diverse Surfaces
by means of the Multifunctional Properties of
Nanocomposite powder**

5.1. Abstract

We used photoluminescent $[\text{Eu}(\text{Phen})_2]^{3+}$ -clay nanocomposite powder to enhance the visualization of latent fingerprints on diverse porous and non-porous surfaces. We obtained nanocomposites powder through the ion exchange reaction of interlayer sodium cation in two different types of clay (synthetic hectorite type and natural montmorillonite-type) with europium (III) complex ion. Moreover, in order to improve interaction between latent fingerprint residue and nanocomposites powder, we successfully modified the surface property of $[\text{Eu}(\text{Phen})_2]^{3+}$ -hectorite nanocomposite to be more hydrophobic by means of simple silylation reaction with hydroxyl group at the edge of clay and hexadecyltrimethoxysilane molecules. The nanocomposites powder showed a characteristic red emission at wavelength 617 nm. We detected and visualized latent fingerprints on the non-porous surfaces of glass, polymer film, plastic, metal, and adhesive tape. Also, we detected latent fingerprints on the porous surfaces of adhesive tape made of paper, credit card receipts, and paper money.

5.2. Introduction

Fingerprints are critical evidence in crime scenes, because of the ability to identify individuals by the unique ridge pattern of skin on the human finger ^{1,2}. The latent fingerprint consists of many chemical components that are organic molecules, such as fatty acids, squalene, amino acids and inorganic salts ³. Even though a large number of fingerprints may be left on the evidence, most of the fingerprints at a crime scene are not visible, due to the various limitations on detection, such as the lack of a suitable method, a variety of surfaces, and unknown contamination ⁴. Moreover, fingerprint residue tends to change the chemical components, such as moisture and oily components, depending on evaporation with chemical environments at the crime scene. For these reasons, fingerprint visualization methodology is one of the main topics of study in the forensic science area ⁵.

In order to detect and develop latent fingerprints, various powders or chemical reagents, such as charcoal, magnetic powders or ninhydrin ^{6,7}, have been applied in forensic science, using chemical ^{8,9}, physical ¹⁰, and optical detection ¹¹. The powder method for detecting latent fingerprints could provide not only fast and easy development of latent fingerprints, but also more chances to design multifunction properties, such as photoluminescent or magnetic properties. To detect latent fingerprints, the color contrast between the surface and powder must be considered. Therefore, fingerprint powders are commercially available in a variety of colors. Grey magnetic powder and black charcoal powder have been applied to dark and white surfaces, respectively. To overcome this problem of color contrast, various fluorescent

agents have been considered in forensic science, such as organic dye or lanthanide complex¹². An enhanced photoluminescent property could be helpful to obtain distinctive images with fast development and high sensitivity latent fingerprint detection.

More recent, there has been a unique nanotechnology for latent fingerprint detection with the novel and intriguing physical and electronic properties of various nano-sized materials^{13, 14}. Functionalized gold nanoparticles provide a novel approach for improved fingerprint detection *via* surface plasmon-based techniques^{15, 16}, while quantum dots show size-dependent fluorescent properties at the nanoscale^{17, 18}. Moreover, combinations of different nano-sized materials show unusual and synergetic physicochemical properties, which cannot be achieved by any single component. Various physico-chemical processes have been applied to the production of such nanocomposite materials. Among them, the intercalation reaction is expected to be one of the most effective ways to prepare noble nanocomposite materials of the desired functionality. In this regard, clay minerals in particular have attracted a great deal of attention, because they can keep various cationic species within their nano-sized interlayer space^{19, 20}.

In this paper, we focused on the detection and visualization of latent fingerprint on diverse surfaces using nanocomposite materials with multifunctional properties of photoluminescence and controlled surface polarity. To enhance photoluminescent properties, we synthesized Eu (III) complex $[\text{EuCl}_2(\text{Phen})_2(\text{H}_2\text{O})_2]\text{Cl}\cdot\text{H}_2\text{O}$ as a guest photoluminescent agent, and used two different types of clay minerals, Laponite-XLG (synthetic hectorite

type) and Kunipia-F (natural montmorillonite-type) as the host clay minerals. In addition, to control surface polarity of the europium complex intercalated laponite nanocomposite, we modified the surface of the nanocomposite to react to hexadecyltrimethoxysilane (HDTMS) by a simple silylation reaction. For real application of latent fingerprint detection, we applied the technique to non-porous surfaces of glass, polymer film, plastic, metal, and adhesive tape; and porous surfaces of adhesive tape made of paper, credit card receipts, and paper money. Finally, we were able to clearly visualize the latent fingerprint on non-porous or porous surfaces by enhanced photoluminescence and controlled surface properties of the obtained nanocomposites under 312 nm of UV light irradiation.

5.3. Experimental Section

5.3.1 Materials.

Europium (III) chloride hexahydrate (99.99%), 1, 10-phenanthroline (Phen, $\geq 99\%$), hexadecyltrimethoxysilane (HDTMS, $\geq 85\%$) and L-ascorbic acid ($\geq 99\%$) were purchased from Sigma Aldrich. Ethyl alcohol (99%) and hexane (99.9%) were purchased from Daejung Chemicals and Burdick & Jackson, respectively. For host clay minerals, Na⁺-montmorillonite and Na⁺-hectorite were used. Na⁺-montmorillonite (Kunipia F, Kunimine Corp.) was used with the chemical formula of Na_{0.35}K_{0.01}Ca_{0.02}(Si_{3.88}Al_{0.12})(Al_{1.53}Mg_{0.32}Fe_{0.10})O₁₀(OH)₂·nH₂O, the dimensions of one layer of montmorillonite being ca. 1 nm×1.5 μm, with a negative charge density of 0.022 e⁻/Å². Na⁺-hectorite (Laponite XLG, Rockwood Ltd.) has the chemical formula of Na_{0.3}(Si₄)(Mg_{2.7}Li_{0.3})O₁₀(OH)₂·nH₂O, with the dimensions of one layer of hectorite being ca. 1 nm × 25 nm, with a negative charge density of 0.014 e⁻/Å². All the other reagents were of analytical grade.

5.3.2 Synthesis of [Eu(Phen)₂]³⁺-montmorillonite/hectorite nanocomposites.

We synthesized the [Eu(Phen)₂]³⁺-montmorillonite and hectorite nanocomposites in-house, according to previously reported methods [21]. We obtained the guest europium (III) complex ([EuCl₂(Phen)₂(H₂O)₂]Cl·H₂O) by simple complex reaction between europium chloride hexahydrate (EuCl₃·6H₂O) and 1,10-phenanthroline (Phen) as a 1:2 molar ratio of Eu³⁺ ion to ligand molecules. We dissolved 2.7224 g of EuCl₃·6H₂O and 2.6779 g of 1,10-phenanthroline in each absolute ethanol (20 mL) solution, and mixed and stirred the two ethanoic solutions, until a white compound precipitated.

Finally, we obtained the product by filtration, drying, and recrystallization. We mixed each 1wt% clay mineral dispersion aqueous solution with Eu (III) complex aqueous solution (corresponding to the 1.2-fold CEC of each clay mineral) under vigorous stirring for 24 h at room temperature. After the ion exchange reaction, we separated the product, washed it with deionized water, and then dried it in a vacuum.

5.3.3 Preparation of $[\text{Eu}(\text{Phen})_2]^{3+}$ -hectorite-HDTMS nanocomposite.

We dispersed 1.0 g of as-prepared $[\text{Eu}(\text{Phen})_2]^{3+}$ -hectorite in 20 mL of ethyl alcohol containing L-ascorbic acid (0.01 g) (Solution 1). The ascorbic acid plays a role as an acid catalyst for the hydrolysis reaction of silane with the clay surface. We dissolved 1.37 mL of HDTMS in 20 mL of hexane (Solution 2). We then mixed and stirred solutions 1 and 2 for 24 h at room temperature under a nitrogen atmosphere. We separated the HDTMS-grafted $[\text{Eu}(\text{Phen})_2]^{3+}$ -hectorite composite ($[\text{Eu}(\text{Phen})_2]^{3+}$ -hectorite-HDTMS composite) by centrifugation, washed it with hexane and ethyl alcohol several times to remove the excess HDTMS or L-ascorbic acid, and then dried it in a vacuum oven at 120 °C.

5.3.4 X-ray diffraction and Photoluminescent measurement.

We recorded the powder X-ray diffraction (XRD) patterns on a diffractometer (Bruker D8 advance), using graphite-monochromatized Cu K_α radiation ($\lambda = 1.5418 \text{ \AA}$), an operating voltage of 40 kV, and a current of 30 mA. We determined fluorescence emission spectra using a Cary Eclipse fluorescence spectrophotometer (Varian) with an excitation wavelength of 295 nm, slit width of 10 nm, and PMT voltage of 800 V at room temperature.

5.3.5 Procedures of latent fingerprint development.

The latent fingerprint detection is simply performed on non-porous and porous surfaces using $[\text{Eu}(\text{Phen})_2]^{3+}$ -montmorillonite/hectorite and $[\text{Eu}(\text{Phen})_2]^{3+}$ -hectorite-HDTMS nanocomposites, respectively. First, the fingers of a middle-aged male donor were cleaned with soap and water, and allowed to air dry without touching anything for 5 min. He then deposited latent fingerprints for 1 or 2 seconds on non-porous surfaces of glass, polymer film, plastic, metal, and adhesive tape surfaces. We then brushed nanocomposite powders on the latent fingerprints using a commercial make-up brush. We observed the resulting fingerprints by monitoring under UV light at 312 nm, using a Video spectral comparator 6000 (Foster + Freeman Ltd., UK). In the same procedure, we detected latent fingerprints on porous surfaces of adhesive tape made of paper, credit card receipts, and paper money.

5.4. Results and Discussion

5.4.1. Sample characterization.

Figure 5-1 (a) schematically represents the intercalation reaction of $[\text{Eu}(\text{Phen})_2]^{3+}$ -montmorillonite/hectorite nanocomposites. When using both montmorillonite and hectorite clays as a host matrix, sodium cations existing in the interlayer of clays are easily replaced by $[\text{Eu}(\text{Phen})_2]^{3+}$ complex ions through the ion exchange process, thus permitting complex ions to be intercalated into the interlayer of clays. Figure 5-2 (a) shows that our XRD analysis confirmed that the characteristic peaks of Eu (III) complex disappeared in both nanocomposites. As a result of intercalation reaction, the intercalated complex showed high chemical and mechanical stabilities, enhanced adhesive property, and in addition, maintained the characteristic fluorescence phenomena of $\text{Eu}(\text{Phen})_2$ complex, even after intercalation reaction. The emission peaks at 592, 617, 653, and 701 nm could correspond to the $^5\text{D}_0 \rightarrow ^7\text{F}_j$ ($J = 1-4$) transitions of Eu (III) ion with the dominated $^5\text{D}_0 \rightarrow ^7\text{F}_2$ red emission (Fig. 5-2 (b)). However, the 617 nm red emission intensity of $[\text{Eu}(\text{Phen})_2]^{3+}$ -hectorite was much higher than that of $[\text{Eu}(\text{Phen})_2]^{3+}$ -montmorillonite, because hectorite host clay has free quenching impurities, such as iron ion ²¹.

Furthermore, Fig. 5-1 (b) shows that the surface of $[\text{Eu}(\text{Phen})_2]^{3+}$ -hectorite nanocomposite, which possesses hydrophilic group (-OH), was modified by the HDTMS through silylation reaction. By doing control surface polarity of $[\text{Eu}(\text{Phen})_2]^{3+}$ -hectorite nanocomposite, the obtained particles were further prone to physically adhere to fingerprint ridges, due to van der Waals interactions between the long alkyl chain of HDTMS and the oily components of fingerprint residues ²⁰. The XRD pattern of $[\text{Eu}(\text{Phen})_2]^{3+}$ -hectorite-HDTMS was almost identical to that of $[\text{Eu}(\text{Phen})_2]^{3+}$ -hectorite, indicating

that silylation reaction with HDTMS does not significantly affect the crystal structure of intercalated nanocomposite²² (Fig.5- 2 (a)).

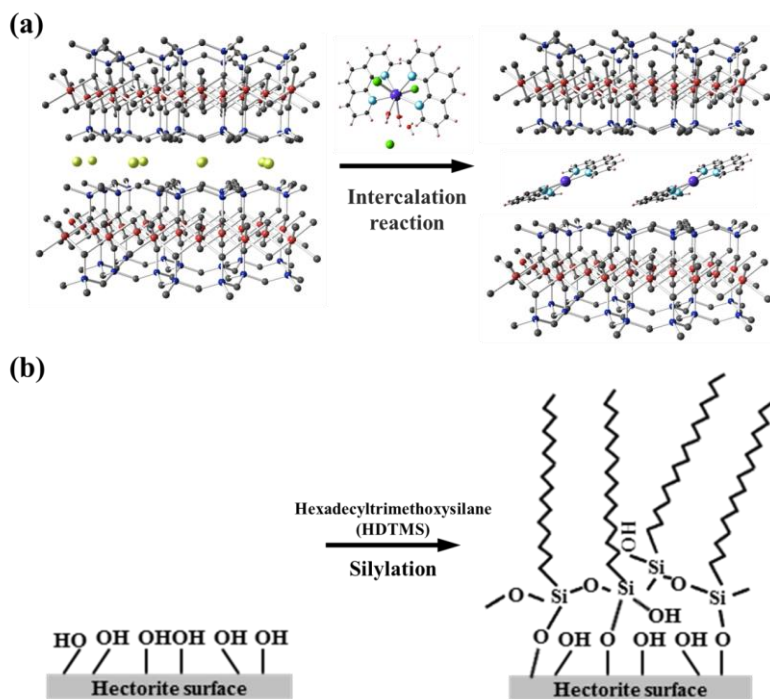


Figure 5-1. Schematic representation of (a) intercalation reaction for [Eu(Phen)₂]³⁺-montmorillonite/hectorite nanocomposites and (b) silylation for [Eu(Phen)₂]³⁺-hectorite-HDTMS nanocomposite.

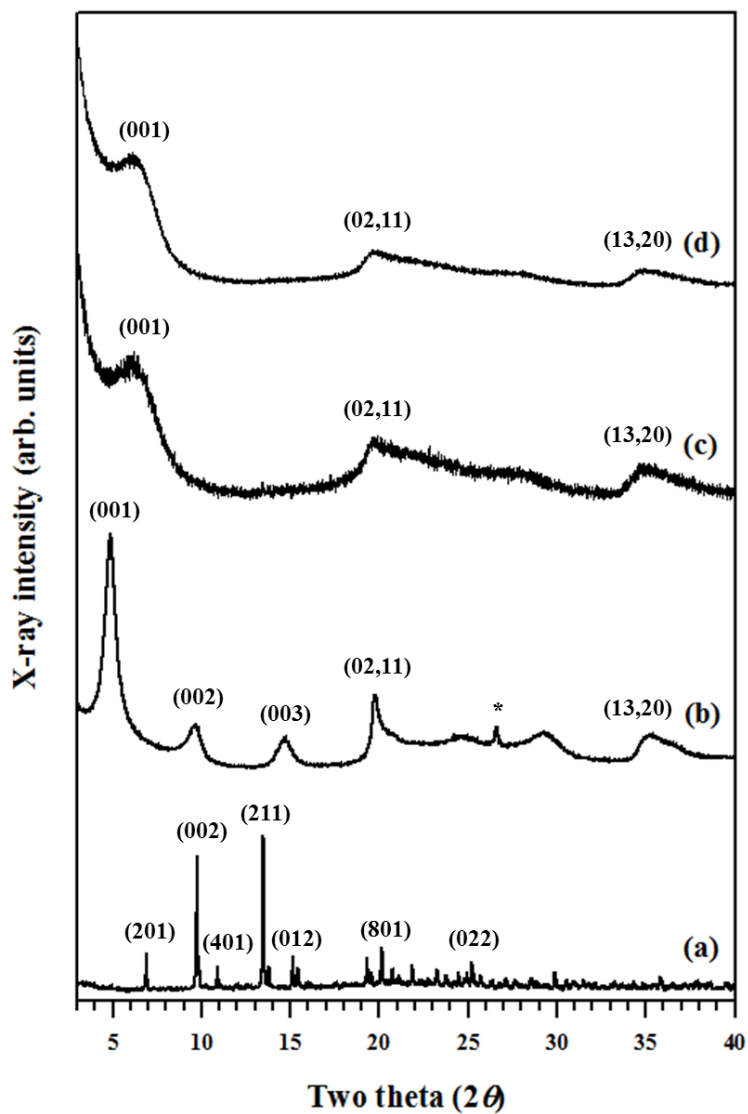


Figure 5-2(a). X-ray diffraction patterns of (a) Eu(III) complex, (b) $[\text{Eu}(\text{Phen})_2]^{3+}$ -montmorillonite nanocomposite (*: quartz), (c) $[\text{Eu}(\text{Phen})_2]^{3+}$ -hectorite nanocomposite and (d) $[\text{Eu}(\text{Phen})_2]^{3+}$ -hectorite-HDTMS nanocomposite.

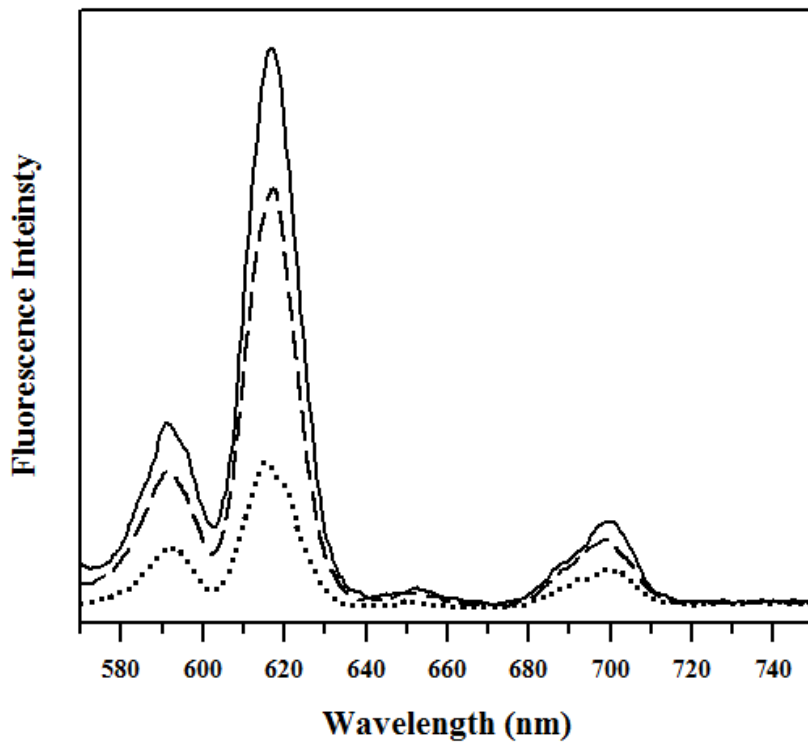


Figure 5-2(b). The solid-state emission spectra of $[\text{Eu}(\text{Phen})_2]^{3+}$ -montmorillonite nanocomposite (dotted line), $[\text{Eu}(\text{Phen})_2]^{3+}$ -hectorite nanocomposite (solid line) and $[\text{Eu}(\text{Phen})_2]^{3+}$ -hectorite-HDTMS nanocomposite (dashed line).

5.4.2. Fingerprint detection on non-porous surfaces.

Figure 5-3 shows latent fingerprint images by $[\text{Eu}(\text{Phen})_2]^{3+}$ -montmorillonite composite powder deposited on non-porous surfaces of glass, polymer film, plastic, metal, and adhesive tape. We clearly obtained sufficient contrast between dark color background and red fingerprint ridge detail on glass, polymer film, and metal surfaces. Also, we obtained most of the fingerprint ridges on plastic and adhesive tape surfaces. Figure 5-4 shows the development of latent fingerprints by $[\text{Eu}(\text{Phen})_2]^{3+}$ -hectorite composite powder. In particular, we obtained superior fingerprint images on glass, plastic, and metal surfaces; and most of the fingerprint ridges on polymer film and adhesive tape. Lastly, Fig. 5-5 shows that the detection of latent fingerprints by $[\text{Eu}(\text{Phen})_2]^{3+}$ -hectorite-HDTMS composite powder provided clear fingerprint ridge detail on glass surface, and most of the fingerprint ridges on polymer film, plastic, metal, and adhesive tape surfaces.

Fingerprint detection on non-porous surfaces with previous nanocomposites effectively showed the photoluminescent property with clarity, and for most of the fingerprint ridge. Although the surface of $[\text{Eu}(\text{Phen})_2]^{3+}$ -montmorillonite and $[\text{Eu}(\text{Phen})_2]^{3+}$ -hectorite nanocomposites has a relatively hydrophilic nature compared with that of surface-modified $[\text{Eu}(\text{Phen})_2]^{3+}$ -hectorite-HDTMS nanocomposite, there is no significant difference in the detection of latent fingerprints on non-porous surfaces.

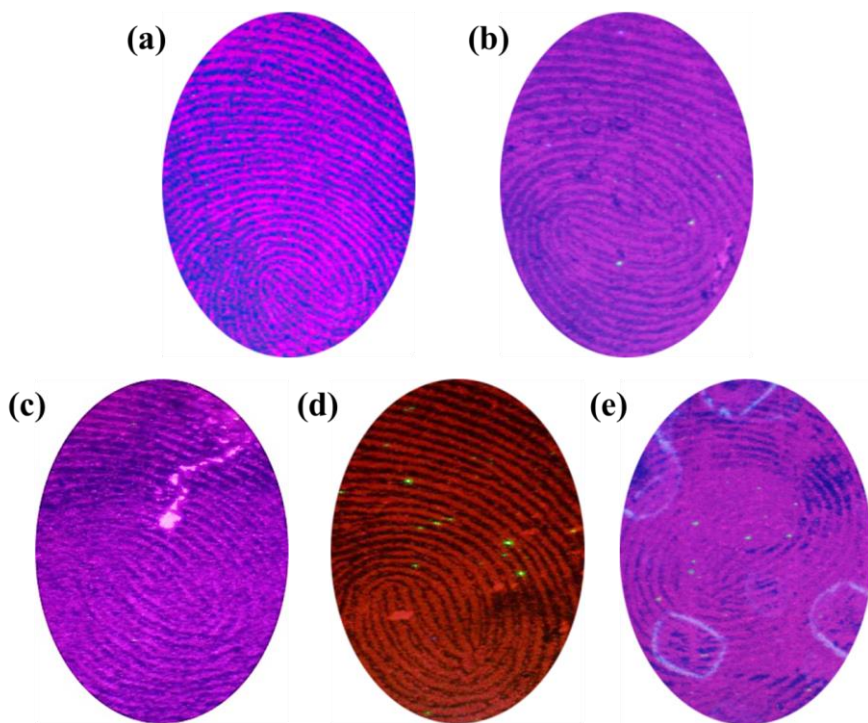


Figure 5-3. Latent fingerprint images developed by $[\text{Eu}(\text{Phen})_2]^{3+}$ -montmorillonite nanocomposite deposited on different non-porous surfaces illuminated with 312 nm light. Fingerprints on (a) glass, (b) polymer film, (c) plastic, (d) metal and (e) adhesive tape are shown.

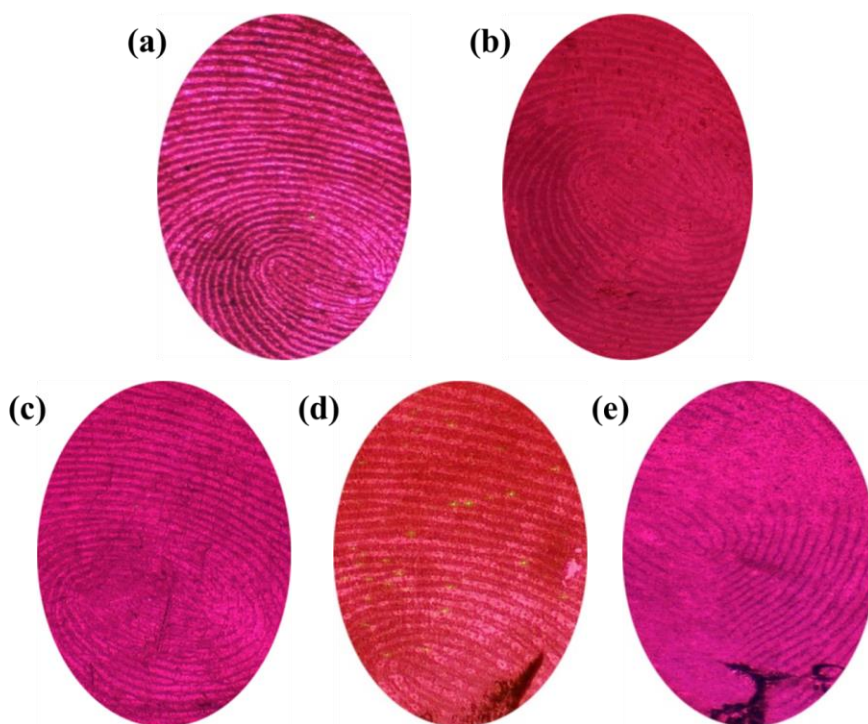


Figure 5-4. Latent fingerprint images developed by $[\text{Eu}(\text{Phen})_2]^{3+}$ -hectorite nanocomposite deposited on different non-porous surfaces illuminated with 312 nm light. Fingerprints on (a) glass, (b) polymer film, (c) plastic, (d) metal and (e) adhesive tape are shown.

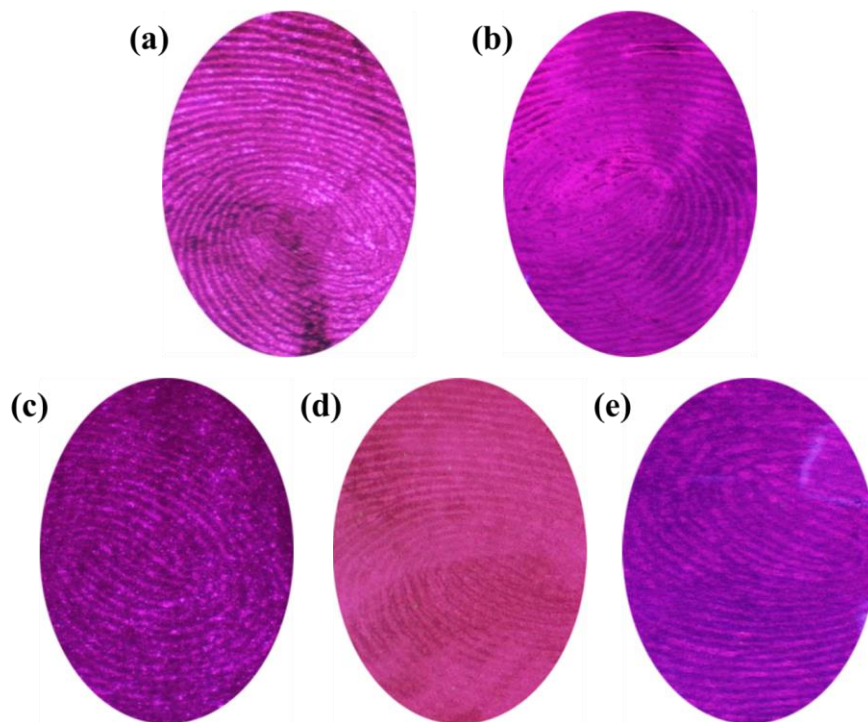


Figure 5-5. Latent fingerprint images developed by $[\text{Eu}(\text{Phen})_2]^{3+}$ -hectorite-HDTMS nanocomposite deposited on different non-porous surfaces illuminated with 312 nm light. Fingerprints on (a) Glass, (b) polymer film, (c) plastic, (d) metal and (e) adhesive tape are shown.

5.4.3. Fingerprint detection on porous surfaces.

Figure 5-6 shows photographs of latent fingerprints developed with $[\text{Eu}(\text{Phen})_2]^{3+}$ -montmorillonite composite on porous surfaces of tape made of paper, traditional credit card receipts, and credit card receipts made of electronic paper, under 312 nm of UV illumination. We obtained sufficient contrast between the background and red ridges in the detection images of latent fingerprints on tape made of paper, which is critical for forensic investigations. Also, we obtained faint fingerprint images on traditional credit card receipts and credit card receipts made of electronic paper. Figure 5-7 shows the development of latent fingerprints by $[\text{Eu}(\text{Phen})_2]^{3+}$ -hectorite composite. The fingerprint images show clear fingerprint ridge detail on the tape made of paper, most of the fingerprint ridges on the traditional credit card receipt, and faint fingerprint ridges on the credit card receipt made of electronic paper, respectively. The green and blue background colors on the credit card receipt differ from the red background color of tape made of paper. The background colors on the traditional credit card receipt result in less effective fingerprint detection when compared to that on the background color on tape made of paper.

Figure 5-8 shows photographs of latent fingerprints developed with surface modified $[\text{Eu}(\text{Phen})_2]^{3+}$ -hectorite-HDTMS nanocomposite on porous surfaces of tape made of paper, traditional credit card receipts, and credit card receipts made of electronic paper. Credit card receipts made of electronic paper show most of the fingerprint ridges, but tape made of paper and traditional credit card receipts show faint fingerprint images. Figure 5-9 shows a comparison of the latent fingerprints developed using the different nanocomposites $[\text{Eu}(\text{Phen})_2]^{3+}$ -montmorillonite/hectorite and $[\text{Eu}(\text{Phen})_2]^{3+}$ -hectorite-HDTMS, on paper money surfaces. We obtained superior fingerprint

images by the surface-modified $[\text{Eu}(\text{Phen})_2]^{3+}$ -hectorite-HDTMS nanocomposite with a hydrophobic surface nature, and we obtained most of the fingerprint ridges by $[\text{Eu}(\text{Phen})_2]^{3+}$ -montmorillonite and hectorite composite powders, respectively.

Table 5-1 shows that the detection of latent fingerprints by the previous nanocomposites on non-porous surfaces show clear fingerprint ridge detail, and most of the fingerprint ridges. On the other hand, the detection on porous surfaces shows good images by $[\text{Eu}(\text{Phen})_2]^{3+}$ -hectorite and $[\text{Eu}(\text{Phen})_2]^{3+}$ -hectorite-HDTMS nanocomposites. These results support the notion that latent fingerprint development could be strongly affected by the size of host clay minerals.

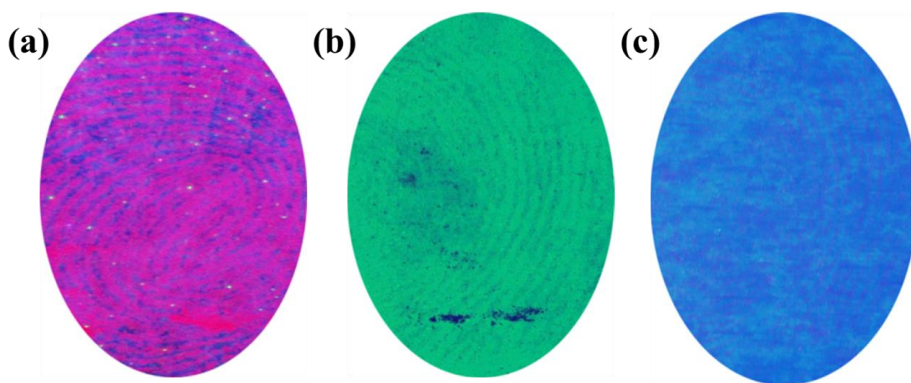


Figure 5-6. Photographs of latent fingerprints developed with $[\text{Eu}(\text{Phen})_2]^{3+}$ -montmorillonite nanocomposite on porous surfaces of (a) tape made of paper, (b) traditional credit card receipt and (c) credit card receipt made of electronic paper under UV illumination at 312 nm.

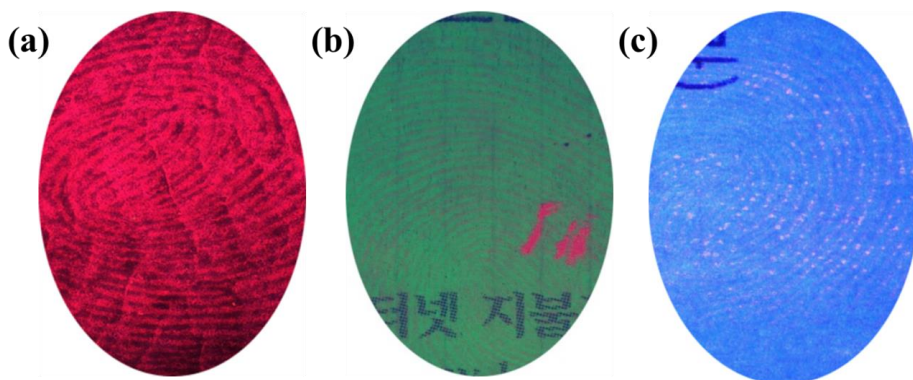


Figure 5-7. Photographs of latent fingerprints developed with $[\text{Eu}(\text{Phen})_2]^{3+}$ -hectorite nanocomposite on porous surfaces of (a) tape made of paper, (b) traditional credit card receipt and (c) credit card receipt made of electronic paper under UV illumination at 312 nm.

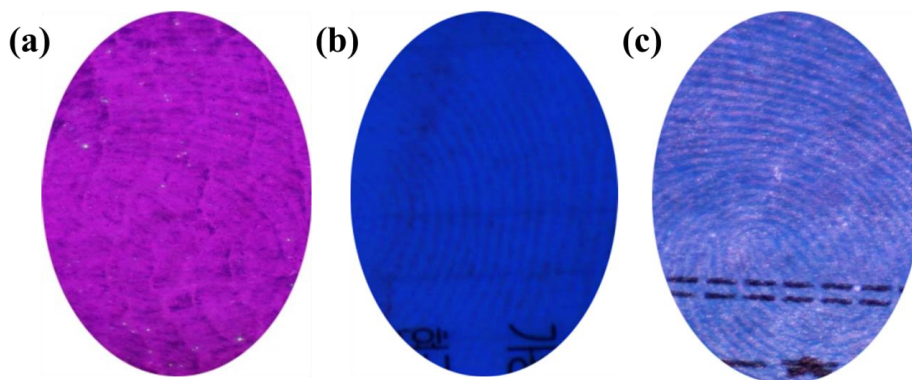


Figure 5-8. Photographs of latent fingerprints developed with $[\text{Eu}(\text{Phen})_2]^{3+}$ -hectorite-HDTMS nanocomposite on porous surfaces of (a) tape made of paper, (b) traditional credit card receipt and (c) credit card receipt made of electronic paper under UV illumination at 312 nm.

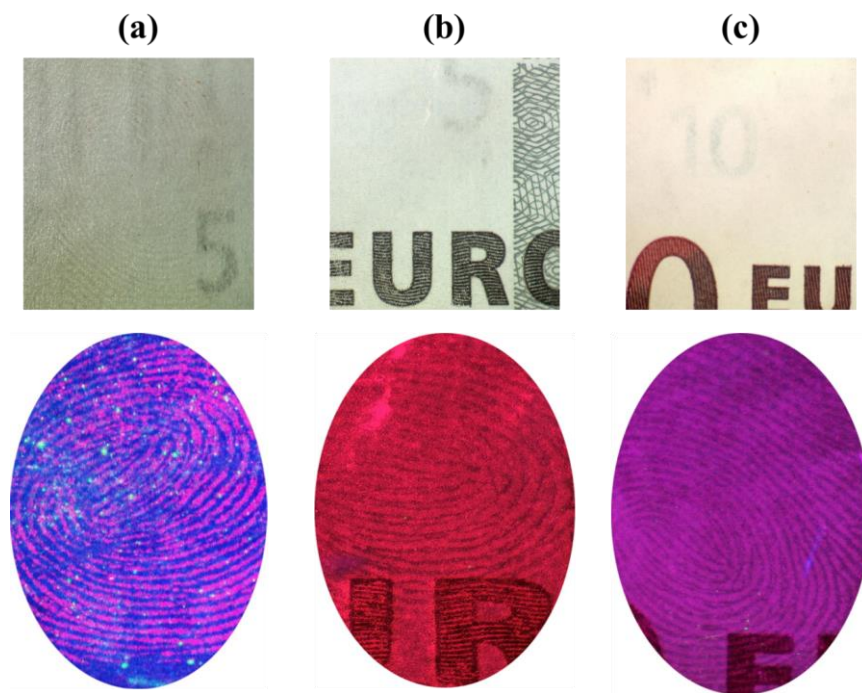


Figure 5-9. Comparison of the latent fingerprints developed using different nanocomposites on paper money surfaces. (a) $[\text{Eu}(\text{Phen})_2]^{3+}$ -montmorillonite, (b) $[\text{Eu}(\text{Phen})_2]^{3+}$ -hectorite and (c) $[\text{Eu}(\text{Phen})_2]^{3+}$ -hectorite-HDTMS. Upper and lower column are shown under white illumination and UV illumination (312 nm), respectively.

Table 5-1. Comparison of definition for the latent fingerprint developed by nanocomposites. (* * *) represents clear fingerprint ridge, (* *) most of the fingerprint ridge and (*) faint fingerprint image, respectively.

	Surface	[Eu(Phen) ₂] ³⁺ - montmorillonite	[Eu(Phen) ₂] ³⁺ -hectorite	[Eu(Phen) ₂] ³⁺ -hectorite- HDTMS
Non-porous	Glass	***	***	***
	Polymer film	***	**	**
	Plastic	**	***	**
	Metal	***	***	**
	Adhesive tape	**	**	**
Porous	Tape made of paper	**	***	*
	Traditional credit card receipt	*	**	*
	Credit card receipt made of electronic paper	*	*	**
	Paper money	**	**	***

5.5. Conclusion

We successfully synthesized and modified fluorescent europium complex ion intercalated clay nanocomposites through ion exchange and silylation reactions. These nanocomposites have suitable photoluminescence properties for the detection of latent fingerprints residue. All of the nanocomposite-based latent fingerprint developers we obtained proved successful in developing latent fingerprints on nonporous substrates of glass, polymer film, plastic, metal, and adhesive tape. In the case of porous substrates of adhesive tape made of paper, credit card receipts, and paper money, the $[\text{Eu}(\text{Phen})_2]^{3+}$ -hectorite and the $[\text{Eu}(\text{Phen})_2]^{3+}$ -hectorite-HDTMS nanocomposites showed good images for the detection of fingerprints. Finally, we conclude that in intercalation-based nanocomposite systems, the size of host clay minerals, as well as the surface properties, strongly affects latent fingerprint development.

5.6. References

1. C. Xu, R. Zhou, W. He, L. Wu, P. Wu, X. Hou, Fast imaging of eccrine latent fingerprints with nontoxic Mn-doped ZnS QDs, *Anal. Chem.* 86 (2014) 3279-3283.
2. K. Cai, R. Yang, Y. Wang, X. Yu, J. Liu, Super fast detection of latent fingerprints with water soluble CdTe quantum dots, *Forensic Sci. Int.* 226 (2013) 240-243.
3. A.M. Knowles, Aspects of physicochemical methods for the detection of latent fingerprints, *J. Phys. E* 11 (2001) 713.
4. J. Dilag, H. Kobus, A.V. Ellis, CdS/polymer nanocomposites synthesized via surface initiated RAFT polymerization for the fluorescent detection of latent fingermarks, *Forensic Sci. Int.* 228 (2013) 105-114.
5. R. Saferstein, *Criminalistics: An Introduction to Forensic Science*, Prentice-Hall of India Pvt. Ltd., New Delhi, 1978, pp. 279-299.
6. S. Oden, B. Von Hofsten, Detection of fingerprints by the ninhydrin reaction, *Nature.* 173 (1954) 449.
7. C.J. Lennard, P. Margot, M. Stoilovic, R.N. Warrenner, Synthesis of ninhydrin analogues and their application to fingerprint development: preliminary results, *J. Forensic Sci. Soc.* 26 (1986) 323.
8. R.S. Croxton, M.G. Baron, D. Butler, T. Kent, V.G. Sears, Variation in amino acid and lipid composition of latent fingerprints, *Forensic Sci. Int.* 199 (2010) 93-102.
9. L. Schwarz, An amino acid model for latent fingerprints on porous surfaces, *J. Forensic Sci.* 54 (2009) 1323-1326.
10. J. Salama, S.A. Donovan, C. Lennard, C. Roux, Evaluation of the fingermark reagent oil red O as a possible replacement for physical developer, *J. Forensic Ident.* 58 (2008) 203-207.

11. M. Tahtouh, P. Despland, R. Shimmon, The application of infrared chemical imaging to the detection and enhancement of latent fingerprints: method optimization and further findings, *J. Forensic Sci.* 52 (2007) 1089–1096.
12. L. Liu, S.K. Gill, Y. Gao, L.J. Hope-Weeks, K.H. Cheng, Exploration of the use of novel SiO₂ nanocomposites doped with fluorescent Eu³⁺/sensitizer complex for latent fingerprint detection, *Forensic Sci. Int.* 176 (2008) 163-172.
13. M.J. Choi, A.M. McDonagh, P. Maynard, C. Roux, Metal-containing nanoparticles and nano-structured particles in fingermark detection, *Forensic Sci. Int.* 179 (2008) 87-97.
14. O.S. Wolfbeis, Nanoparticle-Enhanced Fluorescence Imaging of Latent Fingerprints Reveals Drug Abuse, *Angew. Chem. Int. Ed.* 48 (2009) 2268-2269.
15. K. Li, W. Qin, F. Li, X. Zhao, B. Jiang, K. Wang, S. Deng, C. Fan, D. Li, Nanoplasmonic Imaging of Latent Fingerprints and Identification of Cocaine, *Angew. Chem. Int. Ed.* 52 (2013) 11542-11545.
16. W. Song, Z. Mao, X. Liu, Y. Lu, Z. Li, B. Zhao, L. Lu, Detection of protein deposition within latent fingerprints by surface-enhanced Raman spectroscopy imaging, *Nanoscale.* 4 (2012) 2333.
17. M. Sametband, I. Shweky, U. Banin, D. Mandler, J. Almog, Application of nanoparticles for the enhancement of latent fingerprints, *Chem. Commun.* (2007) 1142-1144
18. Y.F. Wang, R.Q. Yang, Y.J. Wang, Z.X. Shi, J.J. Liu, Application of CdSe nanoparticle suspension for developing latent fingermarks on the sticky side of adhesives, *Forensic Sci. Int.* 185 (2009) 96-99.
19. H. Jung, H.M. Kim, Y.B. Choy, S.J. Hwang, J.H. Choy, Itraconazole–laponite: kinetics and mechanism of drug release, *Appl. Clay Sci.* 40 (2008) 99–107.

20. Q. Chen, W.T. Kerk, A.M. Soutar, X.T. Zeng, Application of dye intercalated bentonite for developing latent fingerprints, *Appl. Clay Sci.* 44 (2009) 156–160.
21. S.-J. Ryu, A. Kim, M.D. Kim, S.W. Hong, S.S. Min, J.-H. Lee, J.-K. Lee, H. Jung, Photoluminescent europium(III) complex intercalated in natural and synthetic clay minerals for enhanced latent fingerprint detection, *Appl. Clay Sci.* 101 (2014) 52-59.
22. S.R. Wasserman, L. Soderholm, Effect of surface modification on the interlayer chemistry of iron in a smectite clay, *Chem. Mater.* 10 (1998) 559-566.

Chapter 6

Latent Fingerprint Detection using Semiconductor Quantum Dots as a Fluorescent Inorganic Nanomaterial for Forensic Application

6.1. Abstract

We synthesized QD@SiO₂ by a modified Stober method to enhance the visualization of latent fingerprints on diverse surfaces with maintaining PL efficiency. In order to synthesize green-emitting QD (GQD) gradient alloy QDs ($\lambda_{em} = 530$ nm) emitting green light, CdO and Zn(OAc)₂ were put into a 100-mL two-neck-RBF, and a condenser and a thermocouple were connected to the RBF. Then OA and ODE were put into the RBF, which was heated at 180 °C until the color of the solution went transparent. Amphiphilic polymers such as polyvinylpyrrolidone (PVP) were directly adsorbed onto the surface of semiconductor QDs. Also, silica shells were introduced to the QDs to synthesize QD@SiO₂ which maintains PL efficiency. QD@SiO₂ synthesized by a modified Stober method was appropriate for the detection and visualization of latent fingerprint as it maintained very strong emission efficiency as well as biocompatibility due to the silica shells on the surface. The strong fluorescence of QD could effectively visualize latent fingerprint deposited on various substrates found at the crime scenes such as aluminum foil, paper money, transparent polymer film and glass using Olympus camera. Most of the obtained fluorescent GQD@SiO₂ nano-powders based latent fingerprint developers proved successful in developing latent fingerprints on porous and nonporous substrates. Moreover, Photographs of latent fingerprints developed with GQD@SiO₂ nano-powders on porous surfaces of paper money and on non-porous surfaces of plastic materials using Video spectral comparator 6000. The results show superior fingerprint ridge images with photoluminescent property for the latent fingerprint detection in forensic application.

6.2. Introduction

Many studies on detection of latent fingerprint have been reported that introduced various materials and methods to visualize microscopic traces.^{1,2,3} Though there have been many suggestions for new materials and methods, it could not be employed for practical applications because either the materials were not mass-producible or their applicability in the crime scene was limited.

Hence, the detection ability on latent fingerprint is expected to be improved if the material is made from nano materials that exhibit good emission and have functionality that can interact with fingerprint residues, which will lead to better sensitivity and selectivity on latent fingerprint detection.^{4,5}

The limitations on the detection of latent fingerprint found in the crime scenes can be overcome by the excellent emission of the nano-particles. Moreover, its sensitivity can be improved by introducing new materials to the nano-materials that can interact with the surface of fingerprint residues.

Semiconductor quantum dots (QDs) show strong fluorescence as they have 100 to 1000 times absorption coefficients, compared with typical dyes, along with high quantum efficiency.^{6,7} They also can be adjusted to emit fluorescence in the visible region as the wavelength depends on the size of the particles.^{8,9,10} The photoluminescence (PL) spectra can be controlled due to its narrow PL spectra and one excitation wavelength, and various studies have been done to apply this to energy conversion, optical device, and especially to biological imaging. Generally QDs are synthesized in non-polar organic solvents of high boiling points to acquire single crystals of high quantum efficiency and narrow size distribution, which has been widely used as it can achieve high quantum efficiency that minimizes surface bonding compared with other methods can. However, the QDs produced by the method have many hydrophobic ligands on their surface and are only dispersed with

organic solvents, and it requires the surface treated with appropriate materials to make them dispersed with solvents like water or alcohols to improve their applicability as optical materials for biological imaging. Hence, it is important to modify the surface while maintaining the fluorescence characteristics as the QDs are prone to surface damages which reduces the efficiency significantly.

It has been attracted interests of many researchers to use QDs as fluorescence labeling marks for latent fingerprint visualization.¹¹ Menzel et al. reported an example that used QDs for latent fingerprint visualization for the first time.¹² Afterwards, most of the researches have focused on the applications of synthesized QDs, in the form of semiconductor powder or that dispersed in water, and II-VI semiconductor QDs, such as CdS, CdSe and CdTe, for fluorescence labeling marks for latent fingerprint visualization.¹³ Various studies have been reported that modified the surface of QDs to adapt to diverse applications, among which ligand exchange methods and QDs coated with amphiphilic polymer were the most representative ones.^{14, 15} As a method to make the surface of QDs hydrophilic, an introduction of silica shells to the QD surface has been studied by many researchers as well. Silica shells can be formed easily through a hydrolysis-condensation reaction of tetraethyl orthosilicate (TEOS) as a precursor with either acid or basic catalysts. Furthermore, the surface of silica shells can be treated by various organosilicon compounds, and it is easy to make the surface treated with ligands that can interact with latent fingerprint residues. It also has biocompatibility without toxicity, and hence is one of the most widely used materials for nano-material formations.¹⁶

A typical method to form QD@SiO₂ nano-particles is a reverse micelle method of water-in-oil, which easily controls the aggregation of QDs in the core. However, it requires multiple steps such as a ligand exchange reaction, and cannot avoid probable surface damages nor make it scalable as it is

inevitable to use a specific process that makes the hydrolysis and condensation of TEOS on the surface of QDs.^{17, 18, 19}

In this study, amphiphilic polymers such as polyvinylpyrrolidone (PVP) were directly adsorbed onto the surface of semiconductor QDs to overcome the limitations described above. Also, silica shells were introduced to the QDs to synthesize QD@SiO₂ which maintains PL efficiency. QD@SiO₂ synthesized by a modified Stober method²⁰ was appropriate for the detection and visualization of latent fingerprint as it maintained very strong emission efficiency as well as biocompatibility due to the silica shells on the surface.

6.3. Experimental Section

6.3.1 Materials.

Zn(OAc)₂·2H₂O, 1-octadecene (ODE), oleic acid (OA), sulfur shot, oleylamine (OLAm) and polyvinylpyrrolidone (PVP) were purchased from Aldrich. Tri-n-octylphosphine (TOP; 85%) and tetraethyl orthosilicate (TEOS) were purchased from TCI. CdO was purchased from Alfa Aesar. Selenium shot was purchased from Acros. Ethanol (EtOH) was purchased from J. T. Baker. Chloroform was purchased from Samchun Chemical Co. All other reagents were of analytical grade.

6.3.2 Synthesis of chalcogenide solutions.

In order to synthesize gradient QDs emitting green light, selenium shot (315.8 mg, 0.4 mmol) and sulfur shot (128.2 mg, 4.0 mmol) were put into a vial in the glove box, to which 3 mL of tri-n-octylphosphine (2.49 g, 6.72 mmol) was added. The solution was stirred until the solids disappeared so that its color went transparent.

6.3.3 Synthesis of green-emitting QD (GQD).

In order to synthesize gradient alloy QDs ($\lambda_{em} = 530$ nm) emitting green light, CdO (0.05136 g, 0.4 mmol) and Zn(OAc)₂ (1.0975 g, 5 mmol) were put into a 100-mL two-neck-RBF, and a condenser and a thermocouple were connected to the RBF. Then OA (6.86 mL, 4eq) and ODE (10 mL) were put into the RBF, which was heated at 180 °C until the color of the solution went transparent. To remove water, it was degassed at 150 °C in vacuum for 20 minutes. The mixture was heated at 300 °C, in which 3 mL of TOP that dissolved Se (0.03158 g, 0.4 mmol) and S (0.1282 g, 4.0 mmol) were added quickly. At the growth stage the temperature was set to 280 °C to make it to react for 10 minutes. A small amount of oleylamine and excessive EtOH were

added after the reaction, from which QDs were refined by centrifugation at 4000 rpm for 10 minutes.

6.3.4 Synthesis of QDs@PVP and QD@SiO₂

In the chloroform solution in which QDs were dispersed (10 mg QDs/ 1 mL chloroform), 100 mg of Polyvinylpyrrolidone (PVP) were added. In 5 mL of EtOH, 0.1 mL of the QD@PVP solution was added. In the solution, 0.1 mL of TEOS, base and H₂O were added in turn and stirred overnight. After the reaction, QD@SiO₂ nanoparticles were precipitated by centrifugation at 200 rpm for 20 minutes. The precipitate was added in EtOH, which was sonicated to make the QD@SiO₂ nanoparticles dispersed and centrifuged like before. This step was repeated for two more times, and it was dispersed in EtOH in the end.

6.3.5 Fingerprint development with QD@SiO₂ nano-powders.

GQD@SiO₂ was used for the fingerprint development test, and five types of substrates, slide glass, paper of yellow color, transparent polymer film, paper money and aluminum foil, were prepared. Fingerprints were from a 20-year-old male and deposited on the five substrates. GQD@SiO₂ nanoparticle powder was applied on the location the fingerprint was deposited. Excessive amounts were removed, which was followed by an air blow to remove further. After that, the specimen was excited with a 365-nm light source and the pictures were taken with an Olympus camera (C-4040Z). Furthermore, the fingers were cleaned with soap and water, and then latent fingerprints were deposited for 1 or 3 seconds on paper money and plastic surfaces. QD@SiO₂ powders brushed on the latent fingerprints using a commercial make-up brush. The latent fingerprints were observed by monitoring at 365-nm, using Video spectral comparator 6000 (Foster + Freeman Ltd., UK).

6.4. Results and Discussion

The overall process of QD@SiO₂ synthesis is described in Fig. 6-1. QDs were synthesized at first, which was then dispersed in chloroform. PVP were added into the QDs dispersed in chloroform with a weight ratio of 1:10. Some of QD@PVP in chloroform was dispersed in EtOH, in which precursors of TEOS, base and water, for silica shell synthesis were added to form QD@SiO₂ after the reaction.

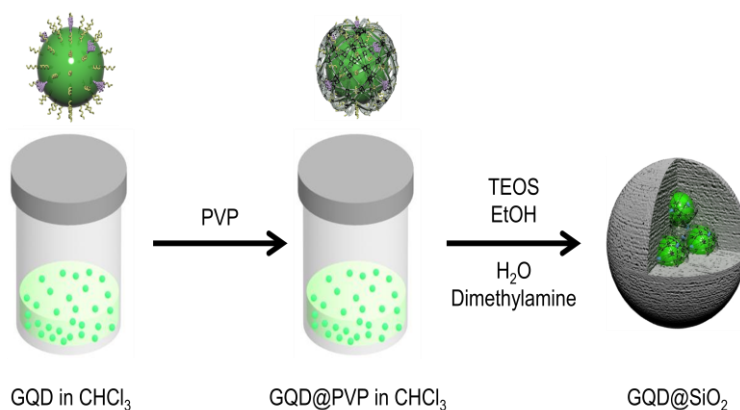


Figure 6-1. Schematic representation of synthesized GQD@SiO₂ nanoparticles.

This study introduced silica shells on the QD surface by the adsorption of PVP instead of the reverse micelle method that most researchers have used. Fig. 6-2 shows the TEM images of GQD, whose sizes were less than 10 nm. GQD exhibited an excitation peak at 530 nm for absorption and PL emission at 550 nm (Fig. 6-3.). The synthesized QDs as described above were dispersed in chloroform. The mixture of 0.1 mL was then mixed with 5 mL of EtOH, which was followed by the addition of TEOS, base and water to form QD@SiO₂ nanoparticles. Since the process could influence the stability of the

QDs such as quantum efficiency, the emission characteristics of QDs during the process were examined.

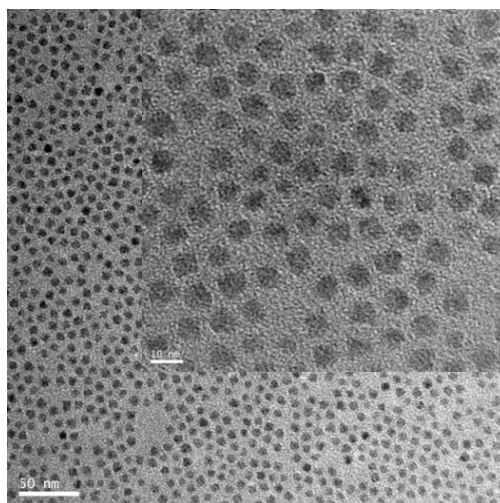


Figure 6-2. TEM images of GQDs.

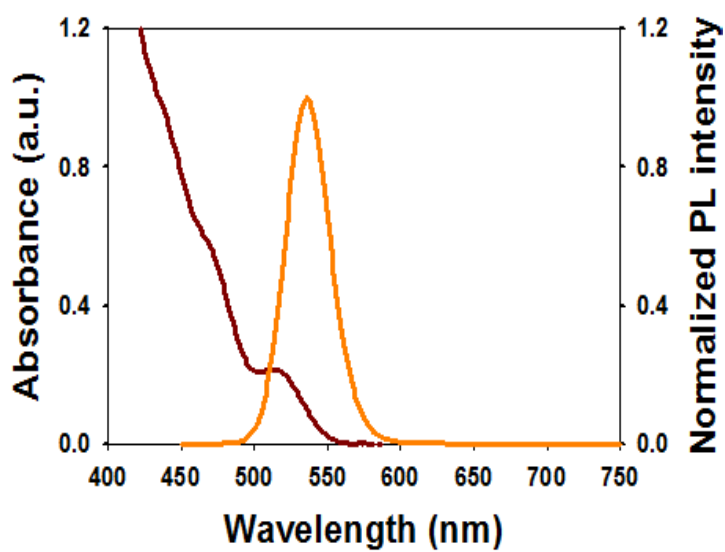


Figure 6-3. UV-visible absorbance and PL spectra.

Fig. 6-4 shows the PL from the samples taken at each stage of the process, which confirmed the emission characteristics of GQD had not been changed during the process. From the TEM images, the progress of the shell formation were confirmed during the QD@SiO₂ nanoparticles were produced.

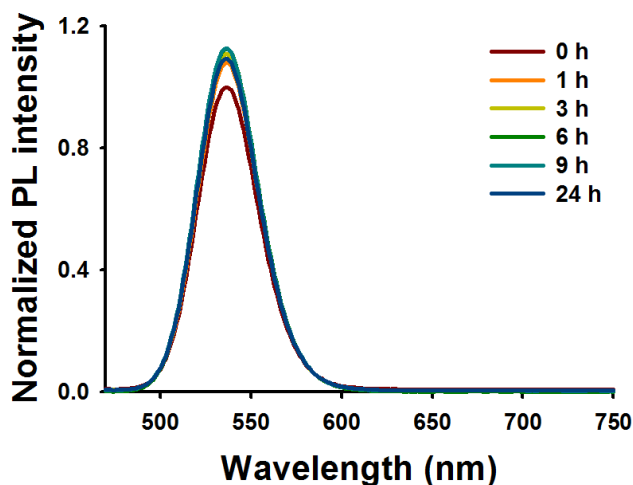


Figure 6-4. PL spectra of GQD@SiO₂ depending on reaction time.

From the Fig. 6-5 condensed TEOS was found near the quantum dots after the reaction. The shells got thicker along with the progress of the reaction, and its formation was almost finished in between 6 to 9 hours. Each silica shell contained 1~3 QDs. QD@SiO₂ of a 100-time bigger scale was synthesized based on the conditions of the previous result of QD@SiO₂ nanoparticle synthesis, as the method was scalable unlike the reverse microemulsion method. The previous result used 1 mg of QD@PVP, and this experiment used 100 mg of QD@PVP as the scale was 100 times larger.

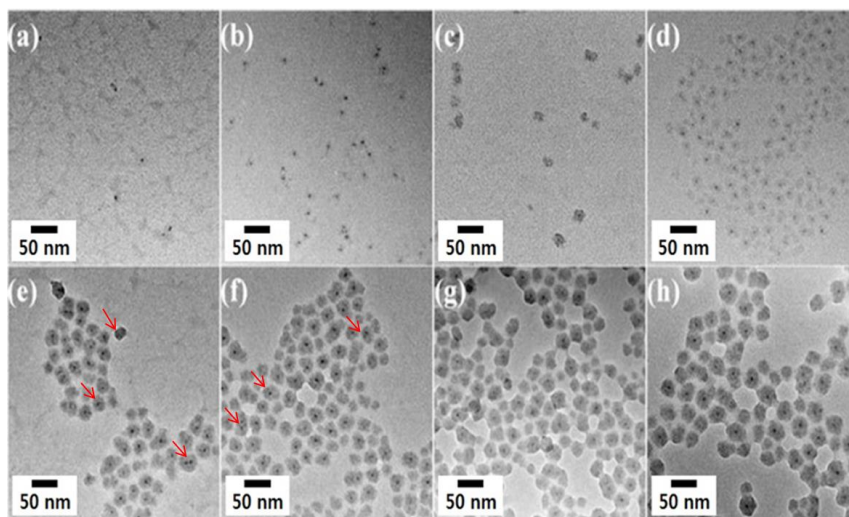


Figure 6-5. TEM images of GQD depending on reaction time; initial time (a), after 1 hour (b), 2 hours (c), 3 hours (d), 6 hours (e), 9 hours (f) 12 hours (g) and 24 hours (h). From the reaction, QD@SiO₂ of about 2.5 g could be acquired.

Various substrates can be found at the crime scenes, and four representative substrates (aluminum foil, paper money, polymer film and glass) were chosen to deposit fingerprints on. Excessive GQD@SiO₂ nano-powders were applied to the substrates, and those which did not interact with the fingerprints were removed. The residue of the nano-powders at the background was removed by an air blow. As the surface of GQD@SiO₂ was hydrophilic due to silica shells, it could make a strong interaction with latent fingerprints that was mostly comprised of water. The strong fluorescence of QD could effectively visualize latent fingerprint deposited on various substrates found at the crime scenes such as aluminum foil, paper money, transparent polymer film and glass using Olympus camera (Figure 6-6). Most of the obtained fluorescent GQD@SiO₂ nano-powders based latent fingerprint

developers proved successful in developing latent fingerprints on porous and nonporous substrates.

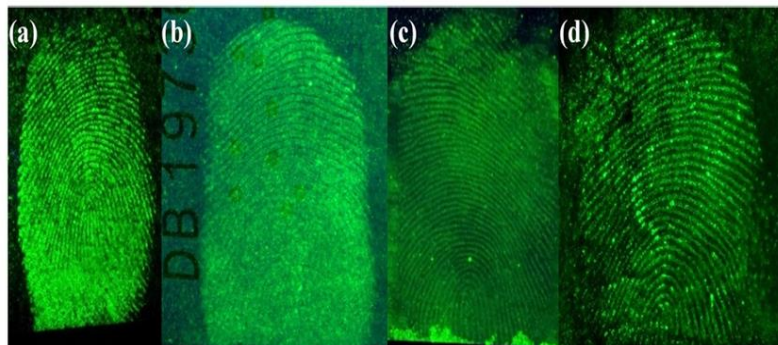


Figure 6-6. Detection of latent fingerprint using GQD@SiO₂ on aluminum foil (a), paper money (b), transparent polymer film (c) and glass (d).

Moreover, Photographs of latent fingerprints developed with GQD@SiO₂ nano-powders on porous surfaces of paper money (Figure 6-7.) and on non-porous surfaces of plastic materials (Figure 6-8.) using Video spectral comparator 6000. Fig. 6-7(b, d) and Fig. 6-8(b) show superior fingerprint ridge images with photoluminescent property for the latent fingerprint detection in forensic application compare to Fig. 6-7(a, c) and Fig. 6-8(a).

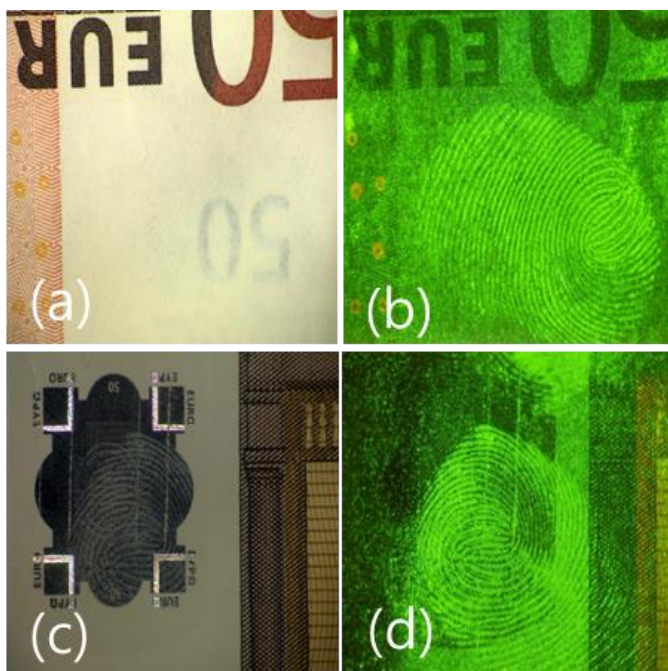


Figure 6-7. Detection of latent fingerprint on paper money as a porous surface using GQD@SiO₂ monitoring visible region (a, c) and 354-nm (b, d).

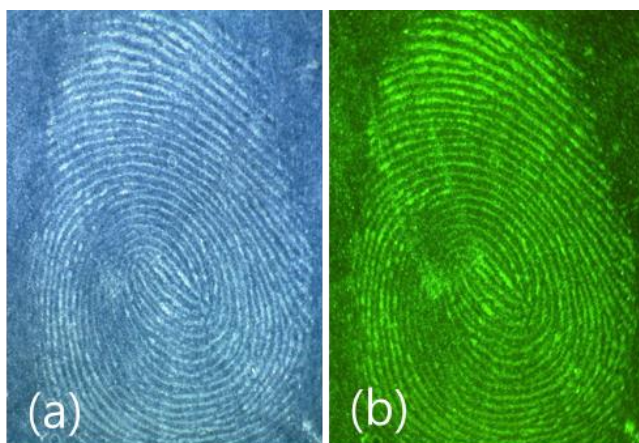


Figure 6-8. Detection of latent fingerprint on plastic surface as a non-porous surface using GQD@SiO₂ monitoring visible region (a) and 354-nm (b).

6.5. Conclusion

In this study, amphiphilic polymers such as polyvinylpyrrolidone (PVP) were directly adsorbed onto the surface of semiconductor QDs to overcome the limitations of typical method to form QDs in the core. Also, silica shells were introduced to the QDs to synthesize QD@SiO₂ which maintains PL efficiency. The QD@SiO₂ synthesized by a modified Stober method was appropriate for the detection and visualization of latent fingerprint as it maintained very strong emission efficiency as well as biocompatibility due to the silica shells on the surface.

6.6. References

1. N. Jaber, A. Lesniewski, H. Gabizon, S. Shenawi, D. Mandler, J. Almog, *Angew. Chem. Int. Ed.* **2012**, *51*, 12224.
2. M. Wood, P. Maynard, X. Spindler, C. Lennard, C. Roux, *Angew. Chem. Int. Ed.* **2012**, *51*, 12272.
3. J. Yu-Juan, L. Yun-Jun, L. Guo-Ping, L. Jie, W. Yuan-Feng, Y. Rui-Qin, L. Wen-Ting, *Forensic Sci. Int.* **2008**, *179*, 34.
4. Y. F. Wang, R. Q. Yang, Y. J. Wang, Z. X. Shi, J. J. Liu, *Forensic Sci. Int.* **2009**, *185*, 96.
5. J. Dilag, H. Kobus, A. V. Ellis, *Forensic Sci. Int.* **2008**, *187*, 97.
6. A. Becue, S. Moret, C. Champod, P. Margot, *Forensic Sci. Int.* **2009**, *191*, 36.
7. J. Liu, Z. Shi, Y. Yu, R. Yang, S. Zuo, *J. Colloid Interf. Sci.* **2010**, *342*, 278.
8. E. R. Menzel, S. M. Savoy, S. J. Ulvick, K. H. Cheng, R. H. Murdock, M. R. Sudduth, *J. Forensic Sci.* **2000**, *45*, 545.
9. E. R. Menzel, M. Takatsu, R. H. Murdock, K. Bouldin, K. H. Cheng, *J. Forensic Sci.* **2000**, *45*, 770.
10. K. K. Bouldin, E. R. Menzel, M. Takatsu, R. H. Murdock, *J. Forensic Sci.* **2000**, *45*, 1239.
11. F. Gao, J. Han, C. Lv, Q. Wang, J. Zhang, Q. Li, L. Bao, X. Li, *J. Nanopart. Res.* **2012**, *14*, 1191.
12. B. E. Dalrymple, J. M. Duff, E. R. Menzel, *J. Forensic Sci.* **1977**, *22*, 106.
13. F. Gao, C. Lv, J. Han, X. Li, Q. Wang, J. Zhang, C. Chen, Q. Li, X. Sun, J. Zheng, L. Bao, X. Li, *J. Phys. Chem. C* **2011**, *115*, 21574.
14. F. Gao, J. Han, J. Zhang, Q. Li, X. Sun, J. Zheng, L. Bao, X. Li, Z. Liu, *Nanotechnology* **2011**, *22*, 075705.
15. M. Algarra, J. Jimenez-Jimenez, R. Moreno-Tost, B. B. Campos, J. C. G. Esteves da Silva, *Opt. Mater.* **2011**, *33*, 893.

16. H. S. Jung, Y. J. Kim, S. W. Ha, J. K. Lee, *J. Mater. Chem C.* **2013**, 1, 5879.
17. R. Xie, U. Kolb, J. Li, T. Basché and A. Mews, *J. Am. Chem. Soc.* **2005**, 127, 7480.
18. E. Jang, S. Jun and L. Pu, *Chem. Commun.* **2003**, 2964.
19. D. D. Sarma, A. Nag, P. K. Santra, A. Kumar, S. Sapra and P. Mahadevan, *J. Phys. Chem. Lett.* **2010**, 1, 2149.
20. H. S. Jung, Y. J. Kim, J.S. Cho, T. J. Yoon, J. K. Lee, *Nanoscale.* **2015**, Submitted.

APPENDIX/Chapter 1

Layered double hydroxide as novel antibacterial drug delivery system

1.1. Abstract

The cephalosporin class antibacterial agent, cefazolin, was intercalated into layered double hydroxides (LDHs) in order to improve the drug efficiency as well as to achieve the controlled release property. Cefazolin molecules were incorporated into LDH through conventional ion exchange reaction. X-ray diffraction pattern analyses confirmed that cefazolin molecules were intercalated between the interlayer spaces of LDH. Fourier-transform infrared spectra and high performance liquid chromatographs clearly showed that the drug molecules were stabilized in LDH lattice through electrostatic interaction and released without any changes in their chemical integrity. Antibacterial activity of the Cefazolin-LDH nanohybrid was also examined by *in vitro* test, such as the minimal inhibitory concentration (MIC) by dilution method. Consequently, the cefazolin-LDH nanohybrid reveals an enhanced antibacterial activity compared to the cefazolin itself not only due to an improvement of chemical stability of cefazolin molecules but also due to a controlled release property.

1.2. Introduction

Considerable research efforts have been focused on inorganic/inorganic, organic/inorganic, and bio/inorganic nanohybrids because of their diverse technical applications and various advantages incorporated with desired functionality¹⁻³. Particularly, novel bio/inorganic nanohybrids have been of great interest due to their roles as both reservoirs and delivery carriers of functional biomolecules^{4,5}. Therefore, intercalation of biomolecules, such as DNA, ATP, nucleosides, and other potential drugs into LDH has been extensively studied recently^{3,6}. Bio/inorganic nanohybrid can protect the biomolecules from decomposition or denaturization, which made it applicable to safe, targeted, and controlled drug delivery⁷.

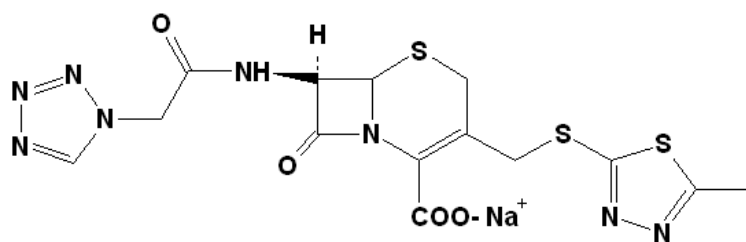
Layered double hydroxide (LDH), so-called anionic clay, has attracted considerable attentions due to its technological importance in catalysis, separation technology, optics, nanocomposite materials engineering and medical science⁸. LDH consists of cationic brucite-like layers and exchangeable interlayer anions, represented by the general formula, $[M^{II}_1 \cdot_x M^{III}_x(OH)_2]^{x+} (A^{n-})_{x/n} \cdot yH_2O$, where M^{II} , M^{III} , and A^{n-} are di-, tri-valent metal cations, and interlayer anions, respectively. Due to the anion-exchangeable properties, LDHs can form a bio/inorganic hybrid with many different anionic drugs.

Cefazolin, one of cephalosporin β -lactam antibiotics, has a potent activity against a large number of gram-positive and gram-negative organisms⁹. Especially, cefazolin is bactericidal in action with a broad antibacterial spectrum as are the other cephalosporin antibiotics. The chemical formula of cefazolin is $C_{14}H_{14}N_8O_4S_3$ and its molecular weight is 454.51g/mol [Fig. 1]. Although cefazolin has many advantages compared to other cephalosporin antibiotics and penicillin, there still posed several problems

with chemical stability and clinical use¹⁰. Cefazolin can be easily denatured by hydrolysis and decomposed above at 65 °C¹¹. Furthermore, in clinical use, frequent administration has been required to maintain therapeutical drug concentration.

Such antibiotics, either systemic or local, were often used for chronic infection. In combination with surgery, effective delivery of antimicrobial would be critical to prevent bone infection¹². Polymethylmethacrylate (PMMA) bone cement beads were often employed for delivery of local antibiotics for the treatment of bone infection.¹³ However, due to its poor mechanical property, thermal and chemical necrosis of bones were often reported, resulted from unreacted monomer release, shrinkage during polymerization, poor distribution around the implant, and weak attachment at the interface¹⁴. Thus, more efficient delivery system for local antibiotics is needed.

In this study, we designed the cefazolin-LDH nanohybrid as a controlled drug delivery system. Cefazolin was intercalated into $Zn_2Al(OH)_6-NO_3$ by ion-exchange reaction. The structure of cefazolin-LDH nanohybrids was characterized with X-ray diffraction patterns and the chemical composition was determined with elemental analysis and thermogravimetry. The enhanced antibacterial activity of the cefazolin-LDH nanohybrid compared to cefazolin itself was investigated by carrying out the modified disc diffusion method to observe the zones of bacterial inhibition versus time.



APPENDIX/Figure 1-1. Molecular structure of the cefazolin sodium salt.

1.3. Experimental Section

1.3.1 Preparation of pristine $\text{Zn}_{0.65}\text{Al}_{0.35}(\text{OH})_2(\text{NO}_3)_{0.35} \cdot 6 \text{H}_2\text{O}$ and cefazolin-LDH nanohybrid.

Pristine $\text{Zn}_{0.65}\text{Al}_{0.35}(\text{OH})_2(\text{NO}_3)_{0.35} \cdot 6\text{H}_2\text{O}$ was prepared by conventional coprecipitation method under N_2 atmosphere. A mixed solution of $\text{Zn}(\text{NO}_3)_2 \cdot 6\text{H}_2\text{O}$ (0.024M) and $\text{Al}(\text{NO}_3)_3 \cdot 9\text{H}_2\text{O}$ (0.012M) was titrated with NaOH (0.5M) solution at room temperature. During titration, the solution pH was adjusted to 7.0 ± 0.2 . The resulting white precipitation was collected by centrifugation and washed with decarbonated water thoroughly.

Cefazolin-LDH nanohybrid was prepared by ion exchange method. Cefazolin sodium salt was first resolved in a mixed solvent. In order to prevent cefazolin from hydrolysis, mixed solvent consisted of EtOH (70%) and deionized water (30%) was utilized. The pristine LDH was then mixed with cefazolin solution to produce colloidal suspension. Molar ratio of sodium cefazolin and the pristine LDH ($\text{Zn}_{0.65}\text{Al}_{0.35}(\text{OH})_2(\text{NO}_3)_{0.35} \cdot 6\text{H}_2\text{O}$) was 2:1 in order to facilitate concentration gradient mediated ion exchange. The suspension was stirred vigorously and aged at room temperature for 1 day under N_2 atmosphere. The resulting solid was washed with EtOH at least three times, centrifuged at 3400 rpm and vacuum-dried for 1day. Cefazolin was purchased from Daewoong chemical company (Kyunggi-do, Korea). All other reagents were of analytical grade.

1.3.2 Characterization of the cefazolin-LDH.

The structural properties were confirmed by both powder X-ray diffraction (XRD) and Fourier-transform infrared spectroscopic analyses. Powder X-ray diffraction patterns were measured by a Philips PW 3710 powder diffractometer equipped with Ni-filtered Cu K_α radiation

($\lambda=1.5405\text{\AA}$) at 20mA and 40kV. The hybrid compositions were determined by elemental analysis (CHNS), thermal analysis (TG-DTA) and inductively coupled plasma spectrometry (ICP). The elemental analysis was conducted with an EA1110 (CE instrument, Italy). TG-DTA curves were recorded in a nitrogen atmosphere at a heating rate of 5°C/min. Inductively coupled plasma spectrometric analysis was carried out with a Shimadzu ICPS-1000IV. According to these data we could determine the chemical composition of pristine LDH and cefazolin-LDH hybrid in table. 1.

1.3.3 In vitro test.

3.8 g of Muller Hinton II-agar (BD, Cat. No. 211438, 38 g/L) were added to 500 ml flask with 100 ml of distilled water and 0.8 % NaCl solution respectively. Liquid medium was boiled for 1 minute using a microwave and sterilized at 121 °C in autoclave (hanshin medical CO. LTD., model: AT-650) for 15 minutes. Autoclaved agar was poured to 90 mm of petri dish until 4-6 mm of depth. When agar get stiff, put the lid on and store at 4 °C.

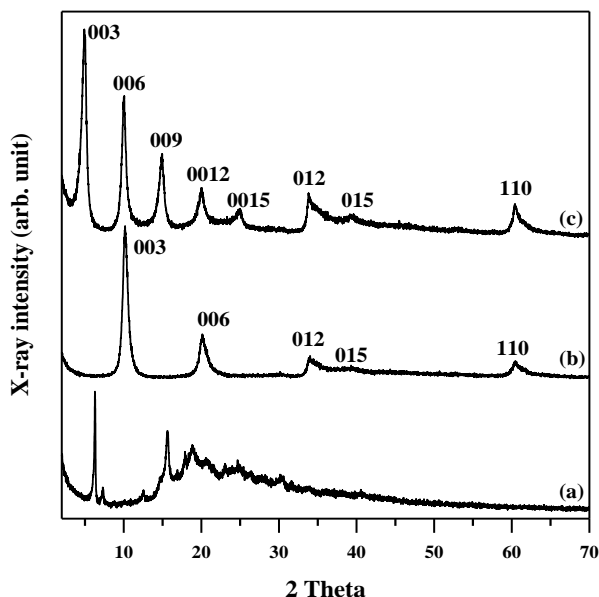
For mother solution of cefazolin and cefazolin-LDH nanohybrid, 0.0015 g of cefazolin and 0.006 g of cefazolin-LDH nanohybrid were prepared into 1 ml of distilled water and 0.8 % NaCl solution with 1.5 ml tube. The cefazolin-LDH nanohybrid was dispersed by ultrasonication to produce homogeneously dispersed suspension. 5 µl of cefazolin and cefazolin-LDH nanohybrid was dropped into 6 mm of blank disk (Becton, Dickinson and Company) respectively. The dropped disk was dried at 55 °C for 15-30 minute.

10⁸/ml CFU of *S. aureus* ATCC 25923 (supplied with The Korean Association of Quality Assurance for Clinical Laboratory) was inoculated into 3 ml of inoculum's water bottles that based on distilled water and 0.8 % NaCl solution. The agar plate was applied the *S. aureus* 25923 and streaking for 3

minute. The prepared cefazolin and cefazolin-LDH disc was attached to the agar plate. The cefazolin and cefazolin-LDH in petri dish was incubated at 37 °C and 95 % of humidity. The zones of bacterial inhibition were investigated for 1, 3, 5 days respectively.

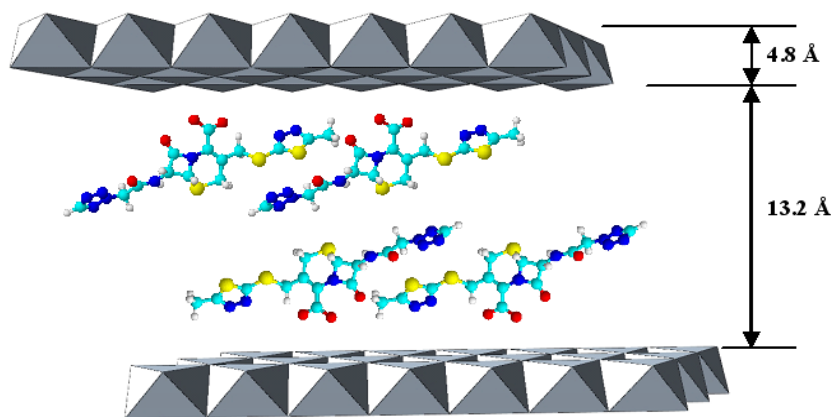
1.4. Results and Discussion

The powder XRD patterns of the pristine ZnAl-LDH, cefazolin-LDH nanohybrid, and cefazolin sodium are shown in Fig.2. Pristine LDH exhibited well-developed (00 l) reflections, such as (003) and (006) with the basal spacing of 8.9 Å. The increase in basal spacing from 8.9 to 18 Å indicated that cefazolin molecules were intercalated in LDH by replacing NO₃⁻ ions. The (00 l) reflections of the pristine LDH shifted to lower angle without any changes of the lattice peaks, such as (012), (015) and (110) after intercalation. The cefazolin sodium showed a well developed characteristic crystalline pattern as previously reported¹⁵. However, the XRD pattern of the nanohybrid did not show any of the distinctive cefazolin crystalline peaks, which also proved that cefazolin anion was successfully intercalated into the nanosize domain of the LDH interlayers.



APPENDIX/Figure 1-2. Powder X-ray diffraction patterns of cefazolin-LDH (a), ZnAl-LDH (b) and cefazolin sodium (c)

Because the sheet thickness of brucite-like LDH was 4.8 Å, the gallery height of nanohybrid was estimated to be 13.2 Å¹⁰, which was larger than the perpendicular length (5.6 Å) and smaller than the horizontal length of cefazolin (20.2 Å). The result from the gallery heights suggested that the cefazolin molecules were intercalated in bilayered arrangement with a tilting angle of 118°, as illustrated in Fig. 3. Thus, after intercalation, the lattice structure of LDH extended only to the *c*-axis direction with the increase in basal spacing. The bilayer arrangement could also be explained by two different anion areas of cefazolin and LDH. According to the horizontal length of cefazolin (20.2 Å), the area of two anions (62.6 Å²) is larger than the equivalent area of LDH (24.3 Å²). Therefore, cefazolin molecules are thought to occupy more than two equivalent areas of LDH to balance charge compensation with NO₃⁻ ions.



APPENDIX/Figure 1-3. Powder X-ray diffraction patterns of cefazolin-LDH (a), ZnAl-LDH (b) and cefazolin sodium (c)

APPENDIX/Table 1. Chemical compositions of the pristine LDH and cefazolin-LDH hybrid by ICP and CHNS measurements

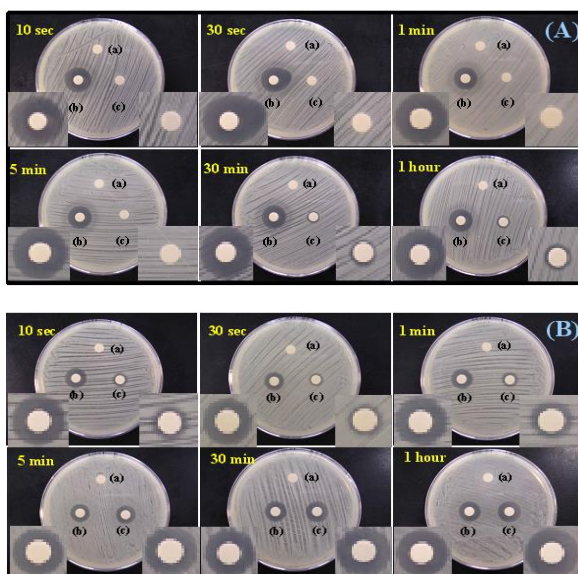
Sample	Zn/Al		CHNS (%)								Chemical composition	
	Calculated	Observed	Calculated				Observed					
			C	H	N	S	C	H	N	S		
Pristine LDH	2.00	1.86	-	-	-	-	-	-	-	-	-	$\text{Zn}_{0.65}\text{Al}_{0.35}(\text{OH})_2(\text{NO}_3)_{0.35} \cdot 6 \text{H}_2\text{O}$
Cefazolin-LDH	2.00	1.86	13.92	1.16	9.27	7.96	14.83	3.01	9.65	7.96	$\text{Zn}_{0.65}\text{Al}_{0.35}(\text{OH})_2(\text{Cefazolin})_{0.22}(\text{NO}_3)_{0.13} \cdot 6 \text{H}_2\text{O}$	

The cefazolin–LDH nanohybrid was examined to see its efficacy as drug delivery carrier. The amount of cefazolin in LDH was determined to be 37 wt % by TG data and also confirmed by CHNS (error limit $< \pm 1$ wt %). For CHNS analysis, the value from S was considered to be critical because S was attributed only to the cefazolin composition. The difference between the observed and calculated values seemed to be generated by water molecules in the interlayer of nanohybrid. The drug release from nanohybrid was measured employing high performance liquid chromatography (HPLC). The result from HPLC also proved that cefazolin in LDH retained its chemical integrity even when released by ion exchange reaction. Two distinct solutions, with and without NaCl, respectively, were employed as the release media to examine the effect of anions on drug release. In a 0.8 % NaCl solution, 66 % of cefazolin was released in 30 minutes while the nanohybrid in water showed only 25 % release in 90 minutes. This result is not surprising because the drug release from LDH-mediated nanohybrid is determined by anion exchange property. Highly concentrated chloride ions in a NaCl solution expedited ion exchange reaction, hence increased amount of drug release.

In order to observe the antibacterial activity of nanohybrid with controlled release property, time scheduled disc diffusion method was carried out both in water and a 0.8 % NaCl solution, respectively. LDH and cefazolin sodium were also employed for the control. Fig. 4 shows the change of dark grey zones of bacterial inhibition versus time with different conditions. LDH did not show any antibacterial activity while cefazolin sodium and nanohybrid exhibited the dark zones around the disc. For cefazolin sodium, the zones of bacterial inhibition expanded to 225 mm² in 10 s and did not change as the time elapsed in both solutions. The fast dissolution of cefazolin sodium seemed to cause the sudden expansion of antibacterial zones. However, for cefazolin-LDH nanohybrid, the antibacterial zones

changed in time-dependent manners. However, in water, the zone was not formed during the first 5 min, which started to be seen at 30 min (Fig. 4(A)). Moreover, the size of the antibacterial zone was very small compared with that from cefazolin sodium. Even at 1 h, the zone from nanohybrid was still 124 mm^2 .

Notably, in case of a 0.8 % NaCl solution, the antibacterial response was faster and the zones expanded more dramatically as the time elapsed. As shown in Fig. 4(B), the zones started to expand at 10 s, the area of which increased to 240 mm^2 at 1 h. Corresponded to the result from the in vitro drug release study, the antibacterial activity seemed to be enhanced by facilitated release of cefazolin with the presence of anions. It should also be noted that the antibacterial activity of cefazolin exhibited sustained release patterns unlike cefazolin sodium itself.



APPENDIX/Figure 1-4. Zones of bacterial inhibition of (a) LDH, (b) cefazolin sodium, and (c) cefazolin-LDH nanohybrid in (A) water and (B) a 0.8 % NaCl solution.

1.5. Conclusion

In summary, cefazolin-LDH nanohybrid was prepared by intercalating cefazolin into the interlayer space of ZnAl-LDH via conventional ion exchange reaction. The nanohybrid exhibited the gallery height of 13.2 Å, which suggested that cefazolin molecules were arranged in the interlayer with double layer arrangement and a tilting angle. In addition, it was found that cefazolin was stabilized in LDH through electrostatic interaction and released without any changes in its chemical integrity. The content of cefazolin in nanohybrid was estimated to be about 37 wt % by TG and CHNS analyses. Antibacterial activity of the cefazolin-LDH nanohybrid could be confirmed by the modified diffusion disc method, which showed that cefazolin was released from nanohybrid with time dependent manners. Especially with the presence of anions, the antibacterial activity was observed to be enhanced due to expedited ion exchange. Therefore, it could be concluded that LDH is an excellent biocompatible inorganic matrix that could improve the antibacterial efficiency of cefazolin with controlled release property.

1.6. References

1. J. H. Choy, S. J. Kwon and G. S. Park, *Science* 280 (1998), 1589-1592.
2. J. H. Choy, J. B. Yoon, H. Jung, *J. Phys. Chem. B* 106 (2002), 11120-11126.
3. J. H. Choy, S. Y. Kwak, J. S. Park, Y. J. Jeong and J. Portier, *J. Am Chem. Soc.* 121(1999), 1399-1400.
4. J. H. Choy, S. Y. Kwak, Y. J. Jeong and J. S. Park, *Angew. Chem. Int. Ed.* 39(2000), 4042-4045.
5. S. Y. Kwak, W. M. Kriven, M. A. Wallig and J. H. Choy, *Biomaterials* 25(2004), 5995-6001.
6. J. H. Choy, S. Y. Kwak, J. S. Park and Y. J. Jeong, *J. Mater. Chem.* 11(2001), 1671-1674.
7. J. H. Choy, J. S. Jung, J. M. Oh, M. Park, J. Y. Jeong, Y. K. Kang and O. J. Han, *Biomaterials* 25(2004), 3059-3064.
8. M. Ogawa and K. Kuroda, *Chem. Rev.* 95(1995), 399-438.
9. J. Kozatani, M. Okui, K. Noda, T. Ogino and H. Noguchi, *Chem. Pharm. Bull.* 20 (1972), 1105-1113.
10. J. R. Anaconda and P. Alvarez, *Trans. Met. Chem.* 27(2002), 856-860.
11. C. F. Martin, L. T. Takahashi, J. L. Worsley, C. J. Hagemeyer and L. K. Hall, *J. Chromatography* 402(1987), 376-380.
12. P. J. Benaerts, B. M. F. Ridler, P. Vercaeren, J. F. Thompson and W. B. Campbell, *Cardiovascular Surgery* 7(4)(1999), 447-450.
13. A. S. Baker and L. W. Greenham, *J. Bone Jt. Surg. Am.* 70A(1988), 1551-1557.
14. S. Torrado, P. Frutos and G. Frutos, *Int. J. Pharm.* 217(2001), 57-69.
15. G. A. Stephenson and B. A. Diserod, *Int. J. Pharm.* 198(2000), 167-177.

Korean Abstract

표면 개질된 무기물질들은 다기능성을 부여할 수 있는 장점과 다양한 분야로의 응용 가능성 때문에 중요한 연구분야로 각광받고 있다. 본 논문에서는 색상변화를 이용한 법과학적 센서를 위한 금속 양이온으로 표면 개질된 실리카 파우더, 잠재지문 (미세흔적) 현출을 위한 유로피움 착물이 삽입된 표면 개질된 나노 킴포짓 물질 개발 및 법과학적 응용을 위해 증대된 형광 무기 나노 물질로서의 반도체 양자점의 잠재지문 (미세흔적) 현출에 대한 연구를 진행하였다.

1장에서는 법과학적 증거물에 대한 설명을 기초로 금속 양이온으로 표면 개질된 실리카 파우더를 이용한 현장용 법과학적 센서, 잠재지문 (미세흔적) 현출을 위한 유로피움 착물이 삽입된 표면 개질된 나노 킴포짓 물질 개발 및 법과학적 응용을 위해 증대된 형광 무기 나노 물질로서의 반도체 양자점의 잠재지문 (미세흔적) 현출에 대한 연구배경을 소개하였다.

2장에서는 황화수소 및 암모니아 가스를 효과적으로 검출하기 위해 금속 양이온인 은 및 구리로 표면 개질된 실리카 파우더 센서를 개발하였다. 황화수소 가스 검출을 위한 센서에서는 은으로 표면 개질된 실리카 파우더가 황화수소와 결합하였을 때 검은색 또는 갈색으로 색상변화를 일으켜 치사량 이하의 농도에서 효과적으로 검출할 수 있음을 확인할 수 있었다. 또한 암모니아 가스 검출을 위한 센서에서는 구리로 표면 개질된 실리카 파우더가 암모니아와 결합하였을 때 파란색으로 색상변화를 일으켜 치사량 이하의 농도에서 효과적으로 검출할 수 있음을 확인할 수 있었다.

3장에서는 납이온으로 표면 개질된 실리카 파우더 센서를 이용하여 혈액 또는 용액의 시료에서 황화이온을 빠른 시간 안에 효과적으로 검출하고자 하였다. 황화수소 가스에 중독된 혈액의 혈장에서 황화이온을 치사량 이하 및 그 이상의 농도에서 효과적으로 검출할 수 있었다.

4장에서는 법과학적 잠재지문 및 미세흔적 현출을 위한 유로피움 착물

이 삽입된 표면 개질된 나노 컴포짓 물질을 개발하였다. 자연계에 존재하는 점토 광물 및 합성된 점토 광물에 유로피움 착물을 이온교환 반응을 통하여 표면 개질된 나노 컴포짓 물질을 효과적으로 합성할 수 있었다. 또한 감소되지 않은 본래의 형광특성과 더불어 잠재지문 및 미세흔적과 효과적으로 부착시킬 수 있는 나노 컴포짓 물질을 개발하였다. 이 물질을 활용하여 효과적으로 잠재지문을 현출할 수 있었다.

5장에서는 합성된 나노 컴포짓 물질을 활용하여 다양한 표면에서 실질적 응용을 위한 잠재지문 현출에 대한 실험을 진행하였다. 소수성으로 표면 개질된 나노 컴포짓 물질에서 다공성 표면의 잠재지문 현출에 좋은 이미지를 얻을 수 있었으며, 친수성 나노 컴포짓 물질에서 비다공성의 다양한 표면에서 효과적으로 잠재지문을 검출할 수 있었다.

6장에서는 형광성 무기 나노 물질인 반도체 양자점을 이용하여 법과학적 잠재지문 및 미세흔적 현출을 위한 잠재지문 현출에 대한 실험을 진행하였다. 양자점에 실리카 껍질을 도입하여 합성된 물질은 다공성 및 비다공성 표면에서 증대된 형광특성을 유지함과 동시에 효과적인 흡착력을 확인할 수 있었다. 특히 지폐 등의 비다공성 표면에서 가변광원을 활용하여 형광특성을 지닌 형광성 무기 나노 물질인 실리카가 도입된 반도체 양자점을 이용하여 효과적으로 잠재지문을 현출할 수 있었다.

이와 같은 연구결과 다양한 금속 양이온으로 표면 개질된 실리카 파우더, 유로피움 착물이 삽입된 표면 개질된 나노 컴포짓 물질 및 실리카 껍질이 도입된 반도체 양자점인 형광성 무기 나노 물질들을 활용하여 다양한 법과학적 응용에 대한 가능성을 확인할 수 있었다.

주요 핵심어: 법과학적 센서, 유해가스, 표면 개질된 실리카, 유로피움 착물, 삽입반응, 유-무기 하이브리드, 나노 컴포짓, 형광성 무기 나노 물질, 잠재지문 현출, 법과학적 응용

학번: 2008-30096